STUDY OF ICE CLOUD PROPERTIES FROM SYNERGETIC USE OF SATELLITE OBSERVATIONS AND MODELING CAPABILITIES

A Dissertation

by

YU XIE

Submitted to the Office of Graduate Studies of
Texas A&M University
in partial fulfillment of the requirements for the degree of

DOCTOR OF PHILOSOPHY

December 2010

Major Subject: Atmospheric Sciences

STUDY OF ICE CLOUD PROPERTIES FROM SYNERGETIC USE OF SATELLITE OBSERVATIONS AND MODELING CAPABILITIES

A Dissertation

by

YU XIE

Submitted to the Office of Graduate Studies of
Texas A&M University
in partial fulfillment of the requirements for the degree of

DOCTOR OF PHILOSOPHY

Approved by:

Chair of Committee,	Ping Yang
Committee Members,	George Kattawar
	Shaima Nasiri
	Gerald North
Head of Department,	Kenneth Bowman

December 2010

Major Subject: Atmospheric Sciences

ABSTRACT

Study of Ice Cloud Properties from Synergetic Use of Satellite Observations and Modeling Capabilities. (December 2010)

Yu Xie, B.S., Peking University;

M.S., Texas A&M University

Chair of Advisory Committee: Dr. Ping Yang

The dissertation first investigates the single-scattering properties of inhomogeneous ice crystals containing air bubbles. Specifically, a combination of the ray-tracing technique and the Monte Carlo method is used to simulate the scattering of light by randomly oriented large hexagonal ice crystals containing spherical or spheroidal air bubbles. The effect of the air bubbles within ice crystals is to smooth the phase functions, diminish the 22° and 46° halo peaks, and reduce the backscatter in comparison with the case of bubble-free ice crystals. Cloud reflectance look-up tables were generated at the wavelengths of 0.65 μm and 2.13 μm to examine the impact of accounting for air bubbles in ice crystal morphology on the retrieval of ice cloud optical thickness and effective particle size.

To investigate the effect of the representation of aggregates on electromagnetic scattering calculations, an algorithm is developed to efficiently specify the geometries of aggregates and to compute some of their geometric parameters such as the projected area. Based on *in situ* observations, aggregates are defined as clusters of hexagonal plates with a chain-like overall shape. An aggregate model is developed with 10 ensemble members, each consisting of between 4-12 hexagonal plates. The scattering properties of an

individual aggregate ice particle are computed using the discrete dipole approximation or an Improved Geometric Optics Method, depending upon the size parameter. The aggregate model provides an accurate and computationally efficient way to represent all aggregates occurring within ice clouds.

We developed an algorithm to determine an appropriate ice cloud model for application to satellite-based retrieval of ice cloud properties. Collocated Moderate Resolution Imaging Spectroradiometer and Multi-angle Imaging SpectroRadiometer (MISR) data are used to retrieve the optical thicknesses of ice clouds as a function of scattering angle in the nine MISR viewing directions. The difference between cloud optical thickness and its averaged value over the nine viewing angles can be used to validate the ice cloud models. Using the data obtained on 2 July 2009, an appropriate ice cloud model is determined. With the presence of all the uncertainties in the current operational satellite-based retrievals of ice cloud properties, this ice cloud model has excellent performance in terms of consistency in cloud property retrievals with the nine MISR viewing angles.

ACKNOWLEDGEMENTS

I would like to thank all people who have helped and inspired me during this work and the writing of this dissertation. I would like to express my deep sense of gratitude to my research advisor, Dr. Ping Yang, for providing me the opportunity to earn a degree in higher education. His enthusiasm in research has consistently motivated me toward better technical writing. I have continued to benefit from his knowledge, inspiration, patience and encouragement throughout this research. I would like to extend my gratitude to my committee members, Drs. George Kattawar, Shaima Nasiri, and Gerald North. Their detailed and constructive comments have been most helpful in shaping this dissertation.

I also wish to acknowledge Drs. Patrick Minnis and Bryan Baum who gave me important guidance throughout this work. Their valuable ideals and advice have had a remarkable influence on my entire career. I am deeply grateful to Drs. Sally McFarlane and Wenbo Sun who shared their invaluable experience and insights on the application of MISR data. I warmly thank my many colleagues in Texas A&M University. I owe my sincere gratitude to Drs. Gang Hong, Heli Wei, Yong-Keun Lee, Jianguo Niu, Hironobu Iwabuchi, and Shouguo Ding for their companionship and help in the past years. I would like to thank all the other folks in our group for inspiring me in research and life through our interactions in our offices.

I would like to thank my parents for their unconditional love and support throughout my life. Last, but not least I would like to thank my wife, Lei Hu, whose patience and devotion is incredible. Her love has always been with me. I dedicate this dissertation to her.

TABLE OF CONTENTS

CHAPTER Page

LIST OF TABLES

LIST OF FIGURES

FIGURE Page

FIGURE Page

FIGURE Page

FIGURE Page

CHAPTER I

INTRODUCTION

Field campaigns such as the First International Satellite Cloud Climatology Project (ISCCP) Regional Experiments (FIRE) [*Starr*, 1987], Tropical Rainfall Measurement Mission (TRMM) [*Silva Dias et al.*, 2002; *Yuter et al.*, 2005], and Cirrus Regional Study of Tropical Anvils and Cirrus Layers-Florida Area Cirrus Experiment (CRYSTAL-FACE) [*Jensen et al.*, 2004] have demonstrated that ice crystals within cirrus clouds are normally defective and irregular in shape [*Arnott et al.*, 1994; *Baumgardner et al.*, 2005; *Chepfer et al.*, 2005; *Heymsfield et al.*, 1990; *Heymsfield et al.*, 2002; *Heymsfield*, 2003; *Heymsfield and Miloshevich*, 2003; *Korolev et al.*, 1999; *Nasiri et al.*, 2002; *Noel et al.*, 2004]. The great natural variability of cloud ice crystal habits causes large uncertainties in the computation of the transfer of electromagnetic radiation involving cirrus clouds and has drawn a great deal of attention, as evidenced by the large volume of research devoted to the topic [*Baran et al.*, 2005; *Lawless et al.*, 2006; *Lawson et al.*, 1998; *Macke*, 1993; *Macke et al.*, 1996b; *Masuda et al.*, 2002; *McFarquhar et al.*, 2002; *Mishchenko et al.*, 1996; *Takano and Liou*, 1995; *Wendisch et al.*, 2007; *Yang and Liou*, 1998; *Yang and Fu*, 2009]. To improve the treatment of the bulk radiative properties of ice clouds in various remote sensing and climate modeling applications, the applied optics community needs to first fully understand and provide

---

This dissertation follows the style of *Journal of Geophysical Research.*

accurate scattering and absorption characteristics of a monodisperse ensemble of ice crystals since this represents the simplest arrangement of ice crystals.

A fundamental hindrance to simulating the light scattering of ice crystals is the difficulty of obtaining realistic representations of natural ice crystals arising primarily from their complex particle shapes. Individual ice crystal structure is affected by a number of factors including the temperature, humidity, and pressure at which ice crystals form [*Bailey and Hallett*, 2004; *Baker and Lawson*, 2006; *Kajikawa and Heymsfield*, 1989; *Kobayashi*, 1961; *Lawson et al.*, 2006]. Several physical processes can further modify the appearance of ice crystals during their vertical motion within clouds. Ice crystals can become unidentifiable aggregates when they fall through the cloud layer and collide with supercooled water droplets or other ice crystals. Additionally, the surfaces of ice crystals are generally not perfectly smooth due to collisions, coalescence, and other fragmenting processes. Although the exact mechanism for forming various ice crystal habits is not well understood, hexagonal columns and plates are known to be the important habits of ice crystals commonly found in cirrus clouds. This has been confirmed by both *in situ* measurements of cirrus clouds and the optical phenomena that 22° halos, caused by sunlight refracted by hexagonal ice crystals, are usually seen when the sky is overspread with thin cirrus clouds [*Coleman and Liou*, 1981; *Sassen et al.*, 1994].

Based on the ice crystal habit and size distributions obtained from *in situ* measurements and the work conducted to simulate light scattering by nonspherical particles [*Baran et al.*, 2001b; *Cai and Liou*, 1982; *Fu et al.*, 1999; *Hess and Wiegner*, 1994; *Macke and Mishchenko*, 1996; *Macke et al.*, 1996a; *Macke et al.*, 1996b; *Takano*

and Liou, 1995; *Yang and Liou*, 1996a; *Yang and Liou*, 1996b; *Yang and Liou*, 1997; *Yang and Liou*, 1998], ice crystals with hexagonal structures are often assumed in the retrievals of cirrus cloud microphysical and optical properties from satellite observations [*Chepfer et al.*, 2001; *King et al.*, 2004; *Li et al.*, 2005; *Minnis et al.*, 1993; *Minnis et al.*, 1998b; *Minnis et al.*, 2004; *Minnis et al.*, submitted]. A mixture of more complicated ice crystal shapes has also been suggested for ice cloud optical models [*Baum et al.*, 2000; *Baum et al.*, 2005a; *Baum et al.*, 2005b; *Baum et al.*, 2007]. The quality of the satellite retrieval depends on the accuracies of the scattering properties used to represent natural hexagonal ice crystals in cirrus clouds and the resulting simulated cirrus cloud solar reflectances.

Efforts have been made to study the sensitivity of certain morphological parameters of hexagonal ice crystals to the single-scattering properties of ice crystals. There are a number of published studies on the optical properties of inhomogeneous ice crystals containing air bubbles and other inclusions. Among these previous studies, *Macke et al.* [1996a; 1996b] employed a combination of the ray-tracing technique and the Monte Carlo method to investigate the single-scattering properties of randomly oriented hexagonal ice columns containing ammonium sulfate inclusions, air bubbles and soot impurities. In their computations, the scattering events at the outer boundary of a hexagonal particle are considered by using the ray-tracing technique [*Macke*, 1993] whereas the Monte Carlo method is used to account for the ray-path changes due to the internal inclusions. *Yang et al.* [2000] used the FDTD technique to compute the scattering phase functions of small ice crystals with inclusions of soot impurities and air bubbles. *Labonnote et al.* [2001] developed an Inhomogeneous Hexagonal Monocrystals (IHM)

model for ice crystals containing randomly located air bubbles and mineral aerosols. This single-scattering property model, based on the ray-tracing and Monte Carlo techniques developed by *Macke et al.* [1996b], has further defined the internal air bubbles in terms of spherical voids with a size distribution. *Labonnote et al.* [2001] and *Knap et al.* [2005] used the IHM model to investigate the bulk-scattering properties of ice clouds and to compare the simulations with satellite-based measurements of polarized radiances. The IHM model does not account for the case where an ice crystal contains only a few air bubbles with specific locations. The geometries of air bubbles in the previous studies were restricted to the assumption of spheres, a constraint that is not always realistic. A new inhomogeneous ice crystal model based on observations is demanded in the study of the scattering properties of ice clouds. Furthermore, the effects of the air bubbles on the retrieval of cloud optical thicknesses and effective particle sizes are also pending issues.

The representation of aggregated ice particles in cloud studies is another area needing further refinement and clarification. Current ice cloud bulk scattering and absorption models used in the operational Moderate Resolution Imaging Spectroradiometer (MODIS) cloud property retrievals involve a percentage of roughened aggregates with large maximum dimensions [*Baum et al.*, 2005a; *Baum et al.*, 2005b]. A specific aggregate geometry defined by *Yang and Liou* [1998], includes eight hexagonal columns. The aggregate dimension can be scaled when each hexagonal column is enlarged or reduced while the aspect ratio is kept to be invariant. The ice aggregate model was modified into a chain-like aggregate by *Baran and Labonnote* [2006] and used for remote sensing applications based on the Polarisation and Directionality of Earth's Reflectances (POLDER) data. The original model was transformed into the chain-like

aggregates by stretching and rotating two of the original hexagonal columns to make the aggregate particle less dense (i.e., decrease the volume to area ratio) and, therefore, to better fit the *in situ* observations.

Evans et al.[2005] generated three types of aggregates consisting of 6-40 randomly oriented hexagonal columns and plates. Each aggregate monomer had a predetermined aspect ratio and particle size, and a larger particle was constructed by interlocking the fixed monomers. The discrete dipole approximation (DDA) method [*Evans and Stephens*, 1995; *Kahnert*, 2003] was used to compute the scattering properties of the aggregates for application to the simulation of the radiances measured by the Compact Scanning Submillimeter Imaging Radiometer (CoSSIR) and the Cloud Radar System (CRS) on NASA's ER-2 aircraft. The aggregate ice particles were represented in the DDA code with each dipole size set to be the thickness of a hexagonal plate monomer. *Um and McFarquhar* [2009] defined geometries of aggregates using ice particles formed from seven hexagonal plates, and the scattering properties of the aggregates were computed by the geometric ray-tracing technique [*Cai and Liou*, 1982; *Macke*, 1993; *Macke et al.*, 1996b; *Um and McFarquhar*, 2007; *Um and McFarquhar*, 2009]. However, it is still unknown that how well the previous aggregate models represent the realistic aggregates within cirrus clouds. A new set of aggregate ice particles is needed to minimize the differences of the scattering properties between the modeled and real aggregates.

Quantifying the morphological parameters (i.e. degrees of ice crystal surface roughness and inhomogeneity) and habit distributions of the ice crystals used in the operational retrieval of cloud properties would help minimize the effect of the spatial and

temporal limitations of the *in situ* and surface observations of atmospheric ice crystals. In other words, a robust algorithm is needed to fast and accurately find the most appropriate ice crystal configurations to minimize the uncertainties introduced by the use of any particular ice cloud model. *Doutriaux-Boucher et al.* [2000] derived ice cloud optical thicknesses based on the Polarization and Directionality of the Earth's Reflectances (POLDER) observations of radiances in 14 different viewing directions. Cloud spherical albedos were computed using the retrieved optical thicknesses over 'super-pixels' consisting of 9×9 elementary pixels, each of which corresponds to a spatial resolution of approximately 60 km × 60 km. The error caused by the use of ice crystal habits and their scattering properties was inferred through the departure of the spherical albedos derived from their averaged values in conjunction with the 14 view angles. This algorithm was followed by studies aimed at improving the scattering properties of cirrus clouds [*Baran and Labonnote*, 2006; *Labonnote et al.*, 2001] or retrieving ice crystal habits [*Baran et al.*, 2001a; *Chepfer et al.*, 2001; *Chepfer et al.*, 2002; *Sun et al.*, 2006] using POLDER multiangle radiance measurements. *McFarlane et al.* [2005] developed a method of retrieving cloud thermodynamic phase and ice crystal habit using the Multiangle Imaging Spectroradiometer (MISR) and Moderate Resolution Imaging Spectroradiometer (MODIS) data. They assessed the accuracy of ice crystal habits by studying the relative deviation of the computed cloud reflectances and those measured by 9 MISR cameras and averaged over a 10 km × 10 km box at the Atmospheric Radiation Measurement (ARM) Southern Great Plains (SGP) site. The retrieval of ice crystal habits was reasonably consistent with *in situ* observations of cirrus clouds.

The differences in retrieved cloud optical properties caused by using measurements taken at different satellite viewing directions can arise from other factors besides ice cloud habits. Theoretical studies [*Davies*, 1984; *Iwabuchi and Hayasaka*, 2002; *Loeb and Davies*, 1997; *Loeb and Coakley*, 1998] have indicated the horizontal inhomogeneity of clouds or the 3D radiative effect may lead 1D retrievals to under- or overestimate cloud reflectances and optical thicknesses due to cloud-side shadowing or illumination. However, because of its complexity, this effect has typically been ignored in current operational retrieval of cloud properties. Moreover, the biases in cloud property retrievals introduced from viewing geometries can be partially eliminated when the results are averaged over several pixels [*Kato and Marshak*, 2009; *Oreopoulos and Davies*, 1998]. Thus, the improvement of pixel-by-pixel retrievals of cloud properties is more meaningful if the errors are investigated using similar spatial resolution.

This doctoral research seeks to compute the single-scattering properties of realistic ice crystals based on *in situ* measurements. The scattering properties of the single ice crystals are then used to improve the current ice cloud models for satellite-based remote sensing of cirrus clouds. This dissertation is organized as follows. Chapter II discusses the effect of the inhomogeneity of ice crystals on retrieving ice cloud optical thickness and effective particle size. Chapter III presents a representation of ice particle aggregates within cirrus clouds. The scattering properties of the aggregates are applicable in the remote sensing of ice clouds. Chapter IV introduces an algorithm to retrieve ice cloud optical thicknesses using MODIS and MISR data. The error caused by ice cloud models and their scattering properties is addressed through analyses of viewing angle dependence of the retrieved cloud optical thicknesses. An appropriate ice cloud model is

determined for application to satellite-based retrieval of ice cloud properties. Chapter V concludes this research.

CHAPTER II

EFFECT OF THE INHOMOGENEITY OF ICE CRYSTALS ON RETRIEVING ICE CLOUD OPTICAL THICKNESS AND EFFECTIVE PARTICLE SIZE*

2.1 Background

An appropriate representation of ice clouds in radiative transfer simulations has long been a subject of great interest, not only because of their importance for cloud radiative forcing and the energy budget of the earth, but also because of the uncertainties associated with the shapes and sizes of ice crystals within these clouds [*Baran*, 2004; *Liou*, 1986; *Ramanathan et al.*, 1983]. Although approximating the single-scattering properties (e.g., phase function, single-scattering albedo and asymmetry factor) of realistic ice crystals by assuming one idealized geometrical shape is an oversimplification [*Baum et al.*, 2005a; *Baum et al.*, 2005b] it is significantly better for retrieving ice cloud properties than assuming that the clouds are composed of spherical ice crystals [*Minnis et al.*, 1993]. However, a more accurate representation of cirrus cloud ice crystal properties is needed. For example, the use of homogeneous hexagonal ice crystals [*Minnis et al.*, 1998a] can yield accurate estimates of ice water path [*Mace et al.*, 2005] but the retrieved optical depth values tend to be low [*Min et al.*, 2004] implying an overestimate of the effective particle size. To further improve the representation of cloud ice crystals in

---

*Reprinted with permission from "Effect of the inhomogeneity of ice crystals on retrieving ice cloud optical thickness and effective particle size", by Xie, Y., P. Yang, G. W. Kattawar, P. Minnis, and Y. X. Hu, 2009. *J. Geophys. Res*. 114, doi: 10.1029/2008JD011216.

radiative transfer calculations, steady progress has been made toward single-scattering computations involving various complex particle shapes.

Liou [1972] first assumed nonspherical ice crystals to be long circular cylinders, and demonstrated the significant differences in the phase functions between polydisperse spheres and equivalent long circular cylinders. *Takano and Liou* [1989], *Muinonen* [1989], *Hess and Wiegner* [1994], *Borovoi and Grishin* [2003] and many others applied the traditional ray-tracing method or its modified forms to the scattering of radiation by randomly and horizontally oriented hexagonal particles. The optical properties of various complicated ice crystals have also been simulated from the geometric optics method by *Hess et al.*[1998], *Macke* [1993], *Macke et al.*[1996a], *Iaquinta et al.*[1995], *Takano and Liou* [1995], *Yang and Liou* [1998], *Baran and Labonnote* [2006; *Baran and Labonnote*, 2007], *Um and McFarquhar* [2007], *Schmitt et al.*[2006], and *Yang et al.*[2008a; 2008b; 2008c]. Furthermore, *Yang and Liou* [1996a] employed the finite-difference time domain (FDTD) method to simulate the scattering of light by small bullet-rosettes, hexagonal plates, solid columns, and hollow columns.

In the previously reported studies on the single-scattering properties of irregular ice particles, homogeneous ice crystal morphologies were usually assumed. In the accretion and aggregation of ice crystals, an ice particle may collide with supercooled water droplets or other ice particles. When this happens, ice crystals can rapidly grow to form large ice crystals. The collision and coalescence processes may lead to the trapping of spherical or spheroidal air bubbles within ice crystals when the supercooled water droplets freeze almost instantly. Air bubbles may be incorporated when water containing dissolved air freezes into ice crystals. Supercooled water drops may turn into ice [*Hallett*,

1964]. The freezing process starts at the particle surface and slowly proceeds inward. This inward growth of the ice may cause the previously dissolved air to be released and subsequently form small bubbles within the ice particle. The size and concentration of air bubbles are then influenced by the rate of freezing, amount of dissolved air in water and temperature during the freezing process [*Carte*, 1961; *Hallett*, 1964].

This chapter reports on a new inhomogeneous ice crystal model based on the surface observations reported by *Tape* [1994]. Furthermore, the effects of the air bubbles on the retrieval of cloud optical thickness and effective particle sizes are also investigated. This chapter is organized as follows. In Section 2.2, we describe the morphologies of ice crystals observed by *Tape* [1994] and define the geometries of the inhomogeneous ice crystals for the present scattering computations. Then, we introduce the single-scattering model based on an improved geometrical-optics method (IGOM [*Yang and Liou*, 1996b]). In Section 2.3, we illustrate the effect of the number, shape, size, and location of the air bubbles inside hexagonal ice crystals on the single-scattering properties of these particles. In Section 2.4, we demonstrate the effects of accounting for air bubbles in defining ice crystal morphology on the retrieval of ice cloud optical thickness and effective particle size. Moreover, we derive cloud microphysical and optical properties based on the Moderate Resolution Imaging Spectroradiometer (MODIS) measurements from a bi-spectral method originally developed by *Nakajima and King* [1990] and compare the retrieval results from homogeneous and inhomogeneous ice crystal models. The conclusions and discussions of this study are given in Section 2.5.

2.2 Single-scattering model for inhomogeneous ice crystals

Although the geometries of ice crystals in the atmosphere have been extensively studied on the basis of airborne *in situ* observations [*Heymsfield and Platt*, 1984; *Korolev et al.*, 1999; *McFarquhar and Heymsfield*, 1996], ground-based observations also provide useful data for investigating ice crystal morphologies. *Tape* [1983; 1994] used Petri dishes containing hexane or silicone oil and acrylic spray to collect ice crystals falling near the surface and observed the ice crystal shapes using a binocular microscope. Figure 2.1 illustrates the ice crystals sampled by *Tape* [1994] at the South Pole on January 19, 1985 and on January 17, 1986. In the photographs, the ice crystals have typical hexagonal shapes and most of these particles are inhomogeneous with embedded air bubbles. The observed inhomogeneous ice crystals spurred development of the theoretical models used by *Macke et al.* [1993] and *Labonnote et al.* [2001] to compute the single-scattering properties of these particles. However, unlike the crystal geometries in the IHM model [*Labonnote et al.*, 2001], an inhomogeneous ice crystal usually contains a few air bubbles with visible dimensions. The sizes of the air bubbles are relatively large, as the maximum dimensions of the air bubbles are comparable with the width of the ice crystal. Another significant difference between the observations by *Tape* [1994] and the IHM model is that the actual air bubbles are not always spheres, although most of them have spherical shapes. Moreover, the air bubbles are located almost exclusively along the symmetry axes of hexagonal columns. However, for hexagonal plates, more than one air bubble can be horizontally aligned near the surface of the particles.

Based on the ice particles photographed by *Tape* [1994], the geometries of inhomogeneous ice crystals in this study are defined as those shown in Fig. 2.2. For

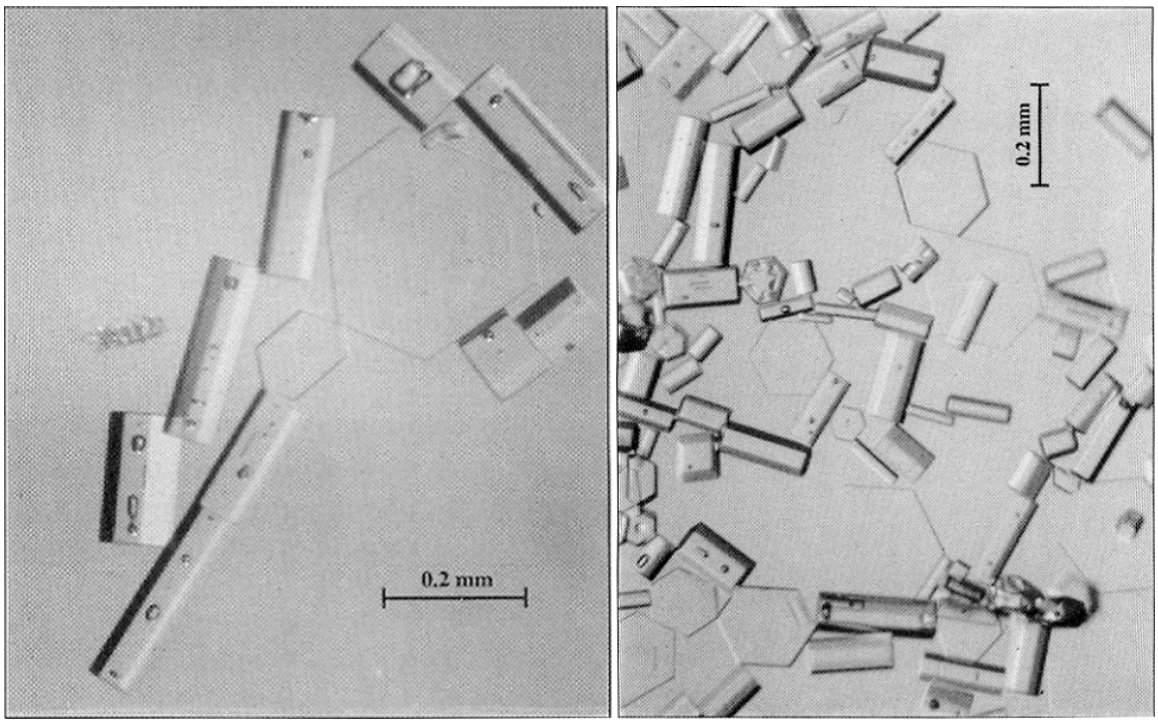

Fig. 2.1 Inhomogeneous ice crystals sampled by Walter Tape [*Tape*, 1994] at the South Pole, on January 19, 1985 (left) and on January 17, 1986 (right).

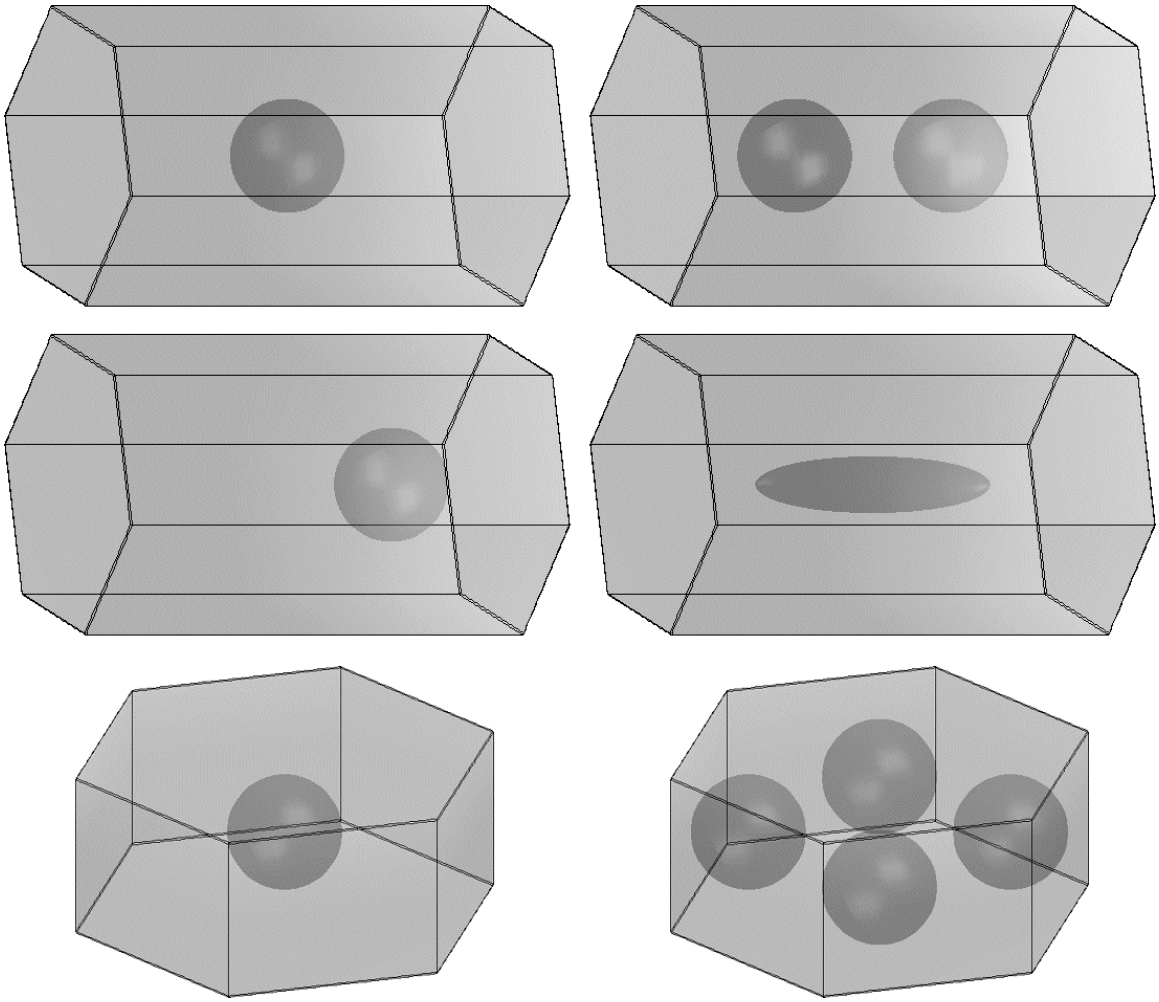

Fig. 2.2 The geometries of inhomogeneous ice crystals.

hexagonal columns, only one or two air bubbles are included within ice particles. Furthermore, the air bubble inclusions in our model are all on the axes of ice crystals (see the upper and middle panels in Fig. 2.2). For hexagonal plates, the air bubbles are aligned horizontally if more than one air bubble is included (see the lower panels in Fig. 2.2). The orientations of ice crystals for either hexagonal columns or plates are specified in the OXYZ coordinate system denoted in Fig. 2.3. Following *Yang and Liou* [1996b], the Y-axis in Fig. 2.3 is perpendicular to one of the ice crystal's side faces, and the Z-axis is along the vertical axis of the hexagon. The shape of an air bubble is defined in terms of the following equation:

$$\frac{(x-x_r)^2}{r_1^2}+\frac{(y-y_r)^2}{r_2^2}+\frac{(z-z_r)^2}{r_3^2}=1, \tag{2.1}$$

where r_1, r_2, and r_3 are the three semi-axes along the X, Y and Z axes, respectively, and the coordinates (x_r, y_r, z_r) specify the center of the air bubble in the OXYZ system.

In this study, the IGOM developed by *Yang and Liou* [1996b] is used to compute the single-scattering properties of inhomogeneous ice crystals. At the outer boundary of the inhomogeneous ice crystals, the computation of reflection and refraction events is the same as in the case for homogeneous hexagonal ice crystals. Since IGOM is based partly on the principles of geometric optics, very small air bubbles are not considered in the present study. The technical details and applicability of the IGOM are reported and discussed in *Yang and Liou* [1996b].

If a ray is refracted into an ice crystal, the next step is to trace the refracted ray and determine if it is intersected by any air bubble within the particle. Figure 2.4 shows the flow-chart for reflection and refraction by internal air bubbles. For an air bubble with

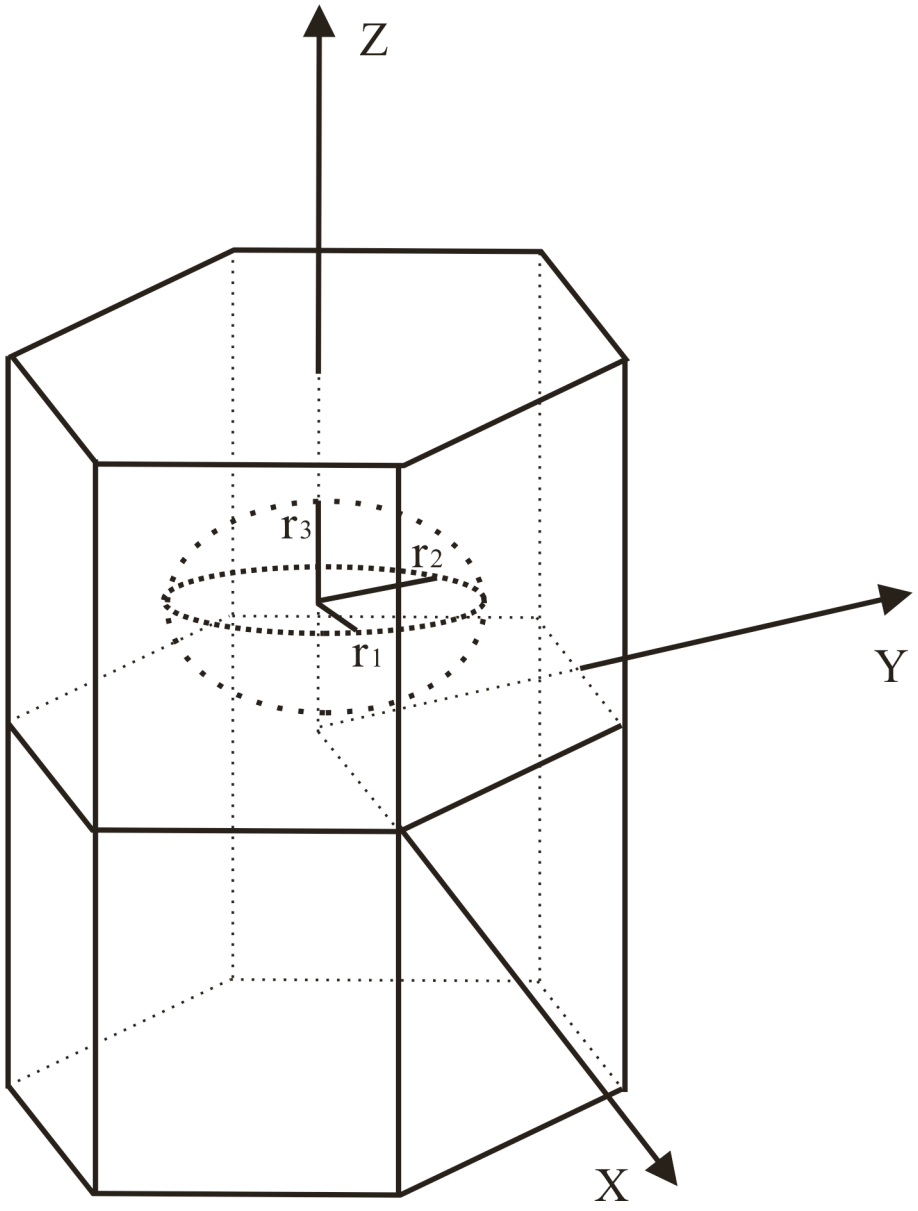

Fig. 2.3 Geometry of a hexagonal ice crystal with an air bubble inside.

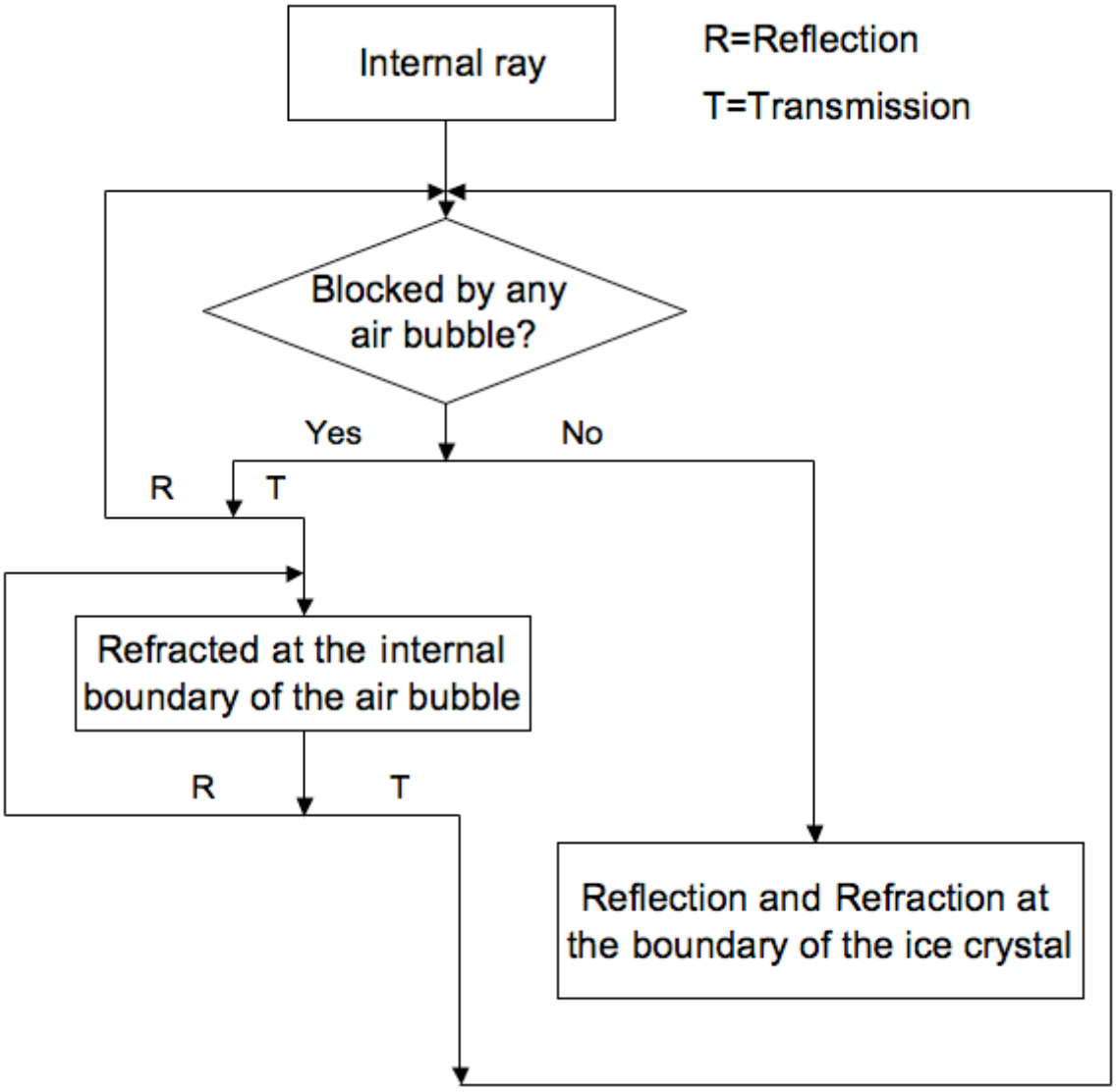

Fig. 2.4 Schematic flow-chart for reflection and refraction by internal air bubbles.

the particle shape given by Eq. (2.1), the coordinates of the incident point B, (x_b, y_b, z_b), can be determined as follows:

$$x_b = x_a + (\hat{e} \cdot \hat{x})l, \tag{2.2}$$

$$y_b = y_a + (\hat{e} \cdot \hat{y})l, \tag{2.3}$$

$$z_b = z_a + (\hat{e} \cdot \hat{z})l, \tag{2.4}$$

where the coordinates (x_a, y_a, z_a) indicate the position of the first incident point, A, at the ice crystal surface, $\hat{e}$ is a unit vector along the incident direction, $\hat{x}$, $\hat{y}$, and $\hat{z}$ are unit vectors along the X, Y, and Z axes, respectively, and l is the distance between points A and B. Substituting Eqs. (2.2)-(2.4) into Eq. (2.1), we obtain

$$A_1 l^2 + A_2 l + A_3 = 0, \tag{2.5}$$

where

$$A_1 = r_2^2 r_3^2 (\hat{e} \cdot \hat{x})^2 + r_1^2 r_3^2 (\hat{e} \cdot \hat{y})^2 + r_1^2 r_2^2 (\hat{e} \cdot \hat{z})^2, \tag{2.6}$$

$$A_2 = 2r_2^2 r_3^2 (x_a - x_r)(\hat{e} \cdot \hat{x}) + 2r_1^2 r_3^2 (y_a - y_r)(\hat{e} \cdot \hat{y}) + 2r_1^2 r_2^2 (z_a - z_r)(\hat{e} \cdot \hat{z}), \tag{2.7}$$

$$A_3 = r_2^2 r_3^2 (x_a - x_r)^2 + r_1^2 r_3^2 (y_a - y_r)^2 + r_1^2 r_2^2 (z_a - z_r)^2 - r_1^2 r_2^2 r_3^2. \tag{2.8}$$

A ray will intercept an air bubble when A_1, A_2, and A_3 satisfy

$$A_2^2 - 4A_1 A_3 > 0, \tag{2.9}$$

and

$$\frac{-A_2 - \sqrt{A_2^2 - 4A_1 A_3}}{2A_1} > 0. \tag{2.10}$$

The directions of the reflected and refracted rays, $\hat{e}_r$ and $\hat{e}_t$ can be determined on the basis of Snell's law in the form

$$\hat{e}_r = \hat{e} - 2(\hat{e} \cdot \hat{n})\hat{n}, \tag{2.11}$$

$$\hat{e}_t = N_r[\hat{e} - (\hat{e} \cdot \hat{n})\hat{n} - \sqrt{N_r^{-2} - 1 + (\hat{e} \cdot \hat{n})^2}\,\hat{n}], \tag{2.12}$$

where N_r is the real part of the effective refractive index formulated by *Yang and Liou* [1995] and $\hat{n}$ is the normal direction of the air-bubble surface at point B. For spheroidal air bubbles used in this study, $\hat{n}$ can be given by

$$\hat{n}_x = \frac{x_b - x_r}{r_1^2} \Bigg/ \sqrt{\left(\frac{x_b - x_r}{r_1^2}\right)^2 + \left(\frac{y_b - y_r}{r_2^2}\right)^2 + \left(\frac{z_b - z_r}{r_3^2}\right)^2}, \tag{2.13}$$

$$\hat{n}_y = \frac{y_b - y_r}{r_2^2} \Bigg/ \sqrt{\left(\frac{x_b - x_r}{r_1^2}\right)^2 + \left(\frac{y_b - y_r}{r_2^2}\right)^2 + \left(\frac{z_b - z_r}{r_3^2}\right)^2}, \tag{2.14}$$

$$\hat{n}_z = \frac{z_b - z_r}{r_3^2} \Bigg/ \sqrt{\left(\frac{x_b - x_r}{r_1^2}\right)^2 + \left(\frac{y_b - y_r}{r_2^2}\right)^2 + \left(\frac{z_b - z_r}{r_3^2}\right)^2}. \tag{2.15}$$

For a ray refracted into the air bubble, the next impinging point C, (x_c, y_c, z_c), on the air-bubble surface can be determined as follows:

$$x_c = x_b + (\hat{e}_t \cdot \hat{x})l', \tag{2.16}$$

$$y_c = y_b + (\hat{e}_t \cdot \hat{y})l', \tag{2.17}$$

$$z_c = z_b + (\hat{e}_t \cdot \hat{z})l', \tag{2.18}$$

where l' is the distance between points B and C. l' can be solved from Eqs. (2.5)-(2.8) by replacing l and $\hat{e}$ by l' and $\hat{e}_t$, respectively.

If the conditions in Eqs. (2.9) and (2.10) are not satisfied, i.e., the incident ray does not impinge upon the air bubble centered at (x_r, y_r, z_r), the ray-tracing procedure needs to be repeated for another air bubble if more than one air bubble is embedded in the ice crystal of interest.

2.3 Single-scattering properties of inhomogeneous ice crystals

Figure 2.5 compares the scattering phase functions for homogeneous ice crystals with their inhomogeneous ice crystal counterparts at the wavelengths (λ) of 0.65 and 2.13 μm. The refractive indices of ice at these wavelengths are $1.3080 + i1.43\times10^{-8}$ and $1.2673 + i5.57\times10^{-4}$, respectively. The ice crystals are assumed to be randomly oriented hexagonal columns and plates with aspect ratios $2a/L$=80 μm/100 μm and 100 μm/43 μm, respectively, where a is the radius of a cylinder that circumscribes the hexagonal ice particle and L is the length of the ice particle. Specifically, Fig. 2.5a shows the phase functions at λ=0.65 μm for homogeneous hexagonal columns and inhomogeneous columns with the same aspect ratio. For the two inhomogeneous conditions, spherical air bubbles with radii of 16 or 34 μm are centered in the middle of ice crystals. It is then evident from Fig. 2.5a that the air bubbles within ice crystals can greatly affect the scattering properties of ice particles. In the homogeneous case, the 22° and 46° halo peaks are quite pronounced, which are typical for the scattering of light by randomly oriented pristine hexagonal ice crystals. However, the magnitudes of the peaks at the scattering angles 22° and 46° are reduced if a small air bubble with a radius of 16 μm is embedded in the crystal. For ice crystals containing relatively large air bubbles with a radius of 34 μm, the 22° and 46° peaks are significantly smoothed out in the scattering phase function although they are still slightly noticeable. Furthermore, the backscattering is substantially reduced in the inhomogeneous case. It should be noted that a bubble embedded in ice acts as a diverging lens and affects internal rays; however, the forward peaks are essentially unaffected by bubbles since diffraction, which depends primarily on the particle projected area, is the primary cause. Figure 2.5b shows the scattering phase

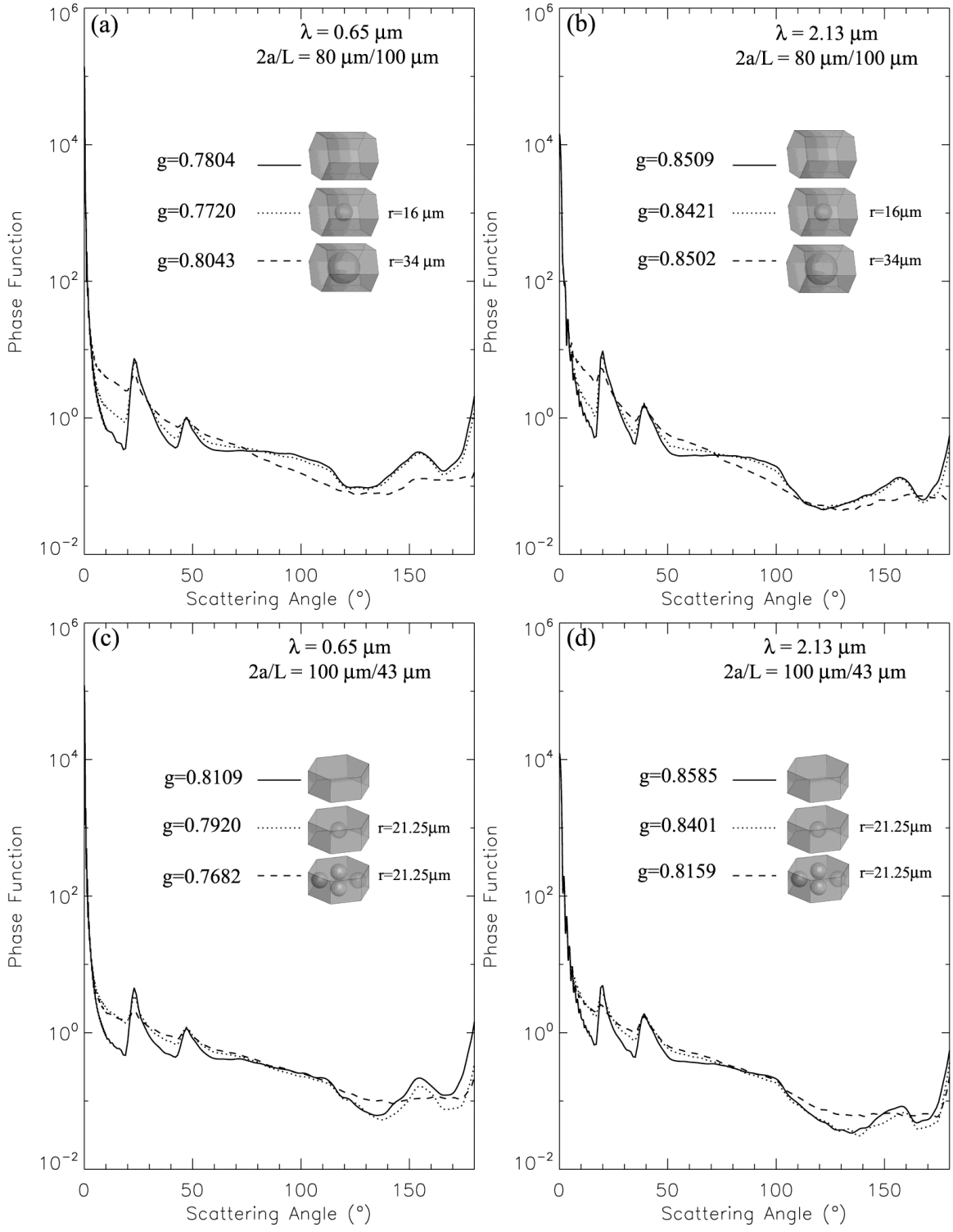

Fig. 2.5 Scattering phase functions for homogeneous and inhomogeneous ice crystals at λ=0.65 μm (panels a and c) and 2.13 μm (panels b and d).

functions for homogeneous and inhomogeneous hexagonal columns at λ=2.13 μm. The effect of air bubbles at the near-infrared wavelength is similar to that in the case for visible wavelengths. Figure 2.5c shows the scattering phase functions of hexagonal plates at λ=0.65 μm. In this panel, the dotted line describes the phase function for inhomogeneous ice crystals containing a spherical air bubble with a radius of 21.25 μm. For the other inhomogeneous case, four air bubbles with the same size are aligned parallel to the basal faces of the plates. Comparable to the effect in the hexagonal columns, the air bubbles in hexagonal plates smooth the scattering phase function and reduce the backscatter. The phase function values at scattering angles larger than 120º are quite sensitive to the number of air bubbles in hexagonal plates. A similar effect of air bubbles on the single-scattering properties is also seen in Fig. 2.5d for a wavelength of 2.13 μm.

Figure 2.6 shows a measure of linear polarization, $-p_{12}/p_{11}$, for ice crystals having the same aspect ratios and inhomogeneities as those in Fig. 2.5. Figures 2.6a and 2.6b compare the degrees of linear polarization between homogeneous and inhomogeneous hexagonal columns. It is seen that air bubbles embedded within ice crystals can also reduce the magnitude of the degree of linear polarization, particularly, in the case of large air bubbles. The same effect can also be found for hexagonal plates, whose scattering phase functions are shown in Figures 2.6c and 6d at λ=0.65 μm and λ=2.13 μm, respectively. However, unlike the scattering phase functions in Fig. 2.5, increasing the number of air bubbles in hexagonal plates enhances the smoothing of the degree of linear polarization.

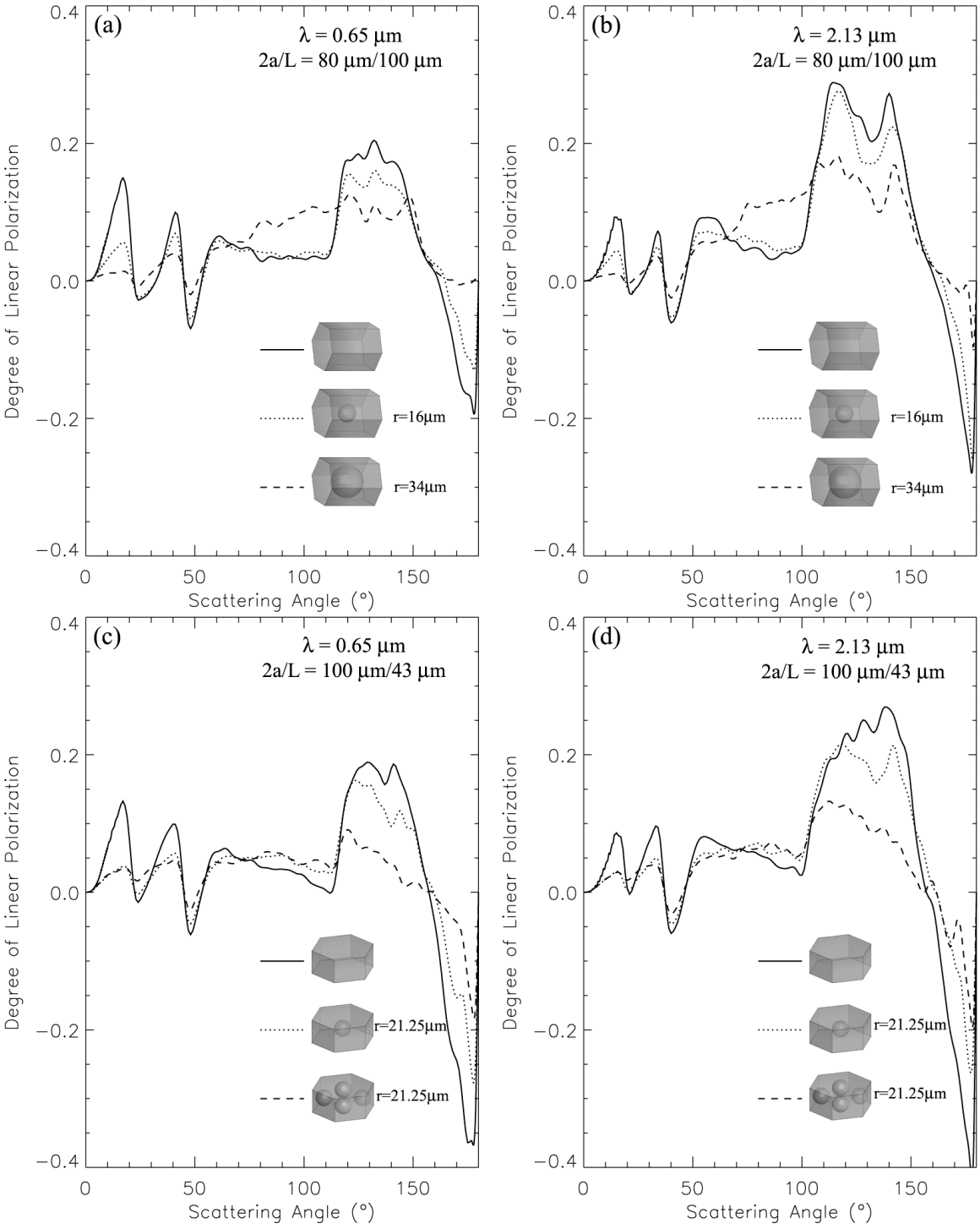

Fig. 2.6 Degrees of linear polarization for homogeneous and inhomogeneous ice crystals at λ=0.65 μm (panels a and c) and 2.13 μm (panels b and d). The ice crystals' sizes and morphologies in this figure are the same as those in Fig. 2.5.

Figure 2.7 shows the phase matrices for hexagonal columns at λ=0.65 μm. To specify the effects of the shapes of air bubbles on the single-scattering properties of ice crystals, three hexagonal column (2a/L=50 μm /100 μm) cases are considered: a homogeneous ice crystal, an inhomogeneous ice crystal with a spherical air bubble (radius=10.0 μm), and an inhomogeneous ice crystal with a volume-equivalent spheroid bubble. It is evident from Fig. 2.7 that spheroidal air bubbles have a greater effect on the phase matrix than those containing spherical air bubbles. This feature is physically understandable since for the same volume, a spherical particle has the smallest cross section on average among all solid particles, and an incident ray has a smaller chance to be intercepted by spherical air bubbles than their counterparts with other shapes. In addition to the phase function and degree of linear polarization, the other elements of the phase matrix are also sensitive to the presence of air bubbles.

To further illustrate the effect of air bubbles on the single-scattering properties of ice crystals, Fig. 2.8 shows the asymmetry factor as a function of the volume of the air bubbles at λ=0.65 μm and λ=2.13 μm. The aspect ratio of ice crystals is 2a/L=10 μm/50 μm. Spherical air bubbles are located at the center of the ice crystals where the radii r_1 and r_2 in Eq. (2.1) are the same. The relative volume of the air bubble, V_b/V, can be specified in terms of the radii, where V_b and V are the volumes of the air bubbles and ice crystals, respectively. It is seen from Fig. 2.8 that the asymmetry factor decreases at both visible and near-infrared wavelengths when small air bubbles are included. The asymmetry factor reaches its minimum value with increasing V_b/V and may increase when back-scattering is significantly reduced by considering extremely large air bubbles.

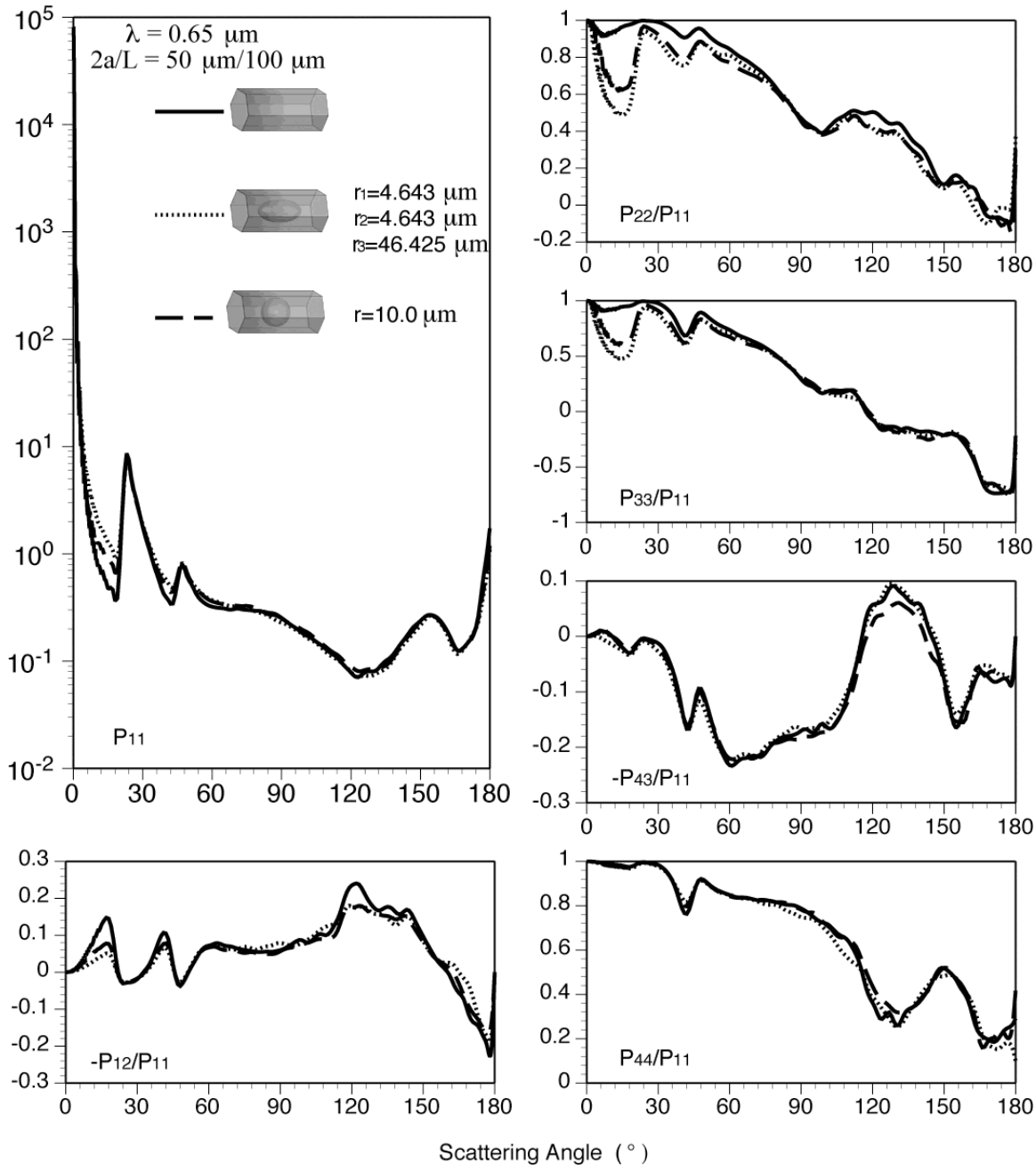

Fig. 2.7 Scattering phase matrixes for homogeneous and inhomogeneous ice crystals at λ=0.65 μm.

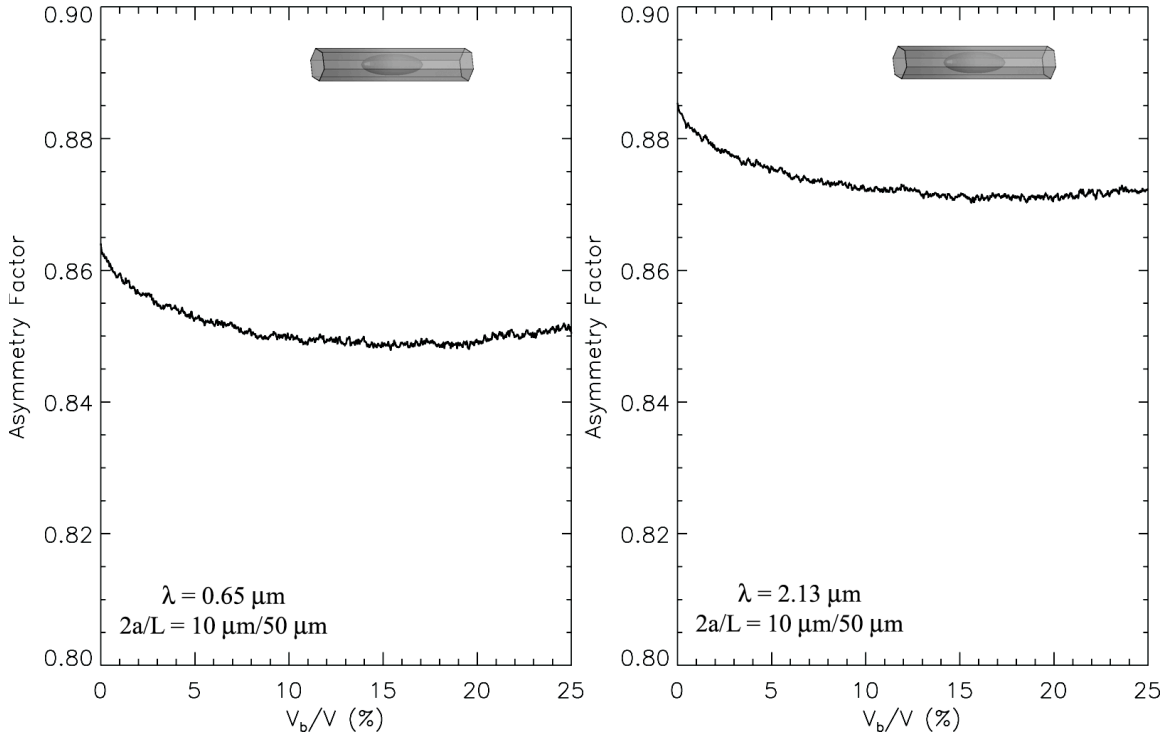

Fig. 2.8 Asymmetry factors for inhomogeneous ice crystals at λ=0.65 μm (left) and 2.13 μm (right).

These features are found to be applicable to all the inhomogeneous ice crystals containing one air bubble shown in Fig. 2.2.

2.4 Effect of inhomogeneous ice crystals on ice cloud retrieval

The single-scattering properties of ice crystals are fundamental to the development of the lookup tables required for satellite-based ice cloud retrieval algorithms. At present, substantial uncertainties exist in ice cloud property retrievals due to inadequate representation of complex ice crystal morphologies and, consequently, inaccurate knowledge about their single-scattering properties. Inhomogeneous ice crystal morphology is one of the least understood aspects in defining realistic ice crystal geometries. Additional *in situ* measurements are required to quantify the occurrence frequency of air bubbles within ice crystals and their importance in radiative transfer simulations and remote sensing applications.

To study the effect of inhomogeneous ice crystals on retrieving ice cloud properties, aspect ratios of ice crystals as well as particle size distributions are required. In this sensitivity study, an aspect ratio of 2a/L=0.2 is used for all ice crystals, although it may not correspond well to observations [*Ono*, 1969]. Realistic aspect ratios are needed in future studies. Furthermore, small (r_1=0.45a, r_2=0.45a, and r_3=0.2L) and relatively large (r_1=0.85a, r_2=0.85a, and r_3=0.2L) air bubbles are defined at the center of each inhomogeneous ice crystal. The size distribution of ice crystals is assumed to obey a Gamma distribution given by

$$n(L) = N_0 L^{\mu} \exp(\frac{b+\mu+0.67}{L_m} L), \tag{2.19}$$

where N_0 is the intercept, μ is assumed to be 2 in this study, and L_m is the median of the distribution of L. The parameter b is taken to be 2.2. The effective particle size for a given size distribution is defined as follows [*Foot*, 1988]:

$$r_e = \frac{3\int_{L_{\min}}^{L_{\max}} V(L)n(L)dL}{4\int_{L_{\min}}^{L_{\max}} A(L)n(L)dL}, \tag{2.20}$$

where V is particle volume, and A is projected area.

The ice cloud bi-directional reflectances are computed using the Discrete Ordinates Radiative Transfer (DISORT) model [*Stamnes et al.*, 1988] for λ = 0.65 and 2.13 μm at various incident-scattering configurations. The visible optical thickness at λ = 0.65 μm serves as the reference optical thickness in this study. The optical thickness for a given wavelength is related to the visible optical thickness via

$$\tau = \frac{\tau_{vis} Q}{Q_{vis}}, \tag{2.21}$$

where Q and Q_{vis} are the extinction efficiencies for λ=2.13 and 0.65 μm, respectively.

Figure 2.9a shows the comparison of the lookup tables computed for the solid homogeneous ice crystals and the inhomogeneous ice crystals containing small air bubbles (r_1= r_2=0.45a, and r_3=0.2L). It is seen that the inhomogeneous ice crystals reflect slightly more than the homogeneous ice crystals at λ = 0.65 μm whereas the bi-directional reflectances for the inhomogeneous ice crystals are significantly larger than those for the homogeneous particles at λ = 2.13 μm. Figure 2.9b is the same as Fig. 2.9a except that each inhomogeneous ice crystal in Fig. 2.9b contains larger air bubbles with radii of r_1= r_2=0.85a, and r_3=0.2L. It is then evident that the bidirectional reflectances at λ

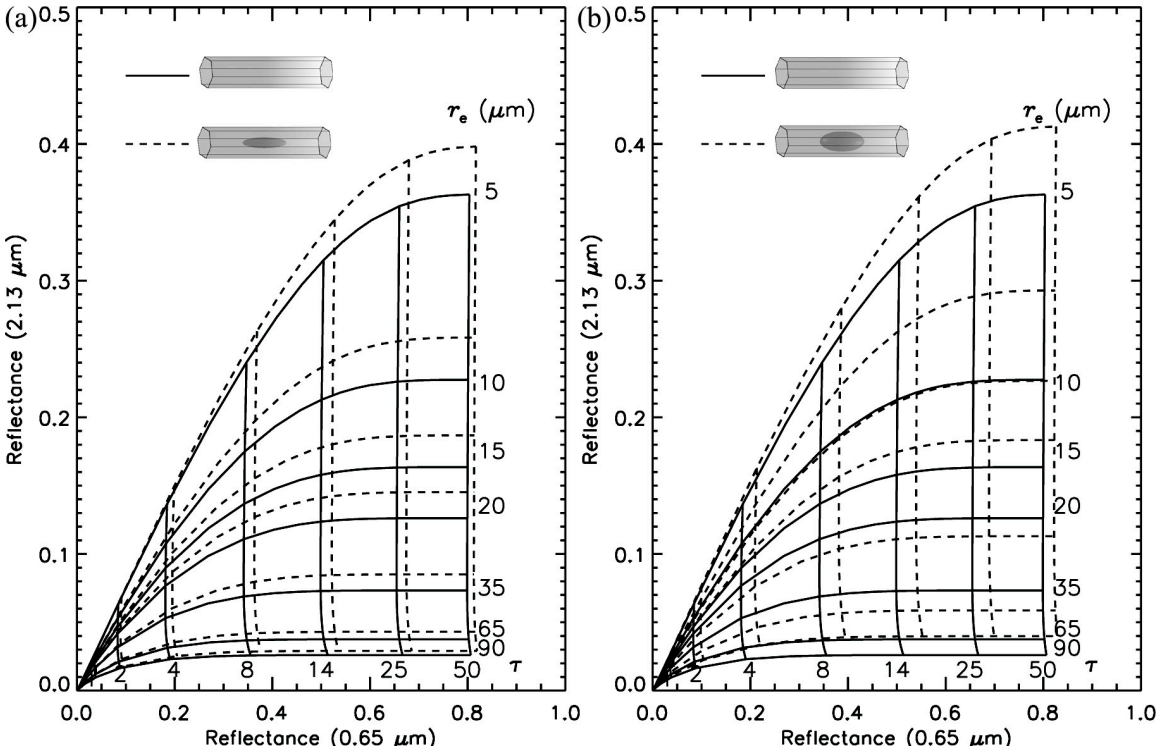

Fig. 2.9 Lookup tables using 0.65 and 2.13 μm reflectances for homogeneous and inhomogeneous cloud models. μ_0=0.65, μ=1.0 and $\varphi - \varphi_0 = 0°$.

= 0.65 μm are slightly sensitive to the air bubble size. However, large air bubbles in the ice crystals can significantly increase the reflectances at λ = 2.13 μm.

The left and right panels in the top of Fig. 2.10 show a MODIS granule image over the south Pacific Ocean on April 17, 2007 and the cloud mask from the operational MODIS cloud product, respectively. The middle and lower panels of Fig. 2.10 show the retrieved cloud properties for the pixels that have been identified as covered by ice clouds. Specifically, the middle panel on the left compares the retrieved ice cloud optical thickness from homogeneous and inhomogeneous ice crystals. For the latter, small air bubbles (r_1= r_2=0.45a, and r_3=0.2L) are embedded. The middle panel on the right is the same as the left panel except that the inhomogeneous ice crystals have larger air bubbles (r_1= r_2=0.85a, and r_3=0.2L). It is then evident that the cloud optical thicknesses are slightly reduced by using inhomogeneous ice crystal models in ice cloud property retrievals. These results are consistent with Fig. 2.9 where the inhomogeneous ice crystals reflect more than homogeneous ice crystals at λ = 0.65 μm. The increase in the sizes of air bubbles can further reduce the optical thickness as evident from the comparison of the two middle panels in Fig. 2.10. Using inhomogeneous ice crystals in ice cloud models may also significantly increase the retrieved ice cloud effective particle sizes, as evident from the lower panels in Fig. 2.10. Moreover, this effect becomes more significant as sizes of the air bubbles increase.

Figures 2.9 and 2.10 describe the sensitivities of ice cloud reflectance and cloud property retrievals to the optical properties of inhomogeneous ice crystals on the basis of the bi-spectral method developed by *Nakajima and King* [1990]. In this study, the same particle volumes and size distributions are employed for both homogeneous and

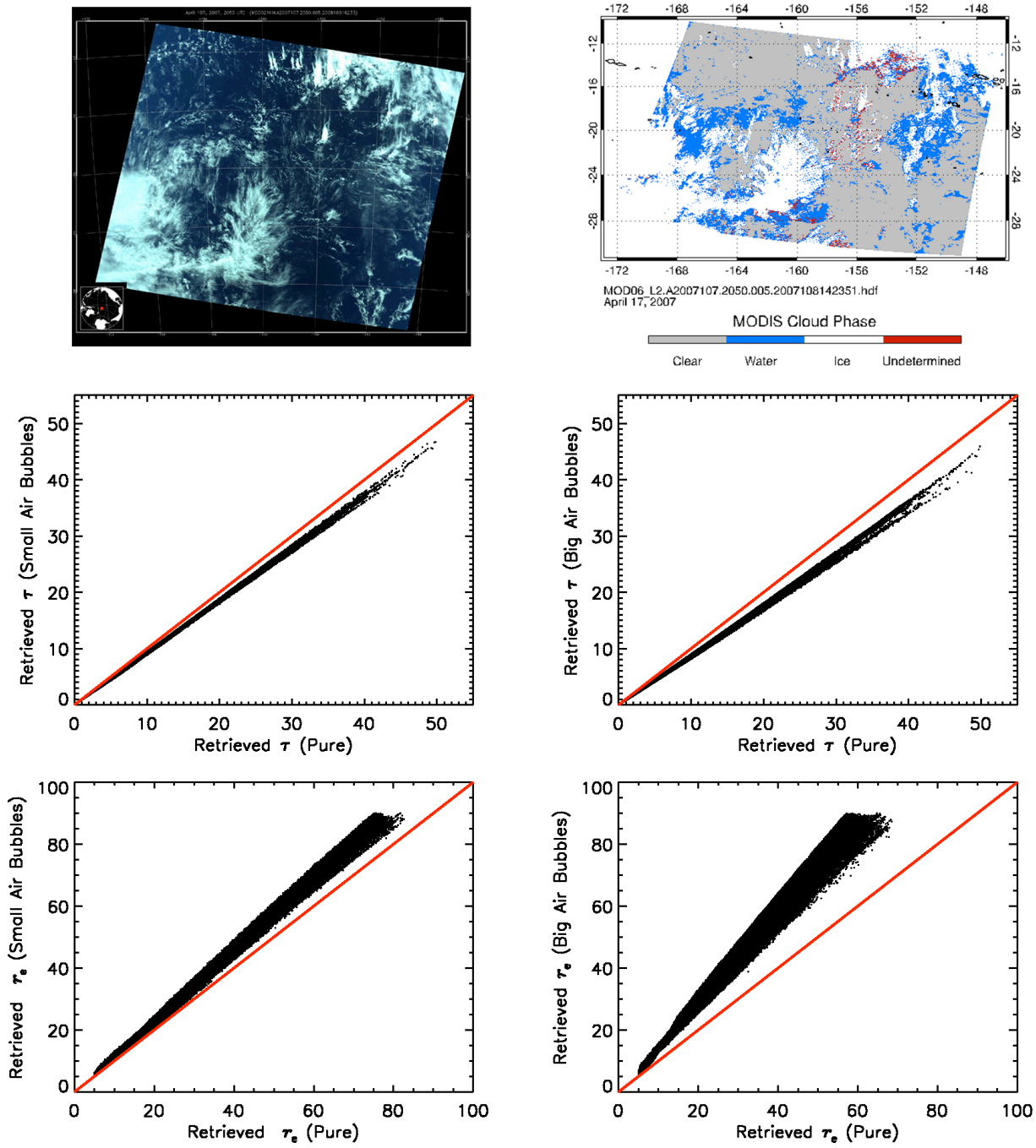

Fig. 2.10 MODIS granule image (RGB=band 4:3:1) from Terra on April 17, 2007, and MODIS cloud mask (upper panels). The comparisons of retrieved ice cloud optical thicknesses from homogeneous and inhomogeneous ice crystals (middle panels). The comparisons of retrieved ice cloud effective particle sizes from homogeneous and inhomogeneous ice crystals (lower panels).

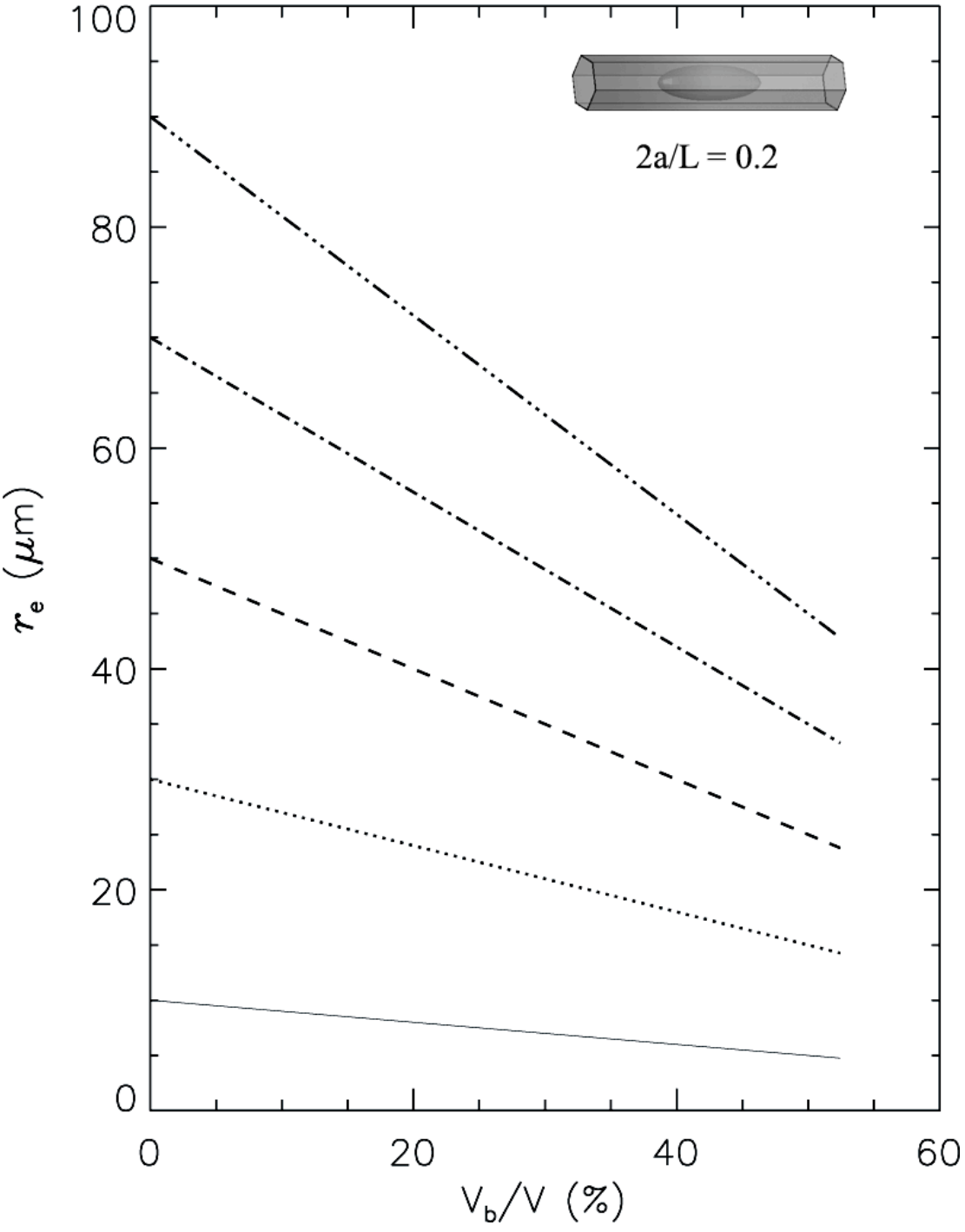

Fig. 2.11 Effective particle sizes for inhomogeneous ice crystals.

inhomogeneous ice crystals. However, air bubbles within ice crystals decrease the volume of ice and therefore decrease the effective particle size of ice crystals in the ice cloud. Figure 2.11 shows the variations of the effective particle size versus the volume of the air bubbles within an ice crystal. It is seen that the effective particle size of ice clouds can be reduced by more than 50%, depending on the shapes and sizes of the air bubbles within ice crystals. Thus, the increased effective particle size resulting from a retrieval employing inhomogeneous ice crystals in Fig. 2.10 can be partly compensated for if the volumes of the air bubbles are subtracted from the particle volumes.

2.5 Summary

This study reports on the single-scattering properties of inhomogeneous ice crystals whose geometries are defined on the basis of the observations made by *Tape* [1994] at the South Pole. Unlike the spherical air bubbles with random locations in the IHM model previously developed by *Labonnote et al.* [2001], in the present study, a few spherical or spheroidal air bubbles are defined within hexagonal ice crystals. The sensitivity of single-scattering properties to inhomogeneous ice crystals has been examined. It is found that the single-scattering phase function is substantially smoothed out and the 22° and 46° halos are reduced if air bubbles are included in the ice crystals. These features have been previously reported [*Labonnote et al.*, 2001; *Macke et al.*, 1996a; *Macke et al.*, 1996b]. The phase function smoothing can become more pronounced by increasing the number of air bubbles, enlarging the air bubble, changing the air bubbles' shapes from spheres to spheroids, or moving them from the sides to the center of an ice crystal. The peaks of the degree of linear polarization can also be reduced

by considering inhomogeneous ice crystals. Moreover, the asymmetry factors of inhomogeneous ice crystals may decrease to a minimum value and increase as the relative volume of the air bubbles increases.

Furthermore, a lookup library of bidirectional reflectances has been developed for both homogeneous and inhomogeneous ice cloud models at $\lambda = 0.65$ and 2.13 μm. We have shown that using inhomogeneous ice cloud models can increase the bidirectional reflectances at those two wavelengths. Therefore, the retrieved ice cloud optical thicknesses are slightly reduced whereas the retrieved ice cloud effective particle sizes can be significantly increased by including air bubbles in ice crystals, particularly, in the case of large air bubbles. This effect is similar to that found when surface roughness is included in the computations of ice crystal single-scattering properties [*Yang et al.*, 2008a; *Yang et al.*, 2008b], except that the presence of air bubbles in the crystals reduces the overall ice water content compared to a solid crystal with roughened surfaces. These results represent another important step in the effort to develop realistic ice crystal optical properties for use in retrieving ice cloud properties from satellite imagery and representing them in numerical weather and climate models. The results appear to be in the right direction for decreasing the biases in retrieved ice cloud optical properties, .e.g., *Min et al.* [2004]. Additional study will be needed, however, to determine if the optical properties of spheroidal bubbles, either alone or in combination with those for other ice crystal formulations, can provide a more accurate representation of actual ice crystal reflectance behavior.

CHAPTER III

USE OF SCATTERING PROPERTIES OF ICE PARTICLE AGGREGATES FOR THE REMOTE SENSING OF ICE CLOUDS*

3.1 Background

In recent years, significant research has been performed to improve the representation of the bulk scattering and absorption properties of ice clouds within the atmosphere. Ice cloud bulk-scattering models have been developed by *Baum et al.*[2005a; 2005b] for remote sensing applications from visible through infrared wavelengths, where the ice clouds were assumed to be composed of ice crystals with a set of idealized particle habits, i.e. bullet rosettes, hollow columns, droxtals, aggregates, and hexagonal columns and plates. The release of new microphysical ice cloud data from *in situ* measurements suggests that the representation of complex particles needs modification, such as in the bullet rosette and aggregate models. The conventional solid bullet rosettes have been modified to have a hollow structure at the end of the columnar part of each bullet branch [*Yang et al.*, 2008c]. In addition to homogeneous ice particles, ice crystals with hexagonal habits were observed to contain internal air bubbles with spherical or spheroidal geometries [*Tape*, 1994]. Furthermore, due to collisions with water droplets or other ice cloud particles during the formation of clouds, nonspherical ice crystals in ice

---

*Reprinted with permission from "Use of scattering properties of ice particle aggregates for the remote sensing of ice clouds", by Xie, Y., P. Yang, G. W. Kattawar, B. A. Baum, Y. X. Hu, *submitted to Appl. Opt.*

cloud models are regarded as more realistic when their surfaces are not assumed to be perfectly smooth. The scattering of radiation by nonspherical ice crystals with rough surface has been discussed by *Macke et al.*[1996b], *Yang and Liou* [1998], *Shcherbakov et al.*[2006] and *Yang et al.*[2008a; 2008b].

The representation of aggregated ice particles in cloud studies is an area needing further refinement and clarification. Aggregates are frequently found in regions of deep tropical convection [*Kajikawa and Heymsfield*, 1989; *Stith et al.*, 2002; *Stith et al.*, 2004] [*Baran et al.*, 2005; *Connolly et al.*, 2005; *Evans et al.*, 2005; *Gallagher et al.*, 2005; *Heymsfield*, 1986; *Houze and Churchill*, 1987; *McFarquhar and Heymsfield*, 1996; *Um and McFarquhar*, 2007; *Um and McFarquhar*, 2009] and are responsible for the generation and growth of precipitation particles usually existing with supercooled water droplets at temperatures warmer than -30°C [*Kajikawa and Heymsfield*, 1989]. When ice particles grow in supersaturated air, they may fall through the atmosphere at various speeds. Although the exact mechanism for aggregate formation is not well understood (e.g., [*Connolly et al.*, 2005]), ice particles can form aggregates from collisions resulting from the relative motion and aerodynamic interactions or from the presence of a strong electric field. Aggregation has been shown to be significantly influenced by the presence of strong electric fields that tend to exist in clouds with strong updrafts [*Dinh-Van and Phan-Cong*, 1978]. It has also been suggested that ice particles within tropical convective clouds are more likely to form aggregates in the presence of an electric field [*Connolly et al.*, 2005; *Pruppacher*, 1963; *Stith et al.*, 2002].

The coalescence rate is related to the habits of the individual ice particles and the ambient cloud temperature. Extensive laboratory studies (e.g., [*Hobbs et al.*, 1974]) have

demonstrated that hexagonal ice crystals with relatively warm (between -10 and -15°C) and rough surfaces may increase the aggregation rate. Furthermore, individual ice aggregates have often been found to be chains of plate shaped crystals [*Lawson et al.*, 2001; *Stith et al.*, 2002].

In this study, we define a new set of aggregate ice particles made from plates and investigate the scattering properties from visible to infrared wavelengths. A computationally efficient method is presented in Section 3.2 to generate numerical aggregate geometries that are similar to those obtained from *in situ* measurements. In section 3.3, we develop an aggregate model containing an ensemble of aggregate geometries and compute the resulting scattering properties. Section 3.4 is a discussion of the capability of the aggregate model to represent general aggregates within ice clouds. The influence of the aggregate particles on the remote sensing of ice cloud microphysical and optical properties is discussed in section 3.5, and conclusions are provided in section 3.6.

3.2 Numerical models for the aggregation of hexagonal ice crystals

The geometries of aggregate ice particles are available from *in situ* data collected during field campaigns [*Connolly et al.*, 2005; *Evans et al.*, 2005; *Gallagher et al.*, 2005; *Heymsfield*, 1986; *Kajikawa and Heymsfield*, 1989; *McFarquhar and Heymsfield*, 1996; *Stith et al.*, 2002; *Stith et al.*, 2004]. Based on observations and on the formation processes, aggregates most likely contain hexagonal monomers. Furthermore, the aggregates tend to contain significantly more hexagonal plates than columns, indicating the cloud temperatures corresponding to the formation of the ice particles. The hexagonal

ice monomers vary in the aspect ratio, and can be attached together in planar and in more complex three-dimensional forms. Thus, one specific aggregate model will be insufficient to realistically represent natural aggregates. However, as demonstrated by *Stith et al.*[2002], aggregates of plates usually exhibit chain-style shapes instead of more compact shapes.

In the present study, the geometries of aggregates are defined by attaching hexagonal plates together. The aspect ratios of the hexagonal plates, representing the relationship between the width and length of the particle, follow the *in situ* measurements reported by *Pruppacher and Klett* [1980]. For a hexagonal plate larger than 5 μm, the aspect ratio is determined by the relationship:

$$L = 2.4883a^{0.474}, \tag{3.1}$$

where a and L represent the semi-width and length of the ice crystal, respectively. Since aggregates consist of plates with similar particle sizes, a in Eq. (3.1) is given by

$$a = 20 + 20\xi_1, \tag{3.2}$$

and

$$a = 40 + 40\xi_2, \tag{3.3}$$

for generating relatively small and large aggregates, where ξ_1 and ξ_2 are independent random numbers distributed uniformly in [0, 1].

Following *Yang and Liou* [1998], we define aggregate ice crystals in a three-dimensional Cartesian coordinate system, $oxyz$, where the geometric coordinate of each hexagonal plate can be determined by the width, length, particle-center coordinates, and the Euler angles on the basis of a z-y-z convention. Figure 3.1a shows an example of a hexagonal particle that is specified in the $oxyz$ coordinate system (the laboratory system)

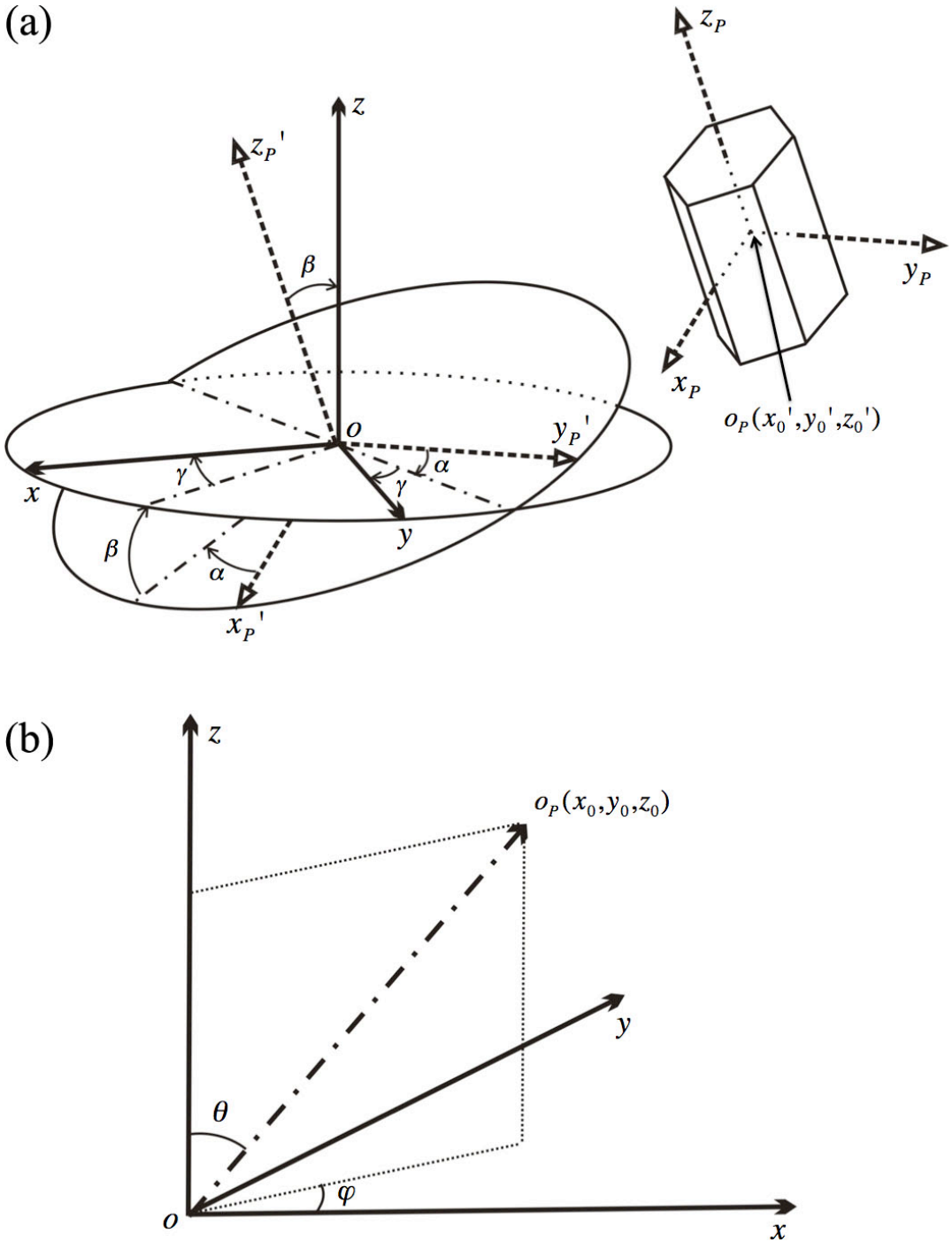

Fig. 3.1 (a) Transformation from the $o_P x_P y_P z_P$ to $oxyz$ coordinate system. (b) Polar and azimuthal angles in the $oxyz$ coordinate system.

and $o_P x_P y_P z_P$ (the particle system). The transfer from the particle system ($o_P x_P y_P z_P$) to the laboratory system ($oxyz$) through an intermediate coordinate system ($ox_P' y_P' z_P'$) is given by:

$$\begin{bmatrix} x_P' \\ y_P' \\ z_P' \end{bmatrix} = \begin{bmatrix} x_P \\ y_P \\ z_P \end{bmatrix} + \begin{bmatrix} x_0' \\ y_0' \\ z_0' \end{bmatrix}; \tag{3.4}$$

$$\begin{bmatrix} x \\ y \\ z \end{bmatrix} = R \begin{bmatrix} x_P' \\ y_P' \\ z_P' \end{bmatrix}; \tag{3.5}$$

where (x_0', y_0', z_0') are the coordinates of the origin of the $o_P x_P y_P z_P$ system in the $ox_P' y_P' z_P'$ coordinate system, and R is a rotational transformation matrix given by

$$R = \begin{bmatrix} \cos\gamma & -\sin\gamma & 0 \\ \sin\gamma & \cos\gamma & 0 \\ 0 & 0 & 1 \end{bmatrix} \cdot \begin{bmatrix} \cos\beta & 0 & \sin\beta \\ 0 & 1 & 0 \\ -\sin\beta & 0 & \cos\beta \end{bmatrix} \cdot \begin{bmatrix} \cos\alpha & -\sin\alpha & 0 \\ \sin\alpha & \cos\alpha & 0 \\ 0 & 0 & 1 \end{bmatrix}$$

$$= \begin{bmatrix} \cos\alpha\cos\beta\cos\gamma - \sin\alpha\sin\gamma & -\cos\beta\cos\gamma\sin\alpha - \cos\alpha\sin\gamma & \cos\gamma\sin\beta \\ \cos\gamma\sin\alpha + \cos\alpha\cos\beta\sin\gamma & \cos\alpha\cos\gamma - \cos\beta\sin\alpha\sin\gamma & \sin\beta\sin\gamma \\ -\cos\alpha\sin\beta & \sin\alpha\sin\beta & \cos\beta \end{bmatrix}, \tag{3.6}$$

where α, β, and γ, respectively, are the Euler angles that represent three consecutive rotations around the *z*, *y* and *z* axes. The positive values of the Euler angles indicate clockwise rotations in their rotating planes. To represent aggregates having random orientations, the Euler angles of the coordinate rotations are given by,

$$\alpha = \pi(2\xi_3 - 1), \tag{3.7}$$

$$\beta = \cos^{-1}(2\xi_4 - 1), \tag{3.8}$$

$$\gamma = \pi(2\xi_5 - 1), \tag{3.9}$$

where ξ_3, ξ_4, and ξ_5 are independent random numbers uniformly distributed in [0, 1]. As

shown in Fig. 3.1a, the valid range of α, β, and γ is $(-\pi, \pi]$. The particle centers of the hexagonal ice particles are determined in the *oxyz* coordinate system by

$$x_0 = d\xi_6 \sin\theta\cos\varphi, \tag{3.10}$$

$$y_0 = d\xi_6 \sin\theta\sin\varphi, \tag{3.11}$$

$$z_0 = d\xi_6 \cos\theta, \tag{3.12}$$

$$\theta = \cos^{-1}(2\xi_7 - 1), \tag{3.13}$$

$$\varphi = 2\pi\xi_8, \tag{3.14}$$

where d is initially set as a large value, e.g. 1000 μm; ξ_6, ξ_7, and ξ_8 are independent random numbers distributed uniformly in [0, 1]; and, θ and φ are the polar and azimuthal angles in the *oxyz* coordinate system (see Fig. 3.1b).

With the representations of an ice particle in the *oxyz* coordinate system, the distance between multiple ice particles can be computed by numerically considering the shortest distances among all the vertices and boundaries of the ice particles. The distance may be reduced with adjustments to the particle-center coordinates of an ice particle (specifically adjusting d in Eqs. (3.10)-(3.12)) while retaining all the other elements. Any two ice particles can join if they do not overlap and the distance between them is negligible. Appendix A provides a detailed procedure for estimating the relative position between two hexagonal particles, computing their distance and identifying whether or not they are overlapped. Repetition of the preceding process attaches more hexagonal plates to the particle. Due to the geometry of the particles, a new particle with determined a, L, α, β, and γ may not necessarily touch some existing aggregate elements. Therefore, the aggregation process begins again by testing the possibility that the aggregate elements can be attached with the new particle. To define chain-style aggregates, the test is

performed with the new attached aggregate elements while the parameters in Eqs. (3.7)-(3.9) are revised. For example, let

$$\beta_N = \begin{cases} \cos^{-1}(2\xi_9 - 1) & for \quad N = 1 \\ \beta_{N-1} + \cos^{-1}[2.0 \times (0.9^{90\xi_{10}} - 0.5)] & for \quad N > 1 \end{cases} \tag{3.15}$$

where N indicates the Nth hexagonal plate in the aggregation process.

Using the aforementioned procedure, we defined the numerous aggregates shown in Figs. 3.2 and 3.3. Figure 3.2 shows samples of "small" aggregates (hereafter referred to as Aggregates 1-5) consisting of 4 or 5 hexagonal plates. The dimensions of the aggregates in Fig. 3.2 can be scaled to fit the size parameters involved in the single-scattering computations. However, as suggested by recent *in situ* measurements, aggregates with extremely large particle sizes are achieved by increasing the monomer numbers instead of only scaling the sizes of each monomer. As shown in Fig. 3.3, "large" aggregates are represented by five models (hereafter referred to as Aggregates 6-10) each consisting of 8-12 hexagonal plates. In general, the ice cloud effective particle size for a given particle size distribution is defined by the maximum dimensions D_m, projected areas A and volumes V of the individual particles. Counting the largest distance between all the aggregate vertices determines the maximum dimensions of the aggregates shown in Figs. 3.2 and 3.3. An algorithm based on the Monte Carlo method computes the projected areas of the aggregates and the details are provided in Appendix B.

Figures 3.4a and 3.4b illustrate the ice crystal projected area and volume, respectively, for Aggregates 1-5 as functions of the particle maximum dimension. Among the five habits used to represent small aggregates, Aggregate 2 has a significantly larger projected area than the other habit realizations. Aggregate 5 has the smallest and largest

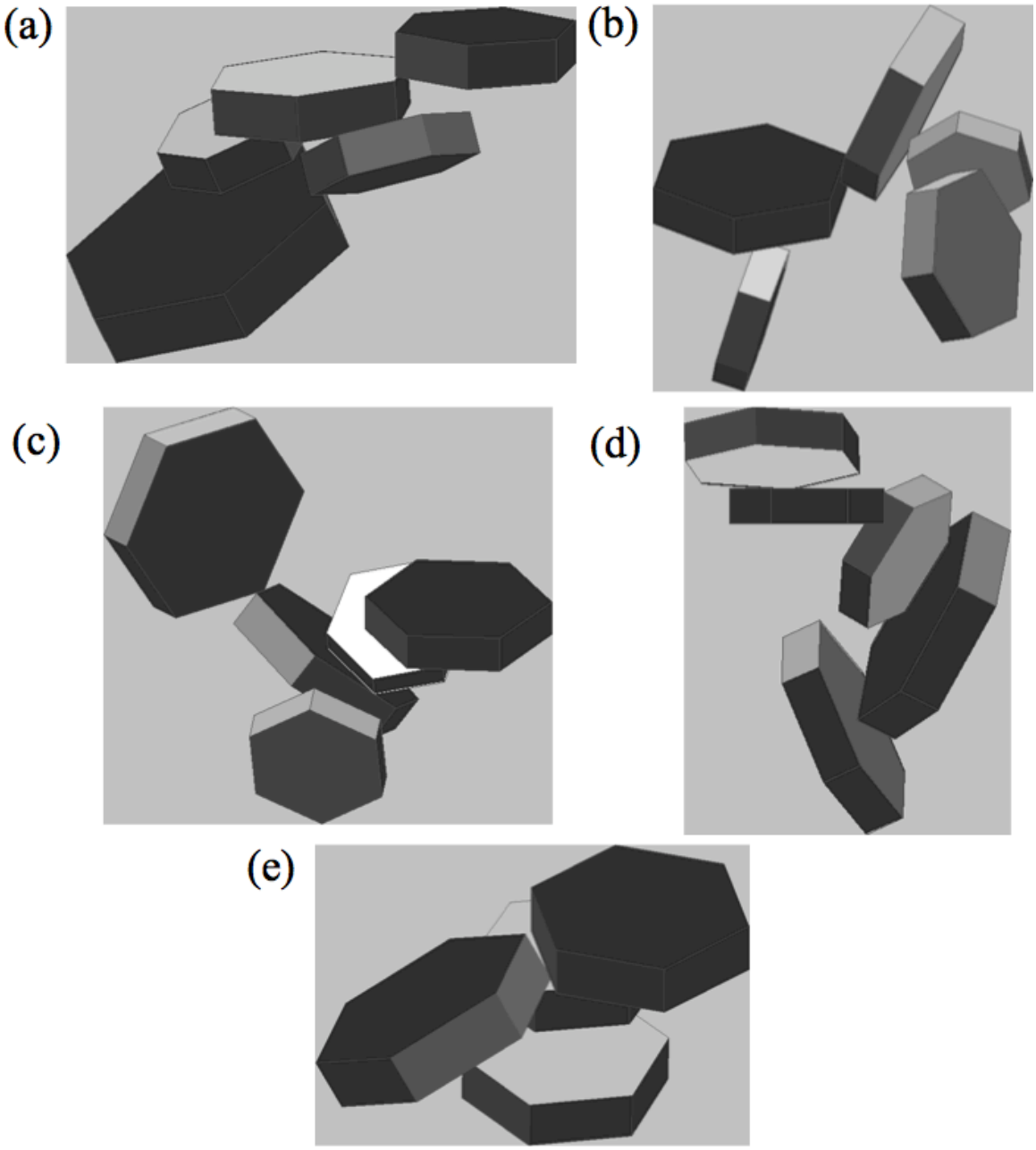

Fig. 3.2 Geometries of (a) Aggregate 1, (b) Aggregate 2, (c) Aggregate 3, (d) Aggregate 4, and (e) Aggregate 5.

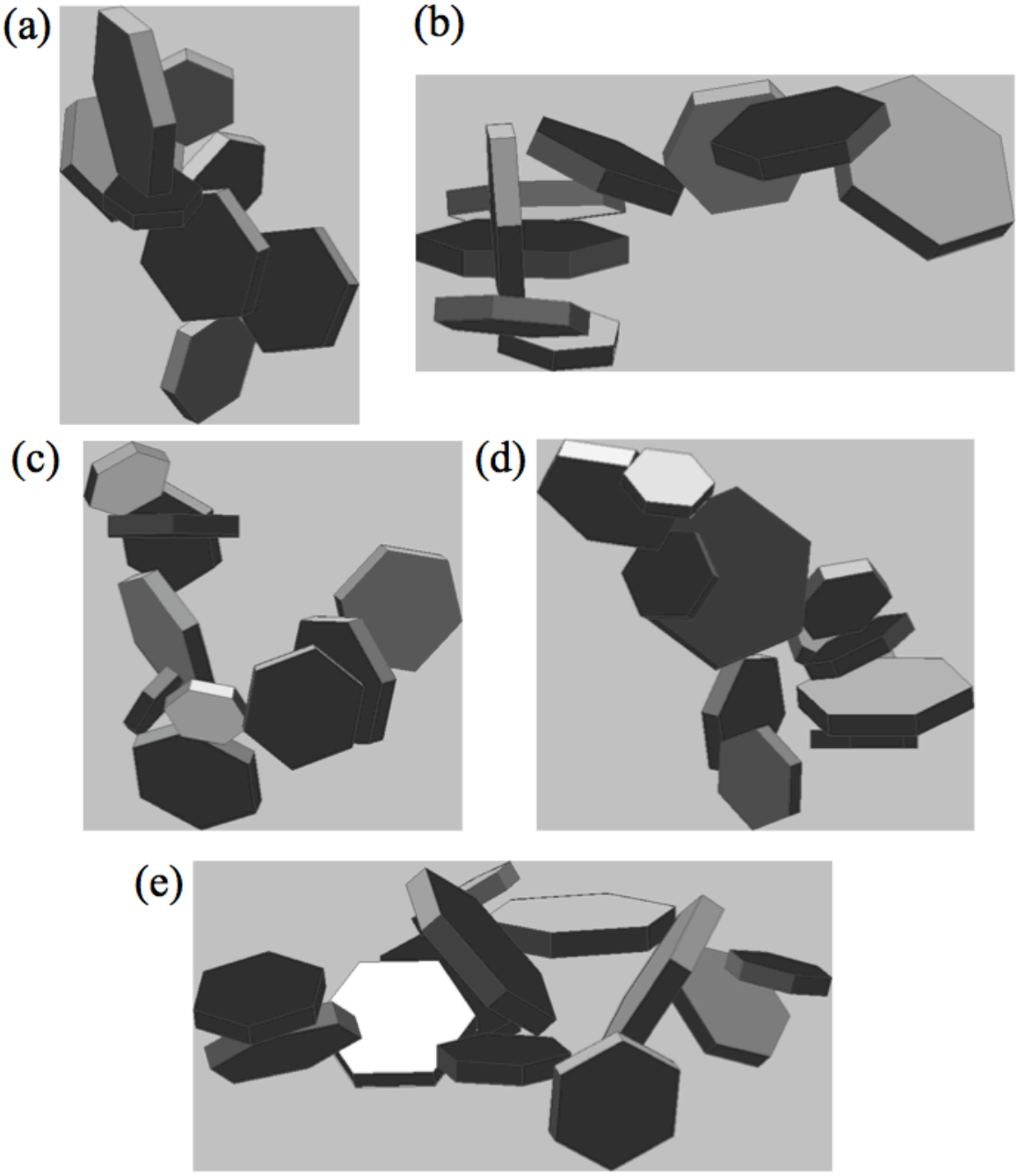

Fig. 3.3 Geometries of (a) Aggregate 6, (b) Aggregate 7, (c) Aggregate 8, (d) Aggregate 9, and (e) Aggregate 10.

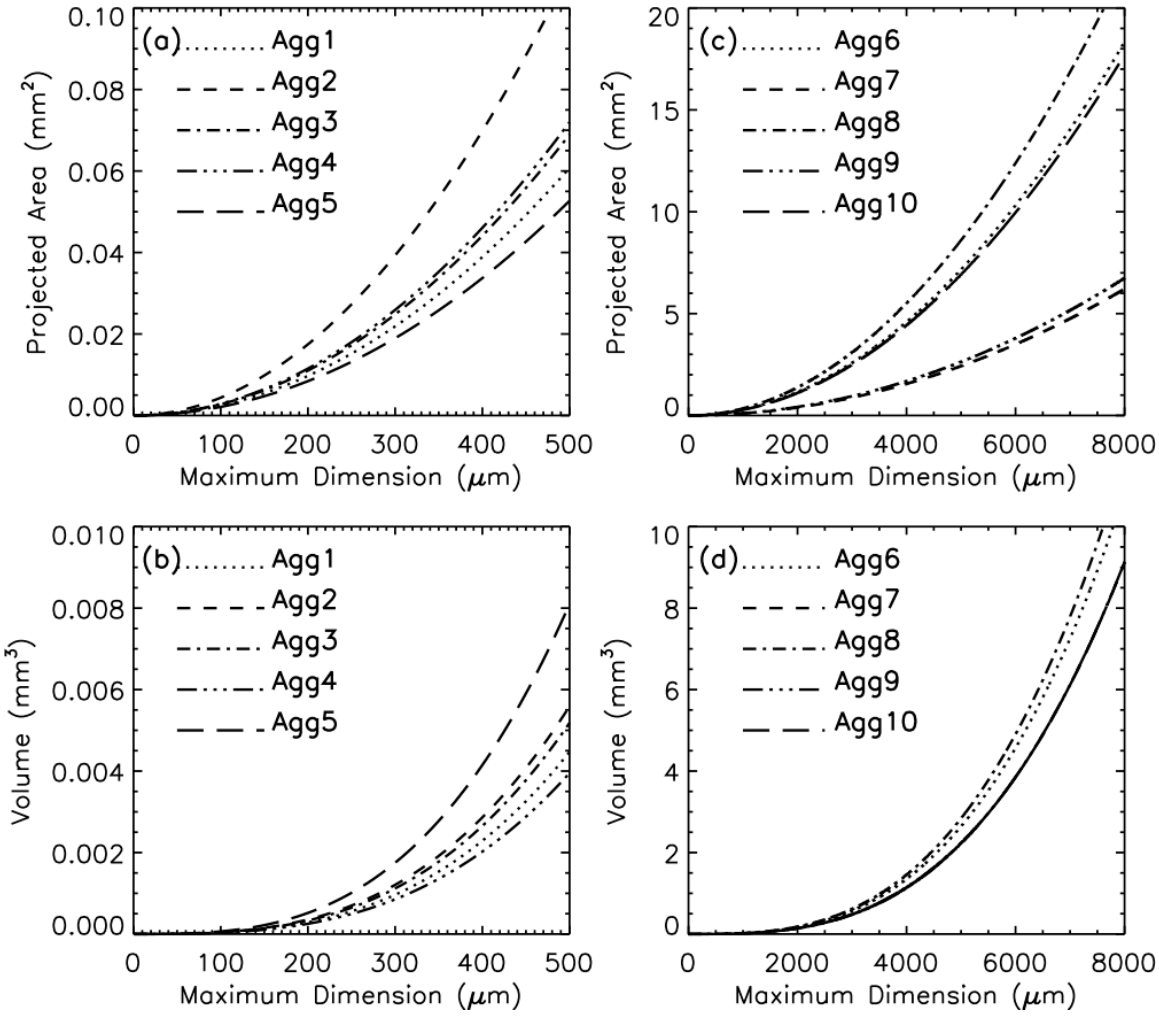

Fig. 3.4 (a) and (b): Variation of ice crystal projected area and volume versus maximum dimension for Aggregates 1-5. (c) and (d): Variation of ice crystal projected area and volume versus maximum dimension for Aggregates 6-10.

values of projected area and volume, which indicates a much more compact aggregate. Aggregate 4 exhibits a less compact particle compared to Aggregates 1, 3, and 5, and has a smaller volume and a larger projected area than the other habits. Figures 3.4c and 3.4d show the particle projected area and volume for Aggregates 6-10. For aggregates having the same particle sizes, Aggregates 7 and 9 have very similar volumes whereas their projected areas are much smaller than those of the other habits. However, the volume of Aggregate 10 is not distinct from Aggregates 7 and 9. The parameters associated with the aggregates in Figs. 3.3 and 3.4 can be found in Tables 3.1 and 3.2.

3.3 Scattering properties of aggregates

The scattering properties of the "small" and "large" aggregates are computed by a combination of the ADDA code [*Yurkin et al.*, 2007; *Yurkin and Hoekstra*, 2009] based on the discrete dipole approximation (DDA) method [*Draine*, 1988; *Draine and Goodman*, 1993; *Draine and Flatau*, 1994; *Purcell and Pennypacker*, 1973] and IGOM [*Yang and Liou*, 1996b]. The DDA is a technique to accurately simulate electromagnetic scattering by nonspherical particles over a wide frequency range. In the DDA method, the scattering particle is defined in terms of a number of electric dipoles. While the electric field within the computational domain is obtained from the incident electromagnetic wave and the interaction of the electric dipoles, the scattering and absorption properties of the scattering particle are derived via a near-to-far-field transformation. Because of its computational efficiency and convenience in the construction of irregular particle morphology, the DDA has been used to investigate light scattering by both oriented and

Table 3.1. The parameters associated with the 5 aggregates with small particle sizes.

Aggregate1: D_m=147.95, A = 5.32057E+03, V=1.15867E+05								
Element #	a	L	α(°)	β(°)	γ(°)	x_0	y_0	z_0
1	24.000	11.223	0.000	0.000	0.000	0.000	0.000	0.000
2	27.000	11.868	-82.655	175.767	-78.103	-5.664	43.934	-13.203
3	22.000	10.770	-7.651	-23.688	-132.443	-13.519	21.792	-25.347
4	20.000	10.294	-101.850	155.069	-50.709	18.656	68.178	-29.741
5	38.000	13.955	-118.412	-30.374	-42.438	-3.161	71.109	-54.738
Aggregate2: D_m=149.21, A = 9.71958E+03, V=1.48618E+05								
Element #	a	L	α(°)	β(°)	γ(°)	x_0	y_0	z0
1	35.000	13.421	0.000	0.000	0.000	0.000	0.000	0.000
2	35.000	13.421	-136.864	111.886	20.422	37.806	35.423	31.105
3	22.000	10.770	129.602	-103.763	123.851	54.186	51.254	4.438
4	26.000	11.657	-106.007	74.775	-150.946	19.071	-23.051	-32.585
5	30.000	12.476	102.088	-111.157	13.492	70.653	26.702	-12.658
Aggregate3: D_m=162.32, A = 7.26631E+03, V=1.77345E+05								
Element #	a	L	α(°)	β(°)	γ(°)	x_0	y_0	z_0
1	33.000	13.052	0.000	0.000	0.000	0.000	0.000	0.000
2	25.000	11.443	-104.323	147.168	29.018	7.916	31.004	-17.561
3	37.000	13.779	-66.295	-39.138	139.772	4.977	59.195	-37.719
4	26.000	11.657	-117.000	101.552	-154.612	-26.415	41.781	-56.674
5	38.000	13.955	-89.474	-95.683	-111.998	-12.506	99.011	17.501
Aggregate4: D_m=174.08, A = 8.72443E+03, V=1.66768E+05								
Element #	a	L	α(°)	β(°)	γ(°)	x_0	y_0	z_0
1	25.000	11.443	0.000	0.000	0.000	0.000	0.000	0.000
2	26.000	11.657	-136.348	117.880	-25.069	29.954	28.576	-14.725
3	39.000	14.128	-74.542	-63.550	12.115	43.180	44.478	-38.725
4	35.000	13.421	-178.069	113.773	164.661	14.393	57.944	-71.778
5	30.000	12.476	-46.679	165.030	-89.502	-11.329	-2.432	18.621
Aggregate5: D_m=101.73, A = 2.18089E+03, V=6.82456E+04								
Element #	a	L	α(°)	β(°)	γ(°)	x_0	y_0	z_0
1	25.000	11.443	0.000	0.000	0.000	0.000	0.000	0.000
2	27.000	11.868	-22.406	30.910	117.028	-44.627	18.399	-13.063
3	21.000	10.535	-100.936	-179.061	44.979	-2.087	20.477	-18.406
4	23.000	10.999	-135.880	177.983	71.613	-19.081	3.495	-29.831

Table 3.2. The parameters associated with the 5 aggregates with large particle sizes.

Aggregate6: D_m=369.63, A = 3.91496E+04, V=1.06798E+06								
Element #	a	L	α(°)	β(°)	γ(°)	x_0	y_0	z_0
1	40.000	14.298	0.000	0.000	0.000	0.000	0.000	0.000
2	79.000	19.741	-46.217	88.822	11.433	-12.564	13.110	84.021
3	43.000	14.797	-179.796	-93.563	85.646	32.092	34.451	70.872
4	59.000	17.190	-7.572	77.85	-132.999	42.693	0.1521	-57.088
5	49.000	15.742	-25.814	88.721	-49.824	44.632	-4.197	-156.989
6	58.000	17.052	-133.723	-138.154	-47.923	-14.287	75.580	-5.949
7	55.000	16.628	170.641	-62.393	51.869	116.120	16.863	-106.819
8	46.000	15.277	-59.226	86.727	125.394	67.638	95.060	-50.351
Aggregate7: D_m=473.71, A = 2.17697E+04, V=1.89471E+06								
Element #	a	L	α(°)	β(°)	γ(°)	x_0	y_0	z_0
1	78.000	19.623	0.000	0.000	0.000	0.000	0.000	0.000
2	68.000	18.387	82.921	164.510	102.946	-6.719	-54.101	25.823
3	67.000	18.258	-92.660	-22.959	1.713	-60.934	-25.493	57.639
4	69.000	18.515	28.655	86.571	-174.082	5.337	114.889	47.891
5	57.000	16.912	160.118	-114.845	-79.650	-158.696	-28.416	72.697
6	59.000	17.190	-61.486	16.746	-99.622	0.291	122.872	-29.215
7	49.000	15.742	-152.577	167.203	-63.528	-29.232	41.204	-58.603
8	66.000	18.129	-40.620	-16.260	-133.618	-207.718	47.738	96.347
9	79.000	19.741	141.896	133.140	-46.151	-291.690	-26.998	58.650
Aggregate8: D_m=439.51, A = 6.64570E+04, V=1.92774E+06								
Element #	a	L	α(°)	β(°)	γ(°)	x_0	y_0	z_0
1	77.00	19.503	0.000	0.000	0.000	0.000	0.000	0.000
2	58.000	17.052	-177.368	64.830	-27.941	99.193	4.561	-7.375
3	75.000	19.261	-146.815	-117.312	-69.303	115.667	8.322	-105.096
4	42.000	14.633	99.056	53.002	77.723	90.671	21.580	-175.875
5	47.000	15.434	13.853	-135.455	33.875	-18.069	47.826	47.262
6	72.000	18.892	-167.855	43.472	-23.762	97.754	-22.864	-249.469
7	45.000	15.119	-108.623	-142.431	-15.595	7.019	-35.116	-189.123
8	65.000	17.998	-51.308	-72.400	-173.509	-14.105	-132.186	-184.875
9	74.000	19.139	-87.353	75.060	-49.382	32.361	-171.149	-155.846
10	70.000	18.641	-98.065	-111.24	25.565	50.082	-228.132	-81.978
Aggregate9: D_m=445.23, A = 2.08749E+04, V=1.57522E+06								
Element #	a	L	α(°)	β(°)	γ(°)	x_0	y_0	z_0
1	48.000	15.589	0.000	0.000	0.000	0.000	0.000	0.000
2	77.000	19.503	150.470	158.669	64.315	16.422	-9.303	36.460
3	50.000	15.893	156.544	-28.559	7.439	-0.981	12.898	79.428
4	51.000	16.043	133.796	143.141	106.479	8.530	110.051	82.220
5	45.000	15.119	15.886	-42.947	-76.896	-21.106	1.340	120.318
6	79.000	19.741	7.484	100.825	85.510	-126.526	-12.425	138.208
7	43.000	14.797	148.401	-80.442	51.002	-183.477	-38.868	140.806
8	57.000	16.912	29.050	79.070	134.321	-103.686	15.369	22.394
9	46.000	15.277	164.668	-104.400	31.959	-103.477	-37.950	-32.759
10	67.000	18.258	102.284	-39.670	-137.843	-241.91	-59.434	209.639
11	40.000	14.298	-20.386	138.140	88.125	-216.237	-146.224	219.446
Aggregate10: D_m=471.42, A = 6.14953E+04, V=1.86694E+06								
Element #	a	L	α(°)	β(°)	γ(°)	x_0	y_0	z_0
1	51.000	16.043	0.000	0.000	0.000	0.000	0.000	0.000
2	53.000	16.338	121.826	79.245	59.939	44.024	-70.931	-27.186
3	75.000	19.261	-119.265	-122.802	131.734	117.027	-44.620	44.158
4	74.000	19.139	168.954	-47.041	130.687	28.929	51.624	67.320
5	49.000	15.742	175.836	130.105	92.497	152.171	-84.018	27.426
6	73.000	19.016	44.989	177.401	-107.193	155.161	74.466	61.031
7	40.000	14.298	85.171	-13.969	154.203	175.293	-111.757	53.939
8	61.000	17.464	128.262	45.585	-151.717	85.657	138.845	10.530
9	59.000	17.190	86.249	-140.248	-143.415	30.315	139.789	-3.023
10	59.000	17.190	17.525	33.540	73.917	-67.218	161.784	-3.566
11	43.000	14.797	-94.888	-148.820	117.310	108.901	146.382	77.028
12	52.000	16.192	72.882	-18.720	22.437	-105.644	147.902	39.572

arbitrary distributed particles including ice particles and aerosols in the atmosphere [*Bi et al.*, 2009b; *Evans et al.*, 2005; *Hong et al.*, 2009; *Kalashnikova and Sokolik*, 2004; *Nousiainen and Muinonen*, 2007; *Nousiainen et al.*, 2009].

The extinction efficiencies, asymmetry factors and scattering phase functions derived by the ADDA have been compared with those from Mie theory [*Yurkin et al.*, 2007]. The RMS relative errors from the ADDA are quite small for cases when $m_r<1.4$, where m_r is the real part of the refractive index. However, the ADDA requires sufficient electric dipoles in the computational domain to resolve detailed geometric features of the scattering particle and to achieve numerical accuracy. As a result, chained-particle aggregates tend to consume a substantial amount of computing time because of the multiple electric dipoles in a relatively large computational domain. In our study, ADDA v0.79 [*Yurkin et al.*, 2007] is used to compute the scattering properties of aggregates. The size of the electric dipoles in the ADDA is given as follows:

$$d=\begin{cases}\left\langle \dfrac{D_m}{20},\ \dfrac{\lambda}{20|m|}\right\rangle & for\quad X\le 1\\ \dfrac{\lambda}{20|m|} & for\quad 1<X<5\\ \dfrac{\lambda}{10|m|} & for\quad 5<X<15\\ \dfrac{\lambda}{5|m|} & for\quad X>15\end{cases} \tag{3.16}$$

where d is the size of each electric dipole, m is refractive index of the aggregates, λ is the wavelength, and $\langle\ \rangle$ indicates the minimum value of the variables. The size parameter, X, of an aggregate is defined by

$$X=\frac{\pi D_s}{\lambda}, \tag{3.17}$$

The conventional IGOM has been extensively employed in the light scattering and radiative transfer processes for satellite-based remote sensing of ice clouds [*Baum et al.*, 2005a; *Baum et al.*, 2005b; *Wendisch et al.*, 2005; *Yang et al.*, 2005]. For computations involving large size parameters, the IGOM is an efficient method to compute the scattering properties of aggregates, and our version has been updated in numerous ways over the past few years. Compared to the computations reported by *Yang and Liou* [1998], the current IGOM has improved the treatment of the edge effect [*Mitchell et al.*, 2001; *Nussenzveig and Wiscombe*, 1980; *Nussenzveig and Wiscombe*, 1991] and enhanced the treatment of forward scattering [*Bi et al.*, 2009a]. To more accurately account for the divergence of scattered energy in the forward peak, making the delta-transmission term is no longer necessary even for extremely large particles. As a result of the scattering model improvements, the extinction efficiency of an ice particle exhibits a smooth transition from small to large particles whose scattering properties are computed from the ADDA and IGOM, respectively. Additionally, the IGOM code used in *Yang and Liou* [1998] has been revised to adapt to various sets of parameters associated with aggregates.

Figure 3.5 shows the extinction efficiency, absorption efficiency, single scattering albedo, and asymmetry factor as functions of size parameter for Aggregate 1 at λ=2.13 μm. The extinction and absorption efficiencies from the ADDA were originally derived by dividing the corresponding extinction and absorption cross sections of the scattered particle over the cross section of a volume-equivalent sphere. For consistency with the IGOM, the cross section of the volume-equivalent sphere is replaced by a projected area computed by the process described in Appendix B. In the IGOM computations, the

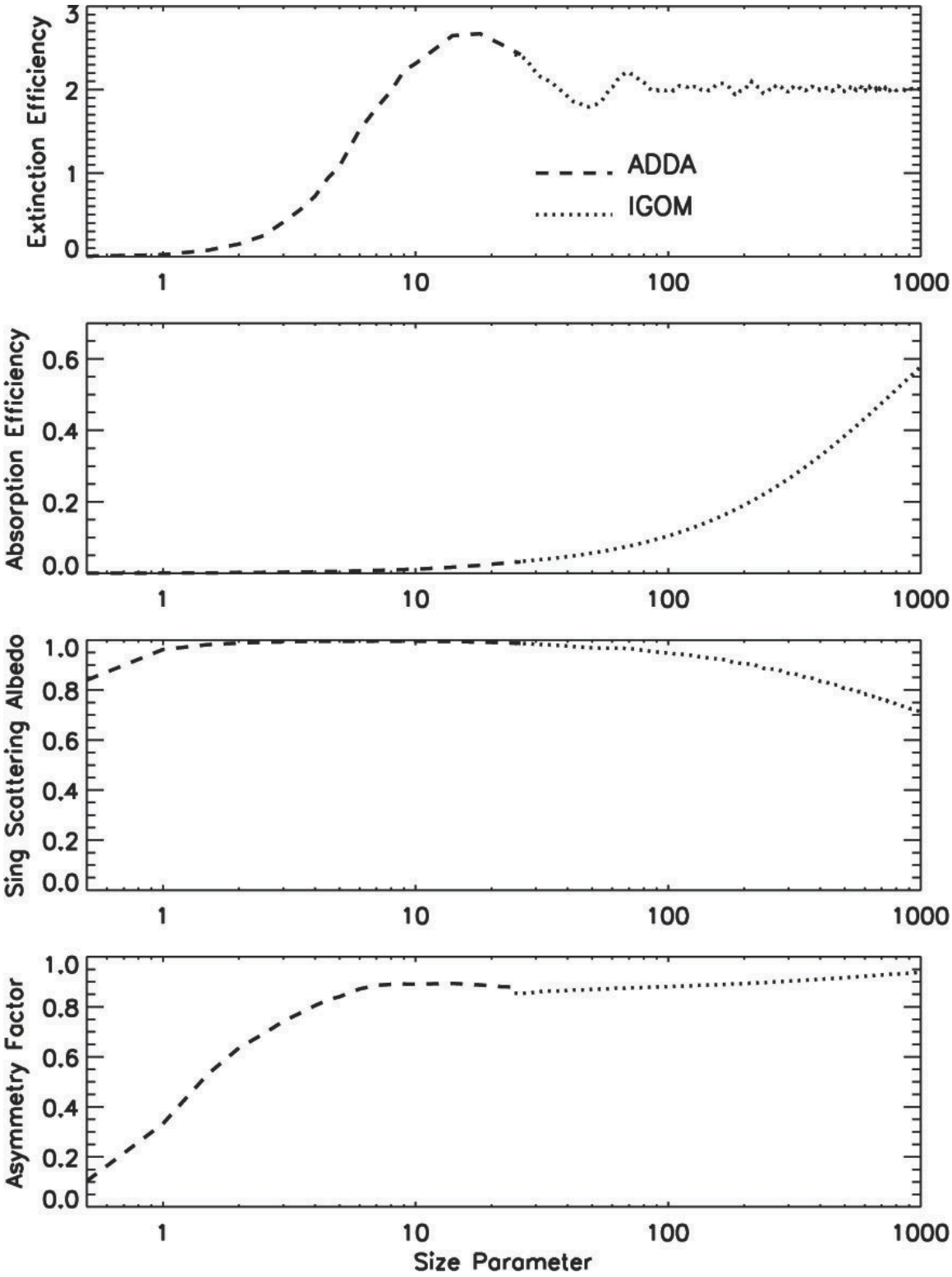

Fig. 3.5 Extinction efficiency, absorption efficiency, single scattering albedo, and asymmetry factor as functions of size parameter for Aggregate 1 at λ=2.13 μm.

above-edge effect contribution to the extinction and absorption efficiencies can be approximated following *Bi et al.* [2009b] as follows:

$$Q_{e,edge}(\lambda) = 2c_1\left(\frac{\lambda}{\pi D_m}\right)^{2/3}, \tag{3.18}$$

$$Q_{a,edge}(\lambda) = 2c_2\left(\frac{\lambda}{\pi D_m}\right)^{2/3}. \tag{3.19}$$

The two constants, c_1 and c_2, are determined at the wavelength (λ_t) where the use of the ADDA is switched to the use of IGOM in the form of:

$$c_1 = 0.5\left[Q_{e,ADDA}(\lambda_t) - Q_{e,IGOM}(\lambda_t)\right]\left(\frac{\pi D_m}{\lambda_t}\right)^{2/3}, \tag{3.20}$$

$$c_2 = 0.5\left[Q_{a,ADDA}(\lambda_t) - Q_{a,IGOM}(\lambda_t)\right]\left(\frac{\pi D_m}{\lambda_t}\right)^{2/3}, \tag{3.21}$$

where $Q_{e,ADDA}(\lambda_t)$ and $Q_{a,ADDA}(\lambda_t)$ are the extinction and absorption efficiencies computed by the ADDA, and $Q_{e,IGOM}(\lambda_t)$ and $Q_{a,IGOM}(\lambda_t)$ are those computed from the IGOM without accounting for the above-edge effect. From Fig. 3.5, it can be seen that the extinction efficiency for the aggregate initially rises rapidly with particle size, and subsequently approaches a constant value of 2 with a decaying oscillation. As the size parameter increases from 40 to 1000, the absorption efficiency increases dramatically due to the increase of the ray path length within the particle as the single scattering albedo decreases from 1. The asymmetry factor in Fig. 3.5 generally increases with particle size when diffraction becomes significant compared to the scattering of light by the particle. For wavelengths with strong absorption, the scattering properties increase with particle size as shown in Fig. 3.6. The results in Figs. 3.5 and 3.6 reflect smooth transitions of the scattering properties from small to large particles. The computations by the ADDA and

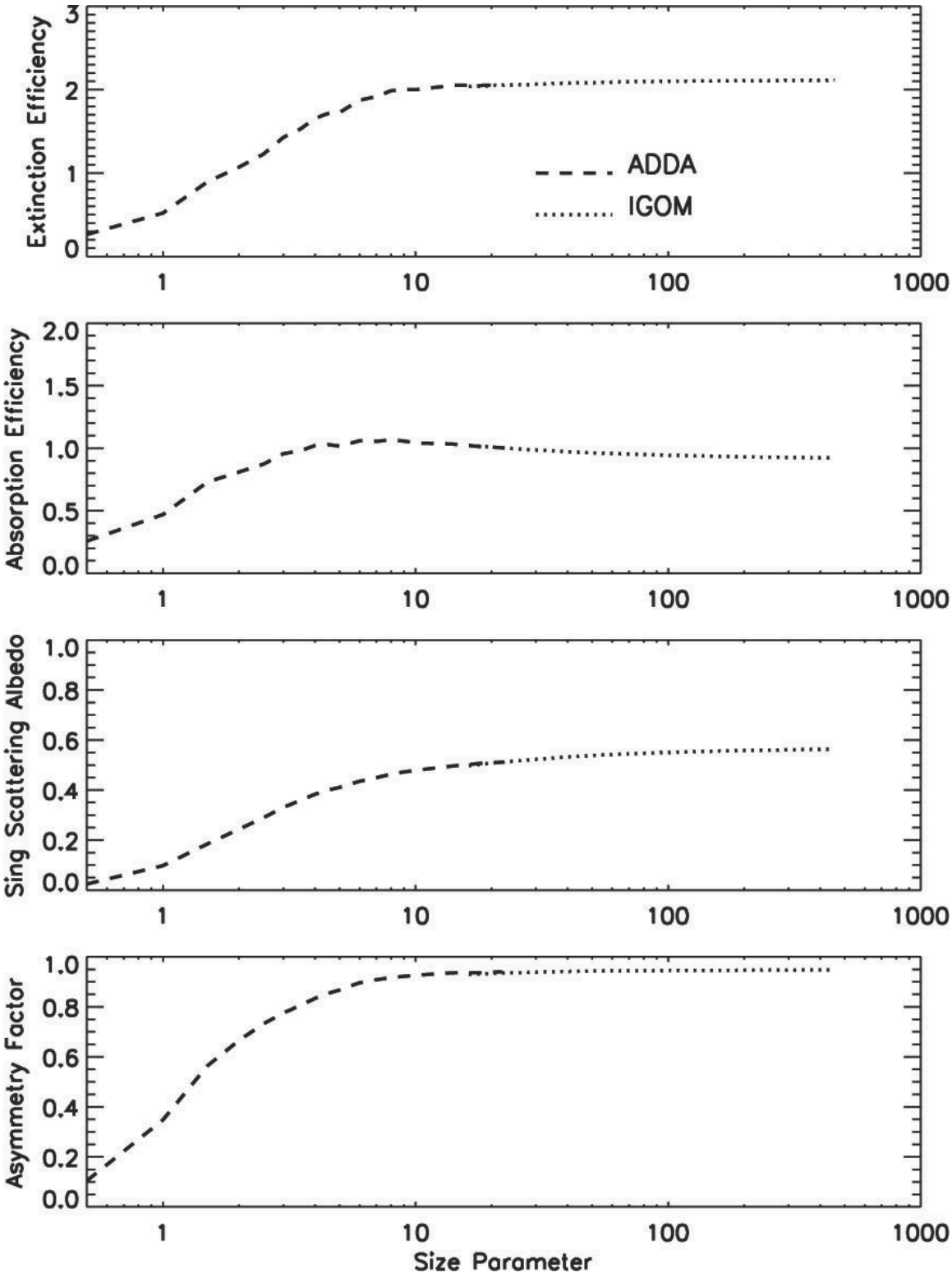

Fig. 3.6 Same as Fig. 3.5, except that λ=12.0 μm.

IGOM are very consistent in the region where the size parameter is approximately 25, with the consistency possible due to improvements in the IGOM. The scattering properties of the aggregates in our study are computed by the ADDA when the size parameter is smaller than 25, and by the IGOM for aggregates with larger size parameters.

Figure 3.7 shows the scattering phase matrixes for Aggregate 1 with a maximum dimension of 100 μm. Following *Yang and Liou* [1998], the surface roughness of the aggregates is specified by small tilted facets on the particle surface. The slopes of the roughened facets are randomly sampled assuming a Gaussian distribution [*Cox and Munk*, 1954]. The RMS tilt σ can be used as the parameter to specify the degree of surface roughness. As σ increases from 0 to 1, the surface roughness varies from smooth to deeply roughened. From Fig. 3.7, aggregates are seen to be associated with strong forward scattering at visible wavelengths due to diffraction. In addition, the phase function for a smooth aggregate reveals halo peaks at approximately 22° and 46°. However, the halos become less significant as σ increases because of the spreading of the rays that are associated with minimum deviation of refraction. Figure 3.8 shows the scattering phase matrix for Aggregate 10 with a maximum dimension of 1000 μm. The scattering phase function (P_{11}) for Aggregate 10 has lower values at some side scattering angles compared to Aggregate 1 for smooth particles, but these differences decrease as σ increases. It is interesting to note that an increasing σ tends to increase the side scattering over that of smooth particles. Additionally, the other non-zero elements of the phase matrices in Figs. 3.7 and 3.8 are sensitive to ice particle habit, size and surface roughness, which indicate the potential of using polarization measurements to determine ice cloud

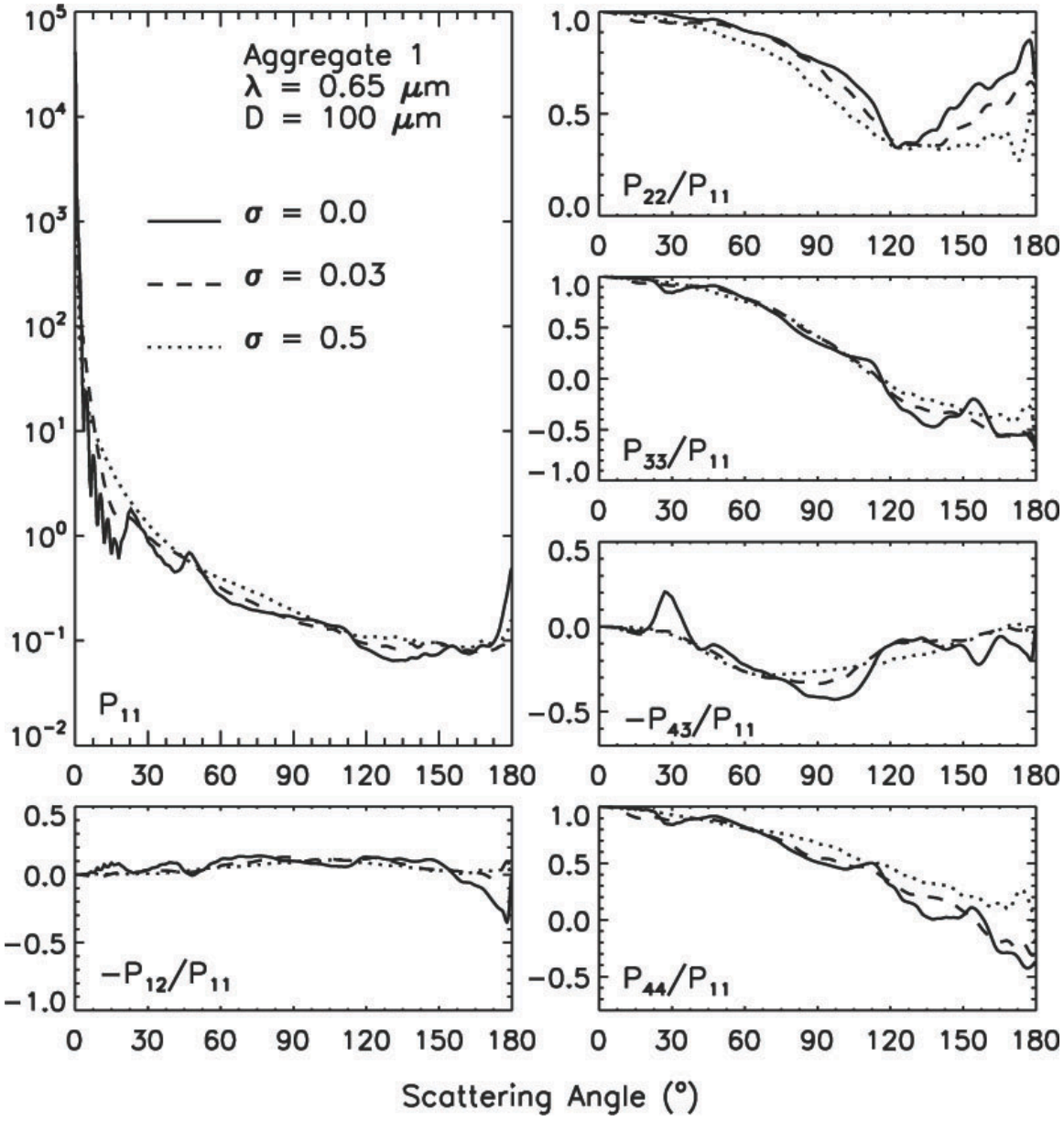

Fig. 3.7 Scattering phase matrixes for Aggregate 1 at λ=0.65 μm.

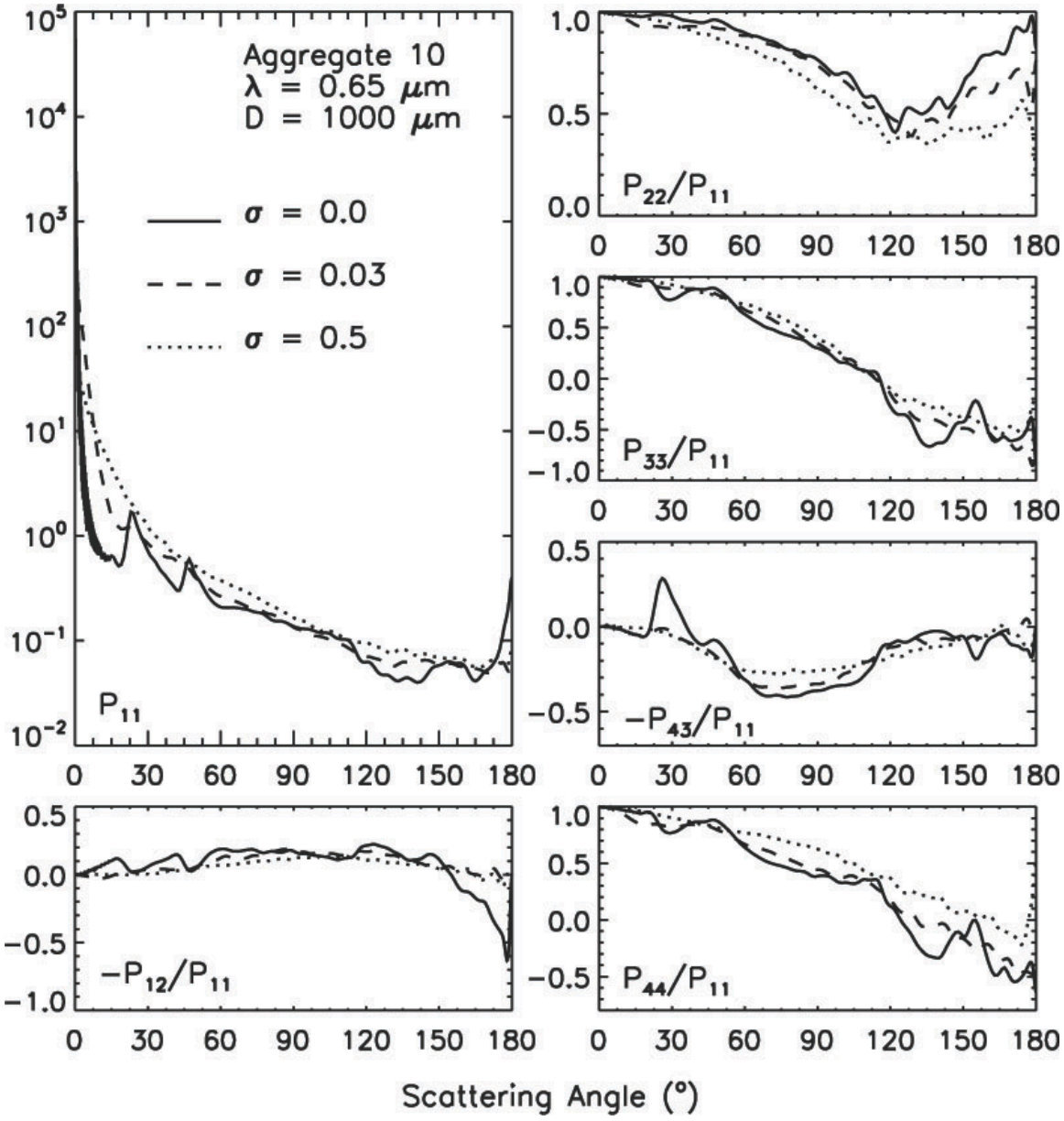

Fig. 3.8 Scattering phase matrixes for Aggregate 10 at λ=0.65 μm.

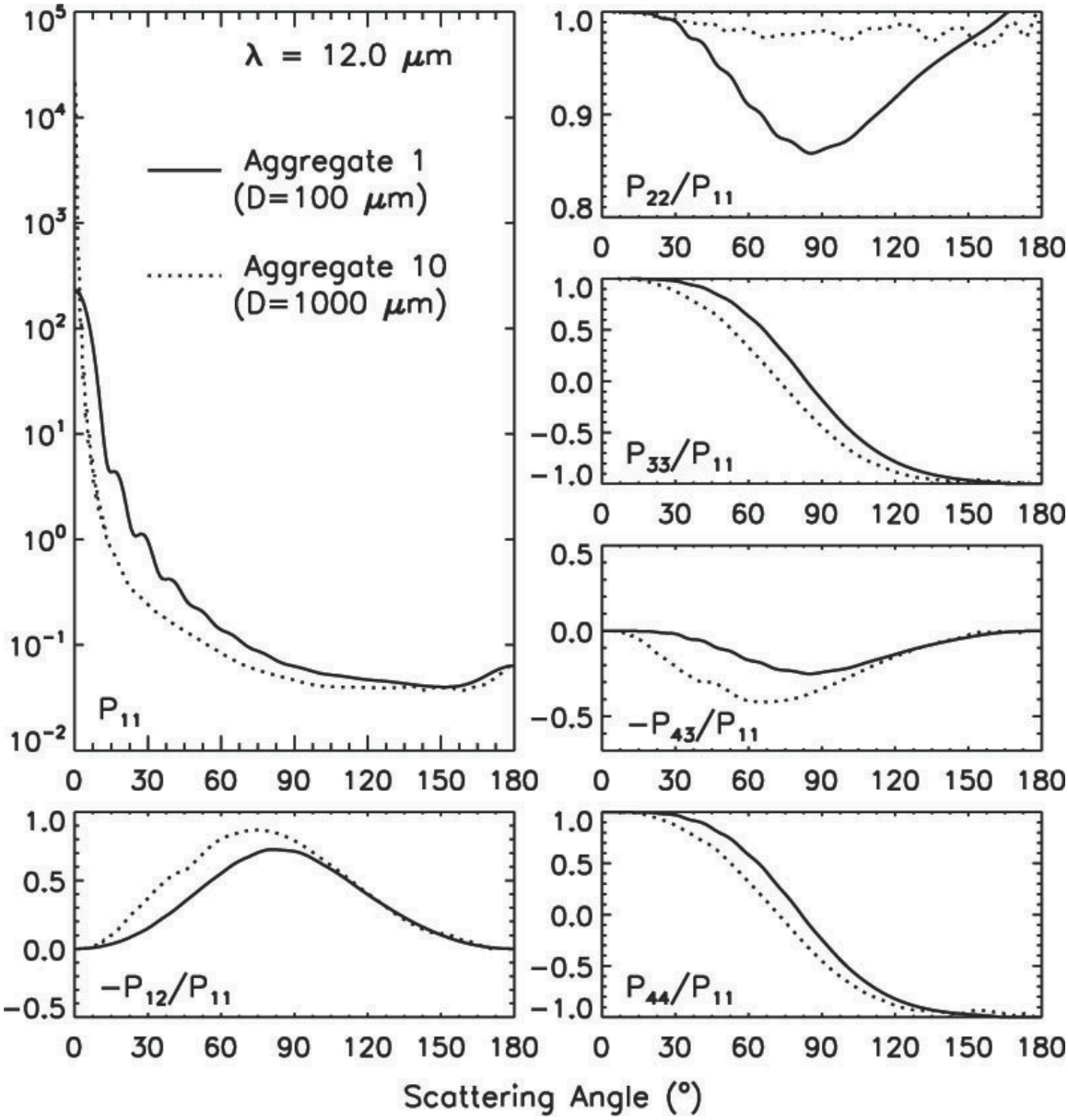

Fig. 3.9 Scattering phase matrixes for Aggregates 1 and 10 at λ=12.0 μm.

microphysical properties. Figure 3.9 compares the scattering phase matrixes for Aggregates 1 and 10 at λ=12.0 μm, and it can be seen that that the various elements of the phase matrix tend to be nearly featureless (i.e., no halos) because of strong absorption.

3.4 Validation of the aggregate model

Various aggregate models consisting of one or a small number of predetermined geometrical particles have been used in previous studies [*Baran and Labonnote*, 2006; *Evans et al.*, 2005; *Um and McFarquhar*, 2009; *Yang and Liou*, 1998]. Our aggregate model uses 10 aggregate geometries with various particle sizes to represent the aggregates. The averaged scattering properties of the aggregates can be used to establish the validity of our aggregate model.

Figure 3.10 shows the comparison of the scattering phase functions for the 'real aggregates' within ice clouds and the approximation using our aggregate models in Figs. 3.2 and 3.3. To represent the variety of aggregates in ice clouds, the 'real aggregates' are an average of 1000 aggregates composed of four or five hexagonal plates having aspect ratios as described by Eq. (3.1). Similar to the aggregate model involving Aggregates 6-10, large aggregates in the 'real aggregates' consist of eight to twelve plates, except that 1000 geometries are considered. The equivalent phase functions in Fig. 3.10 are given by

$$\overline{P_{11}(\Theta,D_m,\lambda)} = \frac{\sum_{n=1}^{M} P_{11}(\Theta,D_m,\lambda,n)C_s(D_m,\lambda,n)}{\sum_{n=1}^{M} C_s(D_m,\lambda,n)}, \tag{3.22}$$

where $P_{11}(\Theta,D_m,\lambda,n)$ is the phase function for each aggregate geometry, Θ is scattering

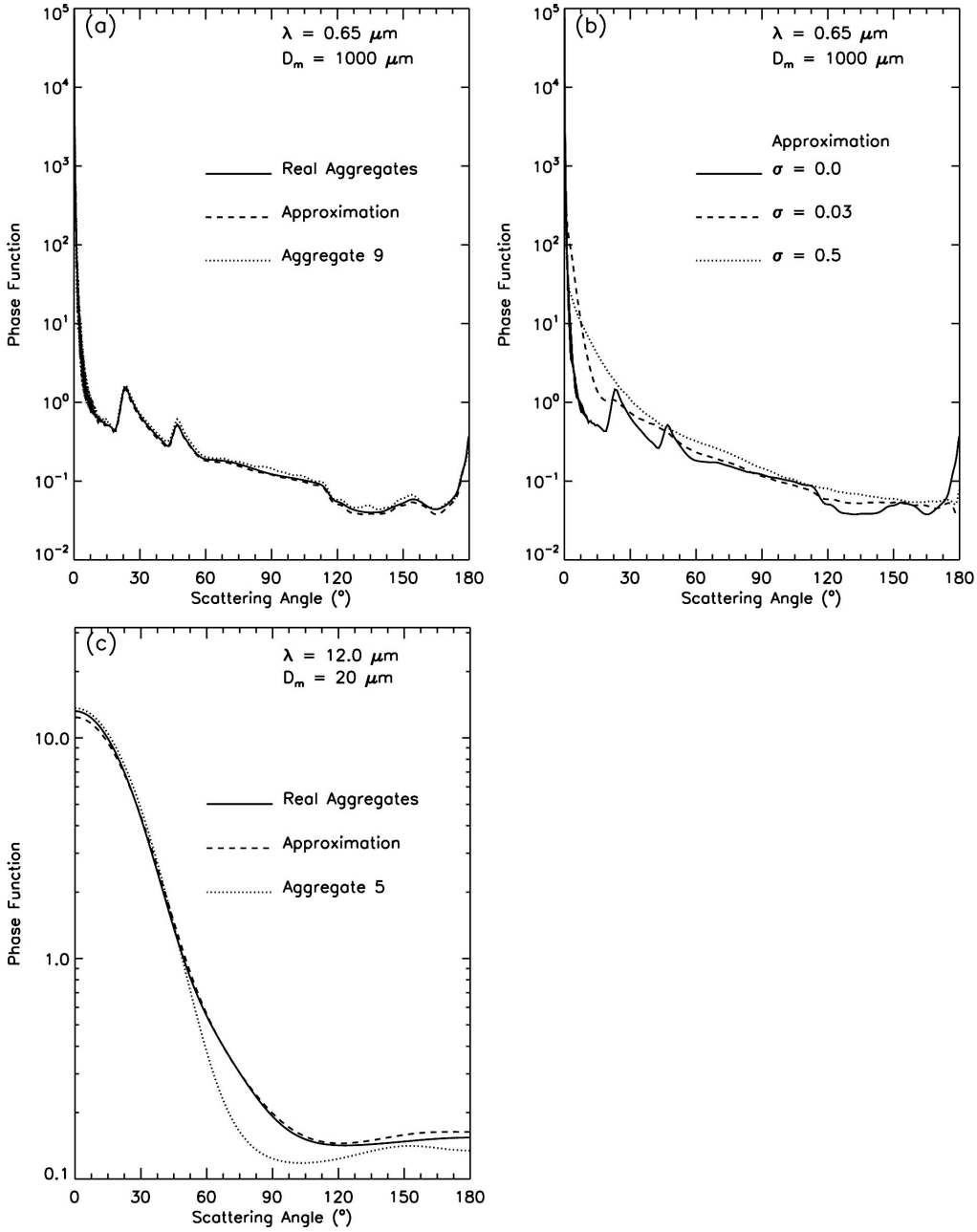

Fig. 3.10 (a) Comparison of the scattering phase functions for the averaged values over 1000 aggregates (solid line), the approximation using Aggregates 6-10 (dashed line), and Aggregate 9 (dotted line). (b) Comparison of the scattering phase functions for ice crystal surface smooth, moderately rough and deeply rough conditions. (c) Comparison of the scattering phase functions for the averaged values over 1000 aggregates (solid line), the approximation using Aggregates 1-5 (dashed line), and Aggregate 5 (dotted line).

angle, $C_s(D_m,\lambda,n)$ is scattering cross section, and M is 5 and 1000 for our aggregate model and the 'real aggregate', respectively. Figure 3.10a illustrates the comparison of the scattering phase functions for large aggregates at λ=0.65 μm. The results indicate that the phase function of a large aggregate shows a slight sensitivity to particle geometry. Generally, for large particles, both Aggregate 9 and the 'real aggregates' are consistent in their representation of scattering properties. However, tiny oscillations are noticeable in the phase function of a single aggregate, especially at small scattering angles. In the 'real aggregates' and our aggregate model, these oscillations are averaged to be physically more meaningful. Figure 3.10b compares the phase functions of our aggregate model under various surface conditions. The phase function oscillation is much reduced when surface roughness is incorporated. The aggregates being considered in Fig. 3.10c are represented by Aggregate 5, Aggregates 1-5 and the 'real aggregates'. The scattering phase functions are computed by the ADDA since the size parameter is small. In the comparison between the phase functions of the 'real aggregates' and Aggregate 5, slight differences are shown in the forward scattering region. At side and back scattering angles, the phase function of Aggregate 5 is substantially different from those of the other two aggregate representations. The Student's t-test [*Freedman et al.*, 2007] is used to investigate the difference between the phase functions from the two aggregate representations. For the scattering angles of 60°-180°, the t-statistic, $|t| = 5.1862$, has exceeded the 95% confidence level ($t_{0.05} = 1.96$), which suggests that the differences in phase functions are significant between Aggregate 5 and the 'real aggregates' containing 1000 geometries. The Student's t-test can be carried out on the phase functions of the 'real aggregates' and our aggregate model. To assess the significance of our aggregate

model, the t-statistics are computed as follows:

$$|t| = 0.1405 < t_{0.05} = 1.96 \tag{3.23}$$

and

$$|t| = 0.5096 < t_{0.05} = 1.96 \tag{3.24}$$

for the phase functions at the scattering angles of 0°-180° and 60°-180°, respectively. The null hypothesis is rejected in favor of the alternative hypothesis. Therefore, the aggregate model in this study can be used to represent the 'real aggregates' in the simulation of their scattering properties.

3.5 Aggregation effect in the retrieval of ice cloud properties

To simulate ice clouds containing individual hexagonal particles and their aggregates, we first assume the geometries shown in Figs. 3.2 and 3.3. The particle sizes of the aggregates are based on a particle size distribution, which, for ice clouds, is generally parameterized by the Gamma distribution [*Heymsfield et al.*, 2002; *Kosarev and Mazin*, 1991; *Mitchell*, 1991] given by

$$n(D_m) = N_0 D_m^{\mu} \exp(-\frac{b+\mu+0.67}{D} D_m), \tag{3.25}$$

where D_m is the dimension of the aggregate, N_0 is the concentration intercept parameter, and D is the median of the distribution of D_m. The parameters, μ and b, are assumed to be 2.0 and 2.2, respectively. Clouds containing a mixture of ice habits can be generated by the decomposition of a number of aggregates into hexagonal fractions. The geometries of the fractions are dependent on the aggregate dimensions and can be derived based on the information provided in Tables 3.1 and 3.2. The effective particle sizes of the ice clouds are derived as follows:

$$D_e = \frac{3}{2}\frac{(1-f)\left[\sum_{i=1}^{24}\int_{D_{\min}}^{D_1} V_{pi}n(D_m)dD_m + \sum_{j=1}^{50}\int_{D_1}^{D_{\max}} V_{pj}n(D_m)dD_m\right] + N_a f\int_{D_{\min}}^{D_{\max}} V_a n(D_m)dD_m}{(1-f)\left[\sum_{i=1}^{24}\int_{D_{\min}}^{D_1} A_{pi}n(D_m)dD_m + \sum_{j=1}^{50}\int_{D_1}^{D_{\max}} A_{pj}n(D_m)dD_m\right] + N_a f\int_{D_{\min}}^{D_{\max}} A_a n(D_m)dD_m}, \quad (3.26)$$

where f is the proportion of the plates that form aggregates; V_{pi} and V_{pj} are the volumes of the plates in Tables 3.1 and 3.2, respectively; A_{pi} and A_{pj} are the projected areas of the plates; V_a is the averaged volume of the aggregates used to represent all aggregate ice crystals; N_a is the number of the aggregate geometries; and, D_1 is the threshold value of the aggregate dimensions to determine small and large aggregates. In this study, N_a is 5 and D_1 is assumed to be 550 μm. Note that the particle size distributions of plates are different than that of the aggregates. However, the size distributions of plates are not derived because they are not used in the computation of effective particle sizes and scattering properties of ice clouds.

The phase functions of ice clouds can be given by,

$$P_{11} = \frac{(1-f)\left[\sum_{i=1}^{24}\int_{D_{\min}}^{D_1} P_{11,pi}Q_{s,pi}A_{pi}n(D_m)dD_m + \sum_{i=25}^{74}\int_{D_1}^{D_{\max}} P_{11,pi}Q_{s,pi}A_{pi}n(D_m)dD_m\right] + N_a f\int_{D_{\min}}^{D_{\max}} P_{11,a}Q_{s,a}A_a n(D_m)dD_m}{(1-f)\left[\sum_{i=1}^{24}\int_{D_{\min}}^{D_1} Q_{s,pi}A_{pi}n(D_m)dD_m + \sum_{i=25}^{74}\int_{D_1}^{D_{\max}} Q_{s,pi}A_{pi}n(D_m)dD_m\right] + N_a f\int_{D_{\min}}^{D_{\max}} Q_{s,a}A_a n(D_m)dD_m} \quad (3.27)$$

where $P_{11,pi}$ and $Q_{s,pi}$ are the phase function and scattering efficiency for plates, and $P_{11,a}$ and $Q_{s,a}$ are the phase function and scattering efficiency for aggregates.

To investigate the influence of ice particle aggregation on the inference of ice cloud microphysical and optical properties, reflectances are simulated by the DISORT model [*Stamnes et al.*, 1988] for two channels centered at wavelengths of 0.65 and 2.13 μm. A dark (non-reflective) surface condition is assumed to eliminate the influence of

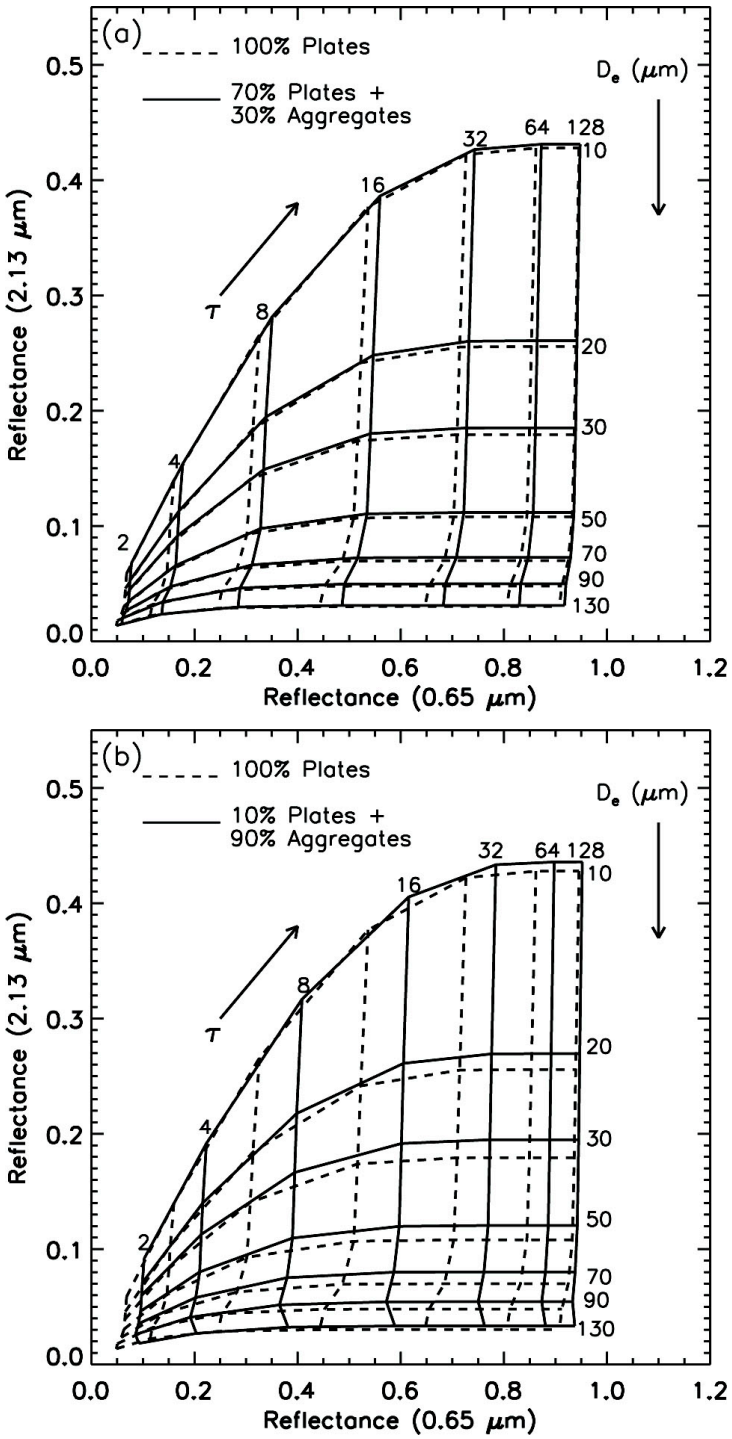

Fig. 3.11 Lookup tables using 0.65 and 2.13 μm reflectances for (a) independent plates and the same ice crystals except that 30% plates form aggregates and (b) independent plates and the same ice crystals except that 90% plates form aggregates. The solar zenith and viewing zenith angles are 30˚, respectively, and the relative azimuth angle is 90˚.

surface bidirectional reflectance features. Figure 3.11 compares the calculated lookup tables. The dashed lines in Fig. 3.11a denote hexagonal plates while the solid lines are used to indicate an ice cloud model that contains the same habits except that 30% of the plates form aggregates. From Fig. 3.11a, it can be found that the optical thicknesses of the ice clouds are reduced when aggregates are included. Based on the scattering properties of ice clouds, the optical thickness of ice crystals involving aggregates can be given as follows:

$$\tau = (1-f)\Delta z\left[\sum_{i=1}^{24}\int_{D_{\min}}^{D_1} Q_{e,pi}A_{pi}n(D_m)dD_m + \sum_{i=25}^{74}\int_{D_1}^{D_{\max}} Q_{e,pi}A_{pi}n(D_m)dD_m\right], \\ + N_a f\Delta z\int_{D_{\min}}^{D_{\max}} Q_{e,a}A_a n(D_m)dD_m \tag{3.28}$$

where Δz is the physical thickness of the cloud, and $Q_{e,pi}$ and $Q_{e,a}$ are the extinction efficiencies for plates and aggregates. The optical thickness is reduced to that of 100% plates when f is 0. From Eq. (3.28), it is known that the scattering properties and particle number concentration of ice crystals can both affect the retrieval of cloud optical thickness. Because the reduction of particle number concentration is more effective in the retrieval of cloud properties, the ice cloud optical thickness decreases in the aggregation process. This feature becomes more pronounced when 90% of the plates form aggregates as shown in Fig. 3.11b. It is also clear from Fig. 3.11 that the retrieved ice cloud effective particle sizes generally decrease when the aggregation effect is ignored in the retrieval process. The physical explanation is that the aggregation of plates has no effect on the total volume of ice crystals when the total values of the projected areas are reduced.

3.6 Summary

With a set of *in situ* measurements of aggregates as guidance, an algorithm is

developed to efficiently define the geometries of aggregates and compute their projected areas. Aggregates result from attaching ice particle hexagonal plates together in a chain-like manner. We investigate the scattering properties of randomly oriented aggregates of plates using the ADDA and IGOM for particles whose size parameters are smaller and larger than 25, respectively. The results indicate that the scattering properties are consistent in the region where the size parameter is approximately 25. The scattering phase functions of the aggregates show the same typical halo peaks at scattering angles of 22° and 46° at visible wavelengths as do hexagonal ice particles.

With the algorithm to create geometries of aggregates and their scattering properties, an investigation was made on the possibility of representing all aggregates based on the scattering properties of a limited number of aggregates. To represent small aggregates, we generated five aggregate models, with each particle consisting of 4 or 5 hexagonal plates. Aggregates with large particle sizes were built by increasing the monomer numbers instead of merely scaling the sizes of each monomer and five models consisting of 8-12 plates were considered. The scattering properties of a representative aggregate were derived by averaging values over the individual aggregate geometries. To validate our aggregate model, a ‘real aggregate’ was simulated from 1000 different plate aggregates. The comparison of the scattering properties suggested that it was not sufficient to use only one aggregate realization to represent all aggregates within ice clouds. However, the scattering properties of our aggregate model showed much better agreement with the ‘real aggregates’ and confirmed the validation of our aggregate model.

Furthermore, the influence of the aggregate of plates was investigated for the

satellite-based remote sensing of ice clouds. As cloud reflectances can be used to infer ice cloud microphysical and optical properties, we compared the lookup tables of cloud reflectances for ice cloud models involving hexagonal plates and their aggregates. The neglect of aggregates in the retrieval process leads to an overestimate of optical thickness but an underestimate of effective particle size. This result is partly due to the lower projected areas of the ice crystals during the aggregation process. More detailed investigations of the plate aggregates need to be performed in conjunction with other ice habits.

CHAPTER IV

DETERMINATION OF ICE CLOUD MODELS USING MODIS AND MISR DATA

4.1 Background

Substantial efforts have been made to improve the satellite-based retrieval of ice cloud properties by introducing realistic ice crystals within cirrus clouds. *Yang and Liou* [1998] modeled ice crystals surface roughness by using the slopes of the facets to define the degree of surface roughness. The radiation scattering by rough-surfaced hexagonal ice crystals has been investigated using both rigorous and simplified algorithms based on the ray-tracing technique [*Yang et al.*, 2008b]. The primary effect of ice crystal surface roughness, relative to using smooth crystals, is to increase the solar reflectances in visible regions at most angles and to decrease the retrieved ice cloud optical thicknesses [*Yang et al.*, 2008a]. *Xie et al.* [2009] investigated the scattering properties of inhomogeneous ice crystals based on observations, in which atmospheric ice crystals were collected near the surface and studied under with a binocular microscope [*Tape*, 1994]. Inhomogeneous ice crystals, containing spherical or spheroidal air bubbles, were confirmed to have the effect of reducing the ice cloud optical thicknesses when they were used in the satellite-based retrieval of ice cloud properties. In addition, air bubbles within ice crystals may substantially reduce the ice crystal volumes and affect the retrieval of ice cloud particle sizes.

A new ice cloud model is demanded to employ the new ice crystal geometries and improve the satellite-based retrieval of ice cloud properties. In this study, we develop an

ice cloud reflectance model using simple, but appropriate ice crystal habit and size distributions, to minimize directional reflectance uncertainties employing matched data from the MODerate-resolution Imaging Spectroradiometer (MODIS) and Multiangle Imaging SpectroRadiometer (MISR) on board the National Aeronautics and Space Administration's (NASA's) Terra spacecraft. Given all of the uncertainties of the operationally retrieved ice cloud properties, the resulting ice cloud model exhibits excellent consistency with the measurements from the 9 MISR views.

In section 4.2, we introduce the study of ice crystal habits and their sensitivity to the scattering properties and solar reflectances of cirrus clouds. In section 4.3, we describe the MODIS and MISR data used in the retrieval of ice cloud properties, and develop a methodology to determine an optimal ice cloud model for routine retrieval of ice cloud properties using reflected solar radiation. In section 4.4, we analyze the potential errors in retrieved ice cloud optical thicknesses in a case in which MODIS data are not employed in the retrieval. In section 4.5, the errors caused by ice cloud models and their scattering properties is addressed through analyses of viewing angle dependence of retrieved ice cloud optical thickness, and an ice cloud model with mixed ice crystal habits is selected from two hundred models. Conclusions are provided in section 4.6.

4.2 Ice cloud models and their sensitivity to the simulations of scattering properties and solar reflectances by cirrus clouds

4.2.1 Ice cloud models

Nearly all atmospheric ice crystals develop on the fundamental hexagonal matrix that results from the near tetrahedral bonding angles of the water molecule. Hexagonal ice crystals, in one form or another, are one of the most important ice crystal shapes within cirrus clouds. In the current study, only hexagonal columns and plates are assumed in developing an algorithm to determine optimal ice cloud models for satellite-based remote sensing of cirrus clouds. Other ice crystal habits such as bullet rosettes, droxtals, hollow columns, and aggregates, often observed in clouds could also be used for the ice cloud models to, perhaps, further improve their performance in retrieving ice cloud properties [*Baum et al.*, 2003; *Baum et al.*, 2005a; *Baum et al.*, 2005b]. The habit fractions of ice crystals may have regional preferences and are strongly related to cloud temperature. This aspect may deserve future study but is beyond the aim of this work.

Hexagonal ice crystal geometries are normally specified by their aspect ratios, α=2a/L, where a and L are the semi-width and length of the ice particles, respectively. The aspect ratios of hexagonal columns used in this study are consistent with those of Mitchell and Arnott [1994] and can be formulated as follows,

$$\alpha = \begin{cases} 0.7 \quad for \quad D < 100\mu m \\ \\ 6.96L^{-0.5} \quad for \quad D \geq 100\mu m \end{cases}, \tag{4.1}$$

where D represents the dimensions of the ice crystals and equals L for hexagonal columns. For hexagonal plates, the aspect ratios are determined based on in situ

measurements of cirrus clouds [*Auer and Veal*, 1970; *Pruppacher and Klett*, 1980] and can be given by,

$$\alpha = \begin{cases} 1 \quad for \quad D \le 4\mu m \\ \dfrac{a}{0.2227a + 1.5547} \quad for \quad 4\mu m < D < 10\mu m, \\ 0.8038a^{0.526} \quad for \quad D \ge 10\mu m \end{cases} \tag{4.2}$$

where D=2a.

Ice crystals with roughened surfaces or internal air bubbles are also considered here because they keep the simple hexagonal shape while significantly altering the optical properties. As in Yang et al. [2008b], the RMS tilt, σ, of the roughened facets on the ice crystal surfaces is used to specify the degree of roughness. Thus, the surface condition varies from smooth to severely rough as σ increases from 0 to 1. The geometries of inhomogeneous ice crystals have been described in detail by *Xie et al.* [2009] and will not be restated here in the interest of brevity. The internal air bubbles of the inhomogeneous ice crystals are simulated using spheroidal shapes that satisfy

$$\frac{x^2}{r_1^2} + \frac{y^2}{r_2^2} + \frac{z^2}{r_3^2} = 1, \tag{4.3}$$

where r_1, r_2, and r_3 are the air bubble radii. Here, r_1, r_2, and r_3 depend on the widths and lengths of the ice crystals as follows:

$$r_1 = C_{bubble} a \tag{4.4}$$

$$r_2 = C_{bubble} a \tag{4.5}$$

$$r_3 = C_{bubble} L, \tag{4.6}$$

where C_{bubble} is a constant.

For the ice cloud models, the ice crystal surface roughness condition and internal air bubbles are used for both the hexagonal column and plates cases. The geometric parameters σ and C_{bubble} are set to be 1.0 and 0.5, respectively, indicating a case with severely roughened ice crystals and a case with medium-sized air bubbles. Thus, the scattering properties of cirrus clouds are represented by ice cloud models consisting of six types of ice crystals including hexagonal column (HC), surface roughened column (RC), inhomogeneous column (IC), hexagonal plate (HP), surface roughened plate (RP), and inhomogeneous plate (IP). Figure 4.1 compares the projected area and volume of these ice crystals as functions of ice crystal dimension. The degree of ice crystal surface roughness has not been considered in the computation of the projected areas and volumes of the ice crystals. As can be seen in Figs. 4.1a and 4.1b, the projected areas of HP are much larger than HC when the dimensions are greater than 250 μm. However, the volume of HC is greater than HP in the region of 0 to 500 μm as shown in Figs. 4.1c and 4.1d. Note that the internal air bubbles within ice crystals substantially reduce their volumes while having no effect on the projected areas.

To quantitatively characterize the cirrus cloud particle sizes, we use the cloud effective particle from [*Foot*, 1988]:

$$D_e = \frac{3}{2}\frac{\int_{D_{\min}}^{D_{\max}} V_{total}(D)n(D)dD}{\int_{D_{\min}}^{D_{\max}} A_{total}(D)n(D)dD}, \tag{4.7}$$

where n(D) is ice particle size distribution; $V_{total}(D)$ and $A_{total}(D)$ are the total volumes and projected areas of the ice crystals for size D, respectively; and, D_{max} and D_{min} are the maximum and minimum values of D. Based on a number of cirrus cloud measurements

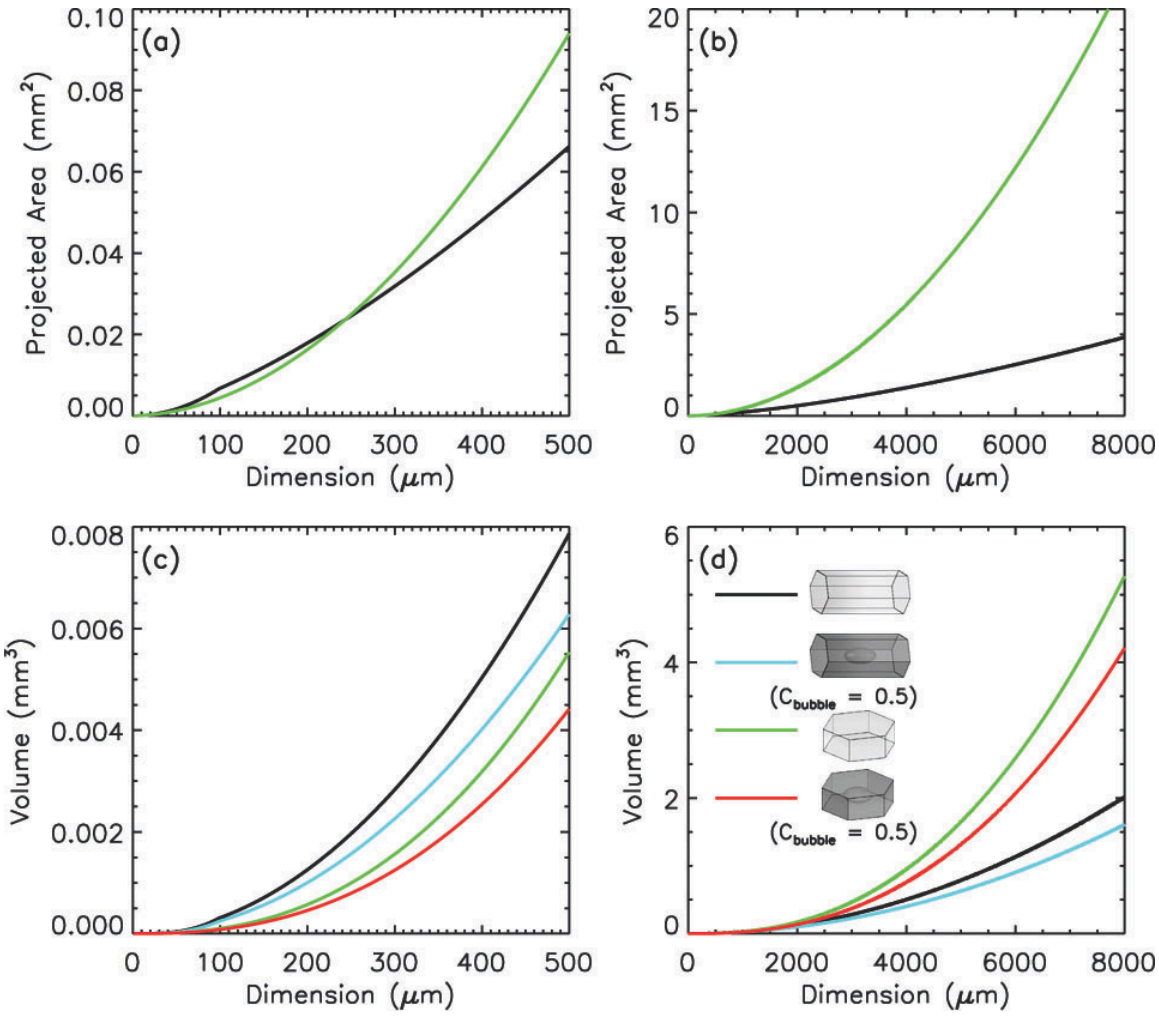

Fig. 4.1 Ice crystal projected area versus dimension (a, b): for HC (black) and HP (blue) models, and (c, d): Variation of ice crystal volume versus dimension for HC (black lines), IC (blue), HP (green), and IP (red).

during field campaigns [*Heymsfield et al.*, 2002; *Kosarev and Mazin*, 1991; *Mitchell*, 1991], the size distribution of ice cloud particles can be represented by the Gamma distribution given by,

$$n(D) = N_0 D^{\mu} \exp(-\frac{b+\mu+0.67}{D_{median}} D), \tag{4.8}$$

where D_{median} is the median value of D, N_0 is the concentration intercept parameter, and μ and b are constants assumed to be 2.0 and 2.2, respectively. $V_{total}(D)$ and $A_{total}(D)$ in Eq (4.7) are given as

$$\begin{aligned} V_{total}(D) = {} & C_{HC}V_{HC}(D) + C_{RC}V_{RC}(D) + C_{IC}V_{IC}(D) + \\ & C_{HP}V_{HP}(D) + C_{RP}V_{RP}(D) + C_{IP}V_{IP}(D) \end{aligned}, \tag{4.9}$$

$$\begin{aligned} A_{total}(D) = {} & C_{HC}A_{HC}(D) + C_{RC}A_{RC}(D) + C_{IC}A_{IC}(D) + \\ & C_{HP}A_{HP}(D) + C_{RP}A_{RP}(D) + C_{IP}A_{IP}(D) \end{aligned}, \tag{4.10}$$

where $V_{HC}(D)$, $V_{RC}(D)$, $V_{IC}(D)$, $V_{HP}(D)$, $V_{RP}(D)$, and $V_{IP}(D)$ and $A_{HC}(D)$, $A_{RC}(D)$, $A_{IC}(D)$, $A_{HP}(D)$, $A_{RP}(D)$, and $A_{IP}(D)$ are the volumes and projected areas, respectively, of the aforementioned ice crystal habits; and, $C_{HC}(D)$, $C_{RC}(D)$, $C_{IC}(D)$, $C_{HP}(D)$, $C_{RP}(D)$, and $C_{IP}(D)$ are habit fractions of the ice crystals. Thus, the goal of this study is to determine the appropriate coefficients $C_{HC}(D)$, $C_{RC}(D)$, $C_{IC}(D)$, $C_{HP}(D)$, $C_{RP}(D)$, or $C_{IP}(D)$ by using satellite observations on a global scale.

4.2.2 Sensitivity of ice cloud models to the simulations of their scattering properties

For single ice crystals, the light scattering properties are simulated by an Improved Geometric Optics Method (IGOM) [*Yang and Liou*, 1996b]. After simulation, the scattering properties including scattering phase functions, $P_{11}(\Theta)$, extinction

efficiencies Q_e, and single scattering albedos ω of an ensemble of ice crystals can be derived on the basis of ice crystal habit and size distributions as follows:

$$P_{11}(\Theta) = \frac{\int_{D_{\min}}^{D_{\max}} \left[\sum_i C_i P_{11,i}(\Theta, D) Q_{s,i}(D) A_i(D) \right] n(D) dD}{\int_{D_{\min}}^{D_{\max}} \left[\sum_i C_i Q_{s,i}(D) A_i(D) \right] n(D) dD}, \tag{4.11}$$

$$Q_e = \frac{\int_{D_{\min}}^{D_{\max}} \left[\sum_i C_i Q_{e,i}(D) A_i(D) \right] n(D) dD}{\int_{D_{\min}}^{D_{\max}} \left[\sum_i C_i A_i(D) \right] n(D) dD}, \tag{4.12}$$

$$\omega = \frac{\int_{D_{\min}}^{D_{\max}} \left[\sum_i C_i Q_{s,i}(D) A_i(D) \right] n(D) dD}{\int_{D_{\min}}^{D_{\max}} \left[\sum_i C_i Q_{e,i}(D) A_i(D) \right] n(D) dD}, \tag{4.13}$$

where $P_{11,i}(\Theta)$ is the scattering phase function; $Q_{e,i}$ and $Q_{s,i}$ are the extinction and scattering efficiencies, respectively, for each ice crystal habit; and i=HC, RC, IC, HP, RP, or IP.

Figure 4.2 compares the scattering phase functions of the ice cloud models for D_e=50 μm. To investigate the sensitivity of the phase function to ice cloud modes, each ice cloud model consists of only one ice crystal habit, thus, five of the habit fractions are zero for each ice cloud model. From Fig. 4.2, HPs are seen to generally have larger forward scattering than HCs, although both ice cloud models have the same cloud particle size. Most HPs have larger projected areas than HCs for the same dimensions (see Fig. 4.1). Therefore, the diffraction of HPs is more significant than the scattering of light by the ice crystals. At a wavelength of λ=0.866 μm (see Fig. 4.2a), the phase functions of HCs and HPs have strong forward and backward scattering and distinct halo peaks at the

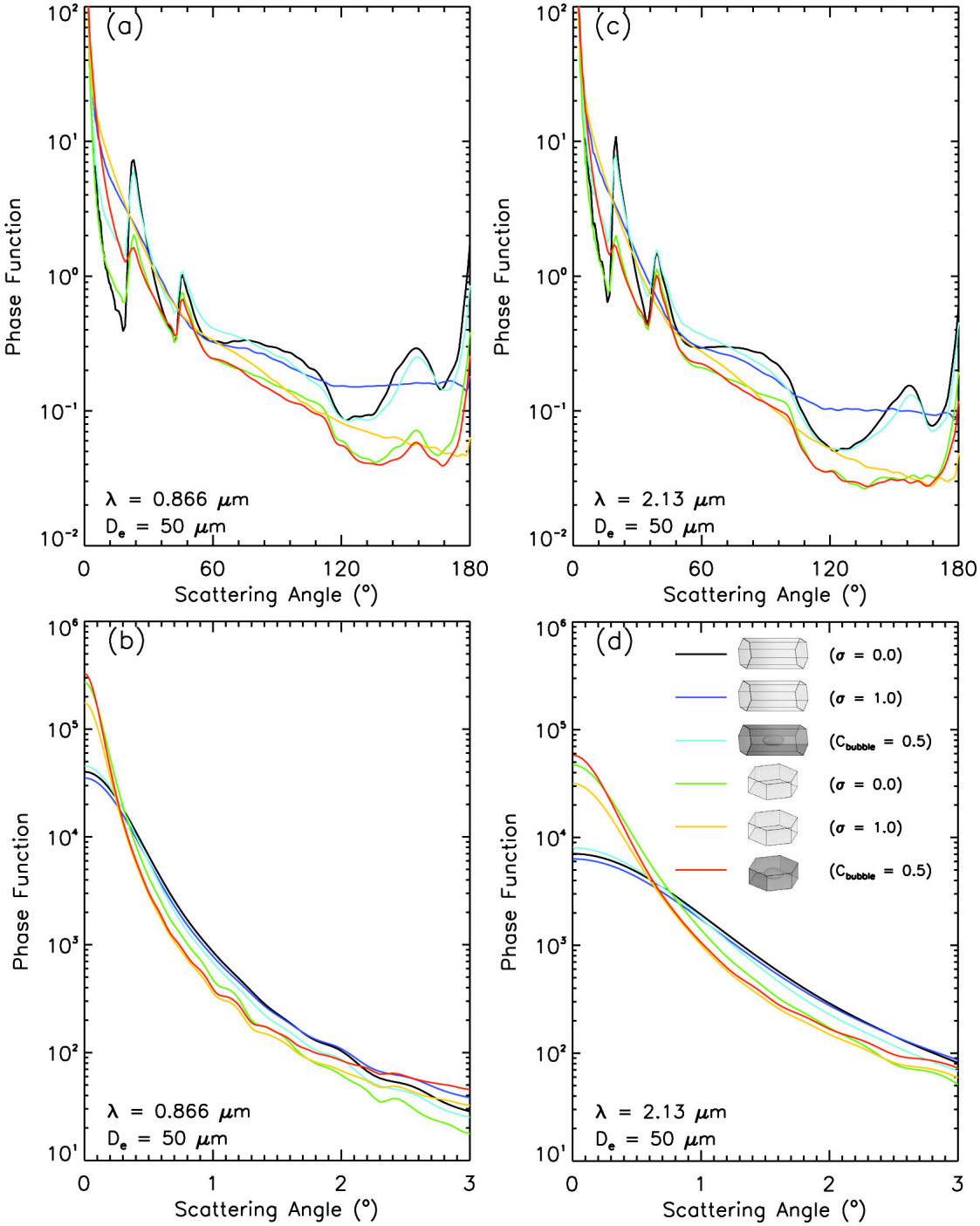

Fig. 4.2 Scattering phase functions for HC (black), RC (blue), IC (cyan), HP (green), RP (yellow), and IP (red) models composed of randomly oriented ice crystals.

scattering angles near 22° and 46°. When surface roughness is introduced (i.e., RC and RP), the phase function halo features, caused by solar beams refracted by hexagonal ice crystals, completely vanish. Moreover, the forward and backward scattering of HCs and HPs are reduced due to light beam spreading in the refraction processes of the ice crystals [*Yang et al.*, 2008b]. As discussed by *Xie et al.* [2009], the inhomogeneity effect on the phase functions can also be seen for single ICs and IPs. However, the volumes of ICs and IPs are smaller than HCs and HPs because the air bubbles are subtracted. To achieve the same cloud effective particle sizes, inhomogeneous ice crystals in the ice cloud models have larger dimensions and larger aspect ratios than homogeneous ones. Thus, the forward scattering of the IC and IP models is stronger than that for the HC and HP models as shown in Fig. 4.2b. Figures 4.2c and 4.2d compare the six phase functions of the ice cloud models at the wavelength of λ=2.13 μm. At the near-infrared wavelength, the smoothing of the scattering phase functions is shown for ice cloud models consisting of RCs, RPs, ICs, and IPs. At the near-infrared wavelength, the smoothing of the scattering phase functions for the RC, RP, IC, and IP models relative to the homogeneous models is similar to that seen at 0.866 μm. As λ increases from 0.866 to 2.13 μm, the phase functions of the ice cloud models decrease in the forward scattering directions, because the ice crystal size diminishes relative to the wavelength.

4.2.3 Sensitivity of solar reflectance to cirrus ice particle habit

To retrieve ice cloud optical and microphysical properties, simulated cloud bi-directional reflectances are typically matched with satellite observations at solar wavelengths. Because the simulated cloud reflectances are sensitive to the particle habits

used in the models, the retrieved properties will vary with the ice crystal scattering model used. This sensitivity needs to be quantified to understand its impact on the retrievals. The satellite observed cloud bi-directional reflectance is defined by

$$R(\mu_0,\mu,\phi)=\frac{\pi I(\mu,\phi)}{\mu_0 F}, \tag{4.14}$$

where F denotes the direct solar flux density at the top of the atmosphere; μ_0 and μ are the cosine values of the solar and satellite viewing zenith angles, θ_0 and θ, respectively; ϕ is the relative azimuth angle; and, $I(\mu, \phi)$ is the radiance observed by the satellite instruments. The relative azimuth angle ϕ can be specified as follows:

$$\phi=\begin{cases}|\varphi-\varphi_0| \quad for \quad 0^\circ \le |\varphi-\varphi_0| \le 180^\circ \\ \\ 360^\circ-|\varphi-\varphi_0| \quad for \quad |\varphi-\varphi_0|>180^\circ\end{cases} \tag{4.15}$$

where φ_0 and φ are the solar and satellite viewing azimuth angles, respectively. The solar and satellite viewing geometries are demonstrated by the coordinate system oxyz (see Fig. 4.3) in which the o is the viewing target on the Earth surface, the z axis is along the direction of the ellipsoid normal, and the x axis points toward the local north.

Figures 4.4 and 4.5 show the simulated cloud bi-directional reflectances using the six ice cloud models. The cloud reflectances were computed by Discrete Ordinates Radiative Transfer (DISORT) [*Stamnes et al.*, 1988] assuming a homogenous ice cloud layer over a black surface, a cloud optical thickness of 1, and θ_0=30°. In each panel of Figs. 4.4 and 4.5, θ increases from 0° to 90° along the radial direction, and $|\varphi_0-\varphi|$ varies along the angular direction from 0° to 360°. At a wavelength of λ=0.866 μm, Fig. 4.4 clearly shows the cloud reflectance is sensitive to viewing geometries. At θ_0=30°, the maximum values of the cloud reflectances are associated with the forward directions

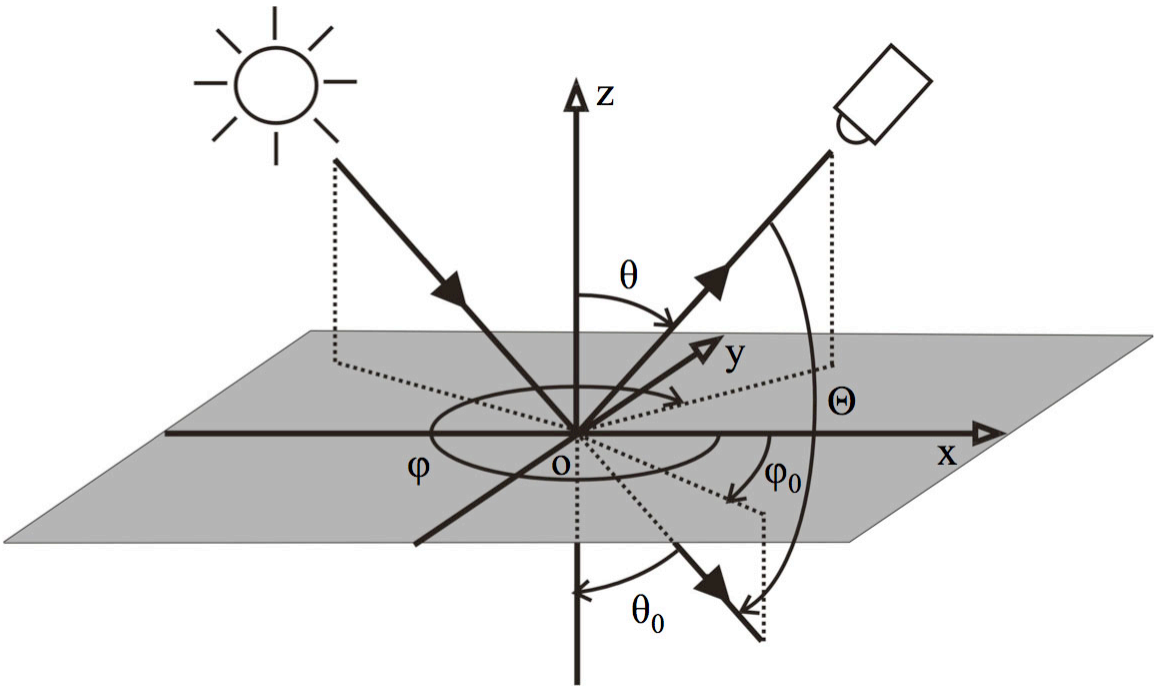

Fig. 4.3 Solar and satellite viewing geometries. θ_0 and θ range between 0° and 90°; φ_0 and φ range between 0° and 360°; and Θ varies from 0° to 180°.

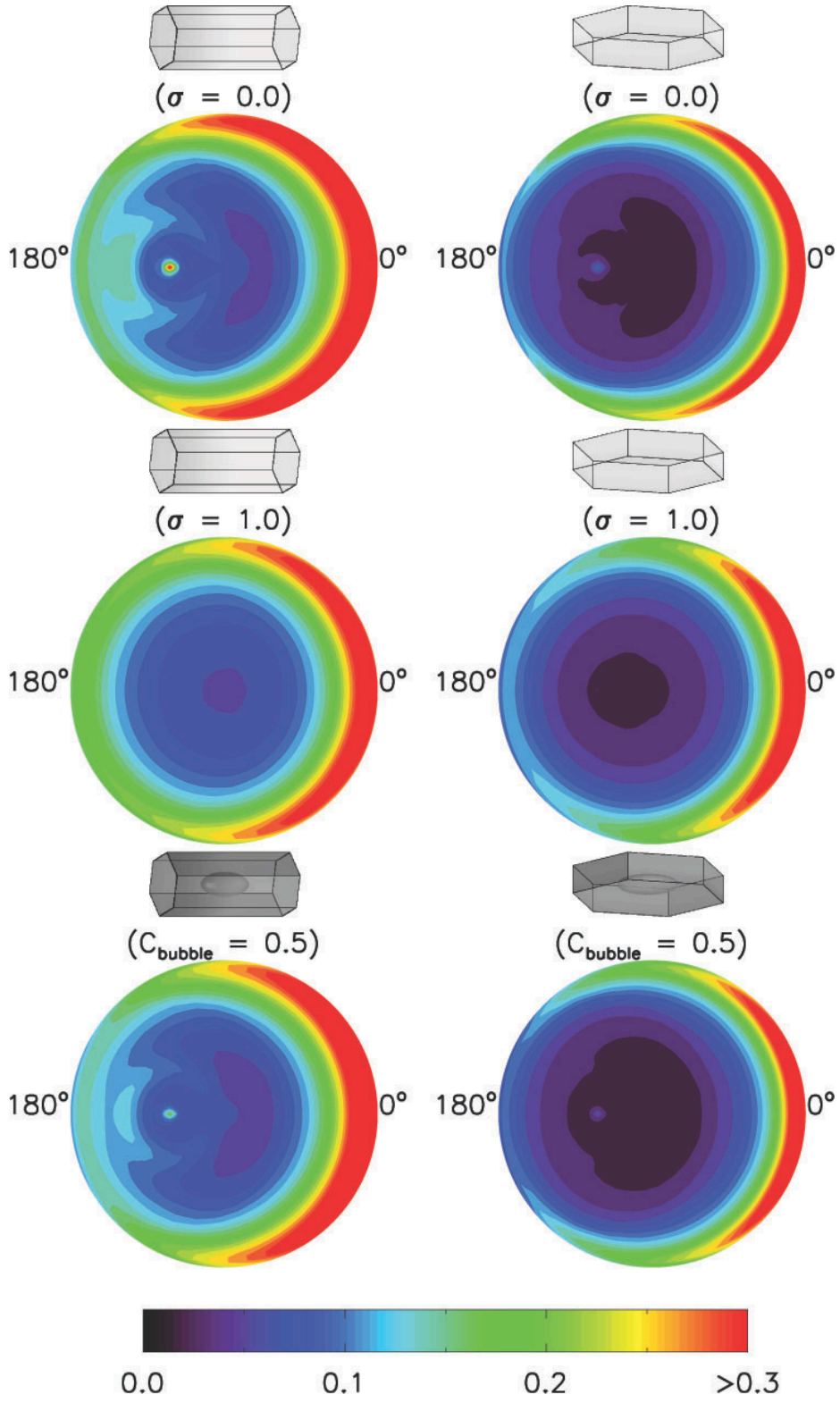

Fig. 4.4 Cloud bidirectional reflectances computed for the HC, RC, IC, HP, RP, and IP ice cloud models for θ_0=30°, D_e=50 μm, and λ=0.866 μm.

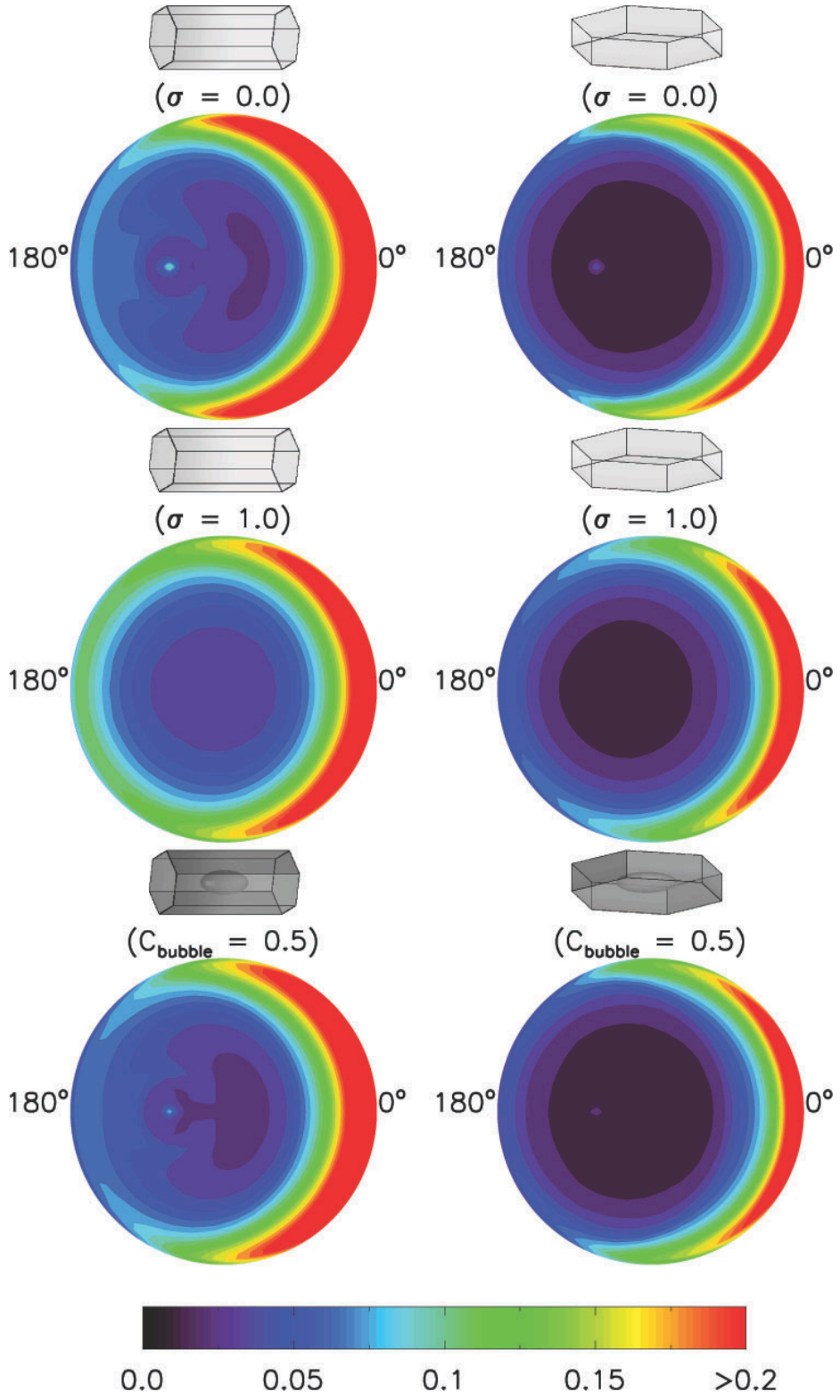

Fig. 4.5 Same as Fig. 4.4 except for λ=2.13 μm.

where θ is between 80° and 90°. In the backscattering directions, the cloud reflectance maxima occur at θ=30° and are correlated to the phase function maxima at Θ=180°. Clearly, the cloud reflectances in Fig. 4.4 are sensitive to the use of ice cloud models. For θ=0-45°, a range frequently used for satellite-based retrievals, the HP, RP, and IP reflectances are much smaller than their columnar counterparts. This is probably due to stronger forward scattering by plates (Fig. 4.2). The relative maxima at Θ=180° in the HC and HP phase functions (Fig. 4.2), yield the nearly pinpoint backscattering reflectance maxima seen in both Figs. 4.4 and 4.5. However, these maxima are significantly reduced for the inhomogeneous ice crystals and absent for the rough crystal reflectances as a result of their smoother phase functions. The sensitivity of cloud reflectances to the choice of ice cloud model is evident in the simulations at both wavelengths. Therefore, the ice crystal habit fractions in the ice cloud models will significantly affect the simulations of cloud reflectances and the retrieval of ice cloud properties.

4.3 Data and methodology

4.3.1 Terra MODIS and MISR data

Terra, launched on 18 December 1999, is a scientific research satellite component of the Earth Observing System (EOS). The MODIS instrument is designed to monitor the state of the Earth's environment including the radiation processes occurring in the atmosphere and at the Earth's surface. MODIS has 36 bands ranging in wavelengths from 0.414 μm to 14.235 μm [*Ardanuy et al.*, 1991]. In this study, the MODIS bands centered

at 0.86 and 2.13 μm are used to derive the ice cloud optical thickness and effective particle sizes over ocean because of the relatively small oceanic reflectance and atmospheric absorption at those wavelengths [*Gatebe et al.*, 2005; *Pinker and Laszlo*, 1992]. In the retrieval process, the viewing and illumination geometries and reflectances at the top of the atmosphere (TOA) are provided by the MODIS Level-1B Calibrated Geolocation Data Set (MOD 02) at a spatial resolution of 1 km × 1 km. The cloud thermodynamic phase is taken from the 1-km resolution cloud product (MOD 06). The MOD 02 and MOD 06 data are stored in MODIS granules, each consisting of a 5-minute data swath.

The Terra MISR instrument is designed to simultaneously provide measurements of daytime shortwave radiances from 9 distinct cameras that view the nadir direction and the forward and aftward local vertical directions [*Diner et al.*, 1989; *Diner et al.*, 1998; *Diner et al.*, 2002]. MISR's cameras are designated as Df, Cf, Bf, Af, An, Aa, Ba, Ca, and Da, where n denotes the nadir direction, and f and a indicate whether the camera points forward or aftward along the Terra ground track. Except for the nadir camera, D, C, B, and A represent the satellite viewing zenith angles of 70.5°, 60.0°, 45.6°, and 26.1°, respectively. Each of the 9 MISR cameras views the Earth in four spectral bands with central wavelengths at 0.446 (blue band), 0.558 (green band), 0.672 (red band), and 0.866 μm (NIR band) [*Diner et al.*, 2002].

The Sun-synchronous Terra orbits have an exact 16-day repeating cycle. Because of this periodicity, MISR Level 1-2 data and data processing are divided into 233 discrete paths for the entire mission period. Each MISR path is further divided into 180 blocks with block 1 starting in the Arctic and block 180 ending in the Antarctic. Each block has

a fixed sub-orbital area and corresponds to a fixed latitude, but block number is a non-uniform function of latitude. For the local mode radiances in the MISR Level-1B2 products (MI1B2T), MISR retains the full spatial resolution (275 m × 275 m) for all spectral bands and views, and each block has 512 × 2048 pixels. In the global mode, only the red-band and nadir-view radiances of the MIB2T have the full spatial resolution while other bands and views have data at a 1.1 km × 1.1 km resolution.

The MISR Level-1B2 data and the retrieved Reflecting Level Reference Altitude (RLRA) values are used to develop the MISR Level 2 cloud product (MIL2TCAL) where the multi-angle reflectances from the 9 cameras are registered at the height of the reflecting level [*Diner et al.*, 1997]. The 2.2-km resolution MIL2TCAL data are employed to derive ice cloud optical thicknesses using multi-angle cloud reflectances measurements.

Figure 4.6 shows a RGB image of MODIS radiances over the central Pacific Ocean acquired at 20:50 UTC, 2 July 2009. The image was created using a MODIS Level-1B granule, which corresponds to 1354 × 2030 1-km pixels. The white boxes are the simultaneous MISR observation domains for blocks 78-95 in Path 60. In Fig. 4.6, the MISR region can be seen overlapped by the MODIS granule. By matching the MODIS data at 2.13 μm with the overlapping MISR data it is possible to provide additional information, e.g., particle size, to the MISR retrievals of ice cloud optical properties.

Figure 4.7a compares the MODIS band 1 (centered at 0.65 μm) and MISR red band (centered at 0.672 μm) reflectances for the region covered by the MISR blocks in Fig. 4.6. The MODIS and MISR reflectances are sorted into 1° × 1° latitude-longitude regions in Fig. 4.6 when the viewing zenith angles of the MODIS instrument are within

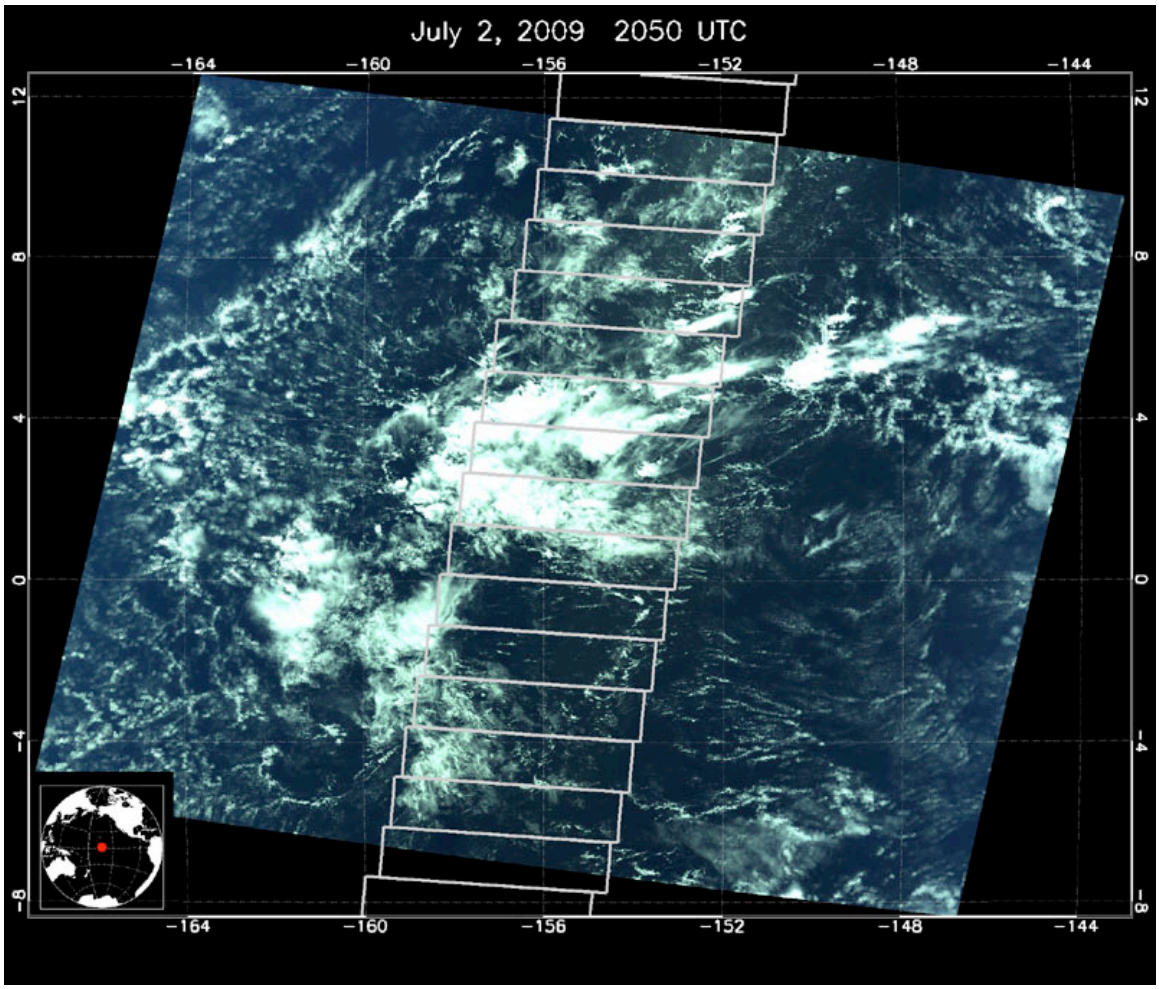

Fig. 4.6 MODIS RGB (R for band 1; G for band 4; B for band 3) image over central Pacific Ocean, 2050 UTC, 2 July 2009. The white boxes indicate blocks 78 through 95 of MISR Path 60.

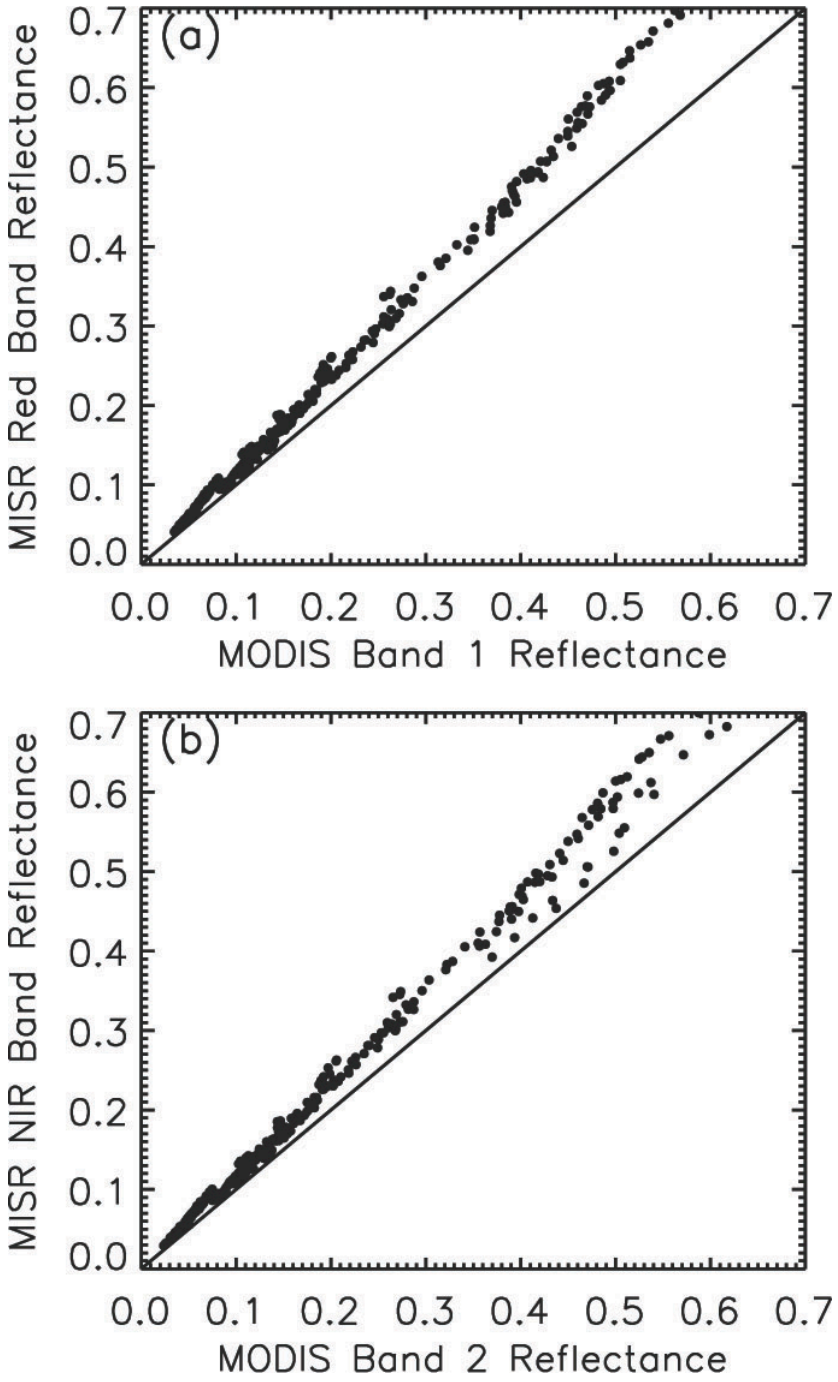

Fig. 4.7 (a) MODIS band 1 (centered at 0.65 μm) and MISR red band (centered at 0.672 μm) reflectances and (b) MODIS band 2 (centered at 0.86 μm) and MISR NIR band (centered at 0.866 μm) reflectances for the region covered by the MISR blocks in Fig. 4.6.

0.5° of the MISR An camera. The averaged reflectances and viewing zenith angles over the 1° × 1° regions are given as follows:

$$\overline{R}_{MODIS} = \frac{\sum_{i=1}^{N_{MODIS}} R_{MODIS,i}\mu_{0,MODIS,i}}{\sum_{i=1}^{N_{MODIS}} \mu_{0,MODIS,i}}, \tag{4.16}$$

$$\overline{R}_{MISR} = \frac{\sum_{i=1}^{N_{MISR}} R_{MISR,i}\mu_{0,MISR,i}}{\sum_{i=1}^{N_{MISR}} \mu_{0,MISR,i}}, \tag{4.17}$$

$$\overline{\theta}_{MODIS} = \frac{1}{N_{MODIS}} \sum_{i=1}^{N_{MODIS}} \theta_{MODIS,i}, \tag{4.18}$$

$$\overline{\theta}_{MISR} = \frac{1}{N_{MISR}} \sum_{i=1}^{N_{MISR}} \theta_{MISR,i}, \tag{4.19}$$

where N is the number of pixels within a 1° × 1° region and the subscripts, MODIS, MISR and i denote MODIS, MISR, and pixel number, respectively. From Fig. 4.7a, it is clear the MODIS and MISR reflectances have a strong linear relationship in the same viewing directions. The relative difference (RD) between the MODIS band 1 and MISR red band reflectances is specified by

$$RD = \frac{1}{N_R} \sum_{i=1}^{N_R} \frac{\overline{R}_{MISR} - \overline{R}_{MODIS}}{\overline{R}_{MISR}} \times 100\% = 16.48\%, \tag{4.20}$$

where N_R is the total number of the 1° × 1° regions in the MISR blocks seen in Fig. 4.6, and R represents the measured reflectance. The difference between the R_{MODIS} and R_{MISR} is partially due to the different solar radiances in MODIS band 1 and MISR red band. Figure 4.7b is the same as Fig. 4.7a except the comparisons are performed between the reflectances in MODIS band 2 (centered at 0.86 μm) and the MISR NIR band (centered

at 0.866 μm). The RD of the reflectances at around 0.86 μm is 15.54%. Therefore, the observations from the MODIS and MISR instruments are consistent with each other.

4.3.2 Algorithm to retrieve ice cloud optical thickness using MODIS and MISR data

The first step in determining the optimal ice cloud model is the retrieval of the ice cloud optical and microphysical properties. The cloud reflectances are simulated in MODIS bands 2 and 7 and the MISR NIR band for the cloud optical thickness τ=0.05, 0.1, 0.2, 0.5, 1.0, 2.0, 4.0, 6.0, 8.0, 10.0, 12.0, 14.0, 16.0, 18.0, 20.0, 25.0, 30.0, 35.0, 40.0, and 50.0. The cloud optical thicknesses at λ = 0.866 μm (hereafter referred to as $\tau_{0.866}$) are used as the reference optical thickness. The optical thicknesses at other wavelengths is related to $\tau_{0.866}$ by

$$\tau = \frac{Q_e}{Q_{e,0.866}} \tau_{0.866}, \tag{4.21}$$

where Q_e represents the extinction efficiency of a given ice cloud model. The solar and satellite viewing zenith angles are constructed using μ_0/μ=1.0, 0.95, …, 0.0, and the relative azimuth angles ϕ are 0°, 2.5°, 5.0°, 10.0°, …, 175.0°, 177.5°, and 180.0°.

Figure 4.8 shows a flow-chart of the algorithm for retrieving ice cloud effective particle sizes using MODIS data. The simulated cloud reflectances are first interpolated in cloud optical thickness, particle size, and solar and satellite viewing angles. For a cloud within a MODIS pixel, the thermodynamic phase is provided by the MOD 06. The effective particle size of an ice cloud is initially assumed to be 100 μm. The value of $\tau_{0.86}$ is retrieved by matching the MOD02 band-2 reflectance to the reflectance simulated for each ice cloud model associated with D_e=100 μm. A new effective particle size, D_{e2}, of

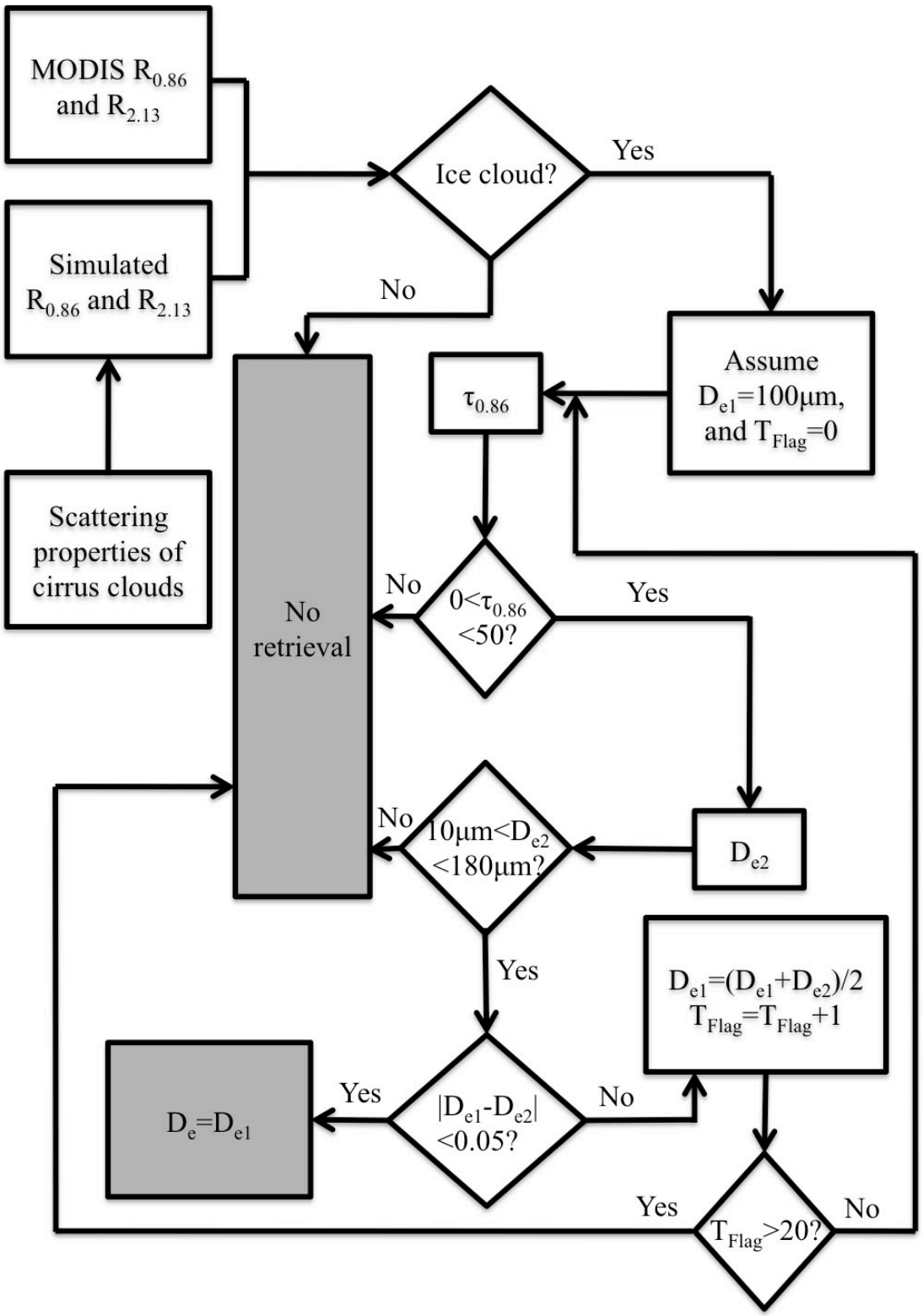

Fig. 4.8 Flow-chart of the algorithm for retrieving ice cloud effective particle sizes using MODIS data.

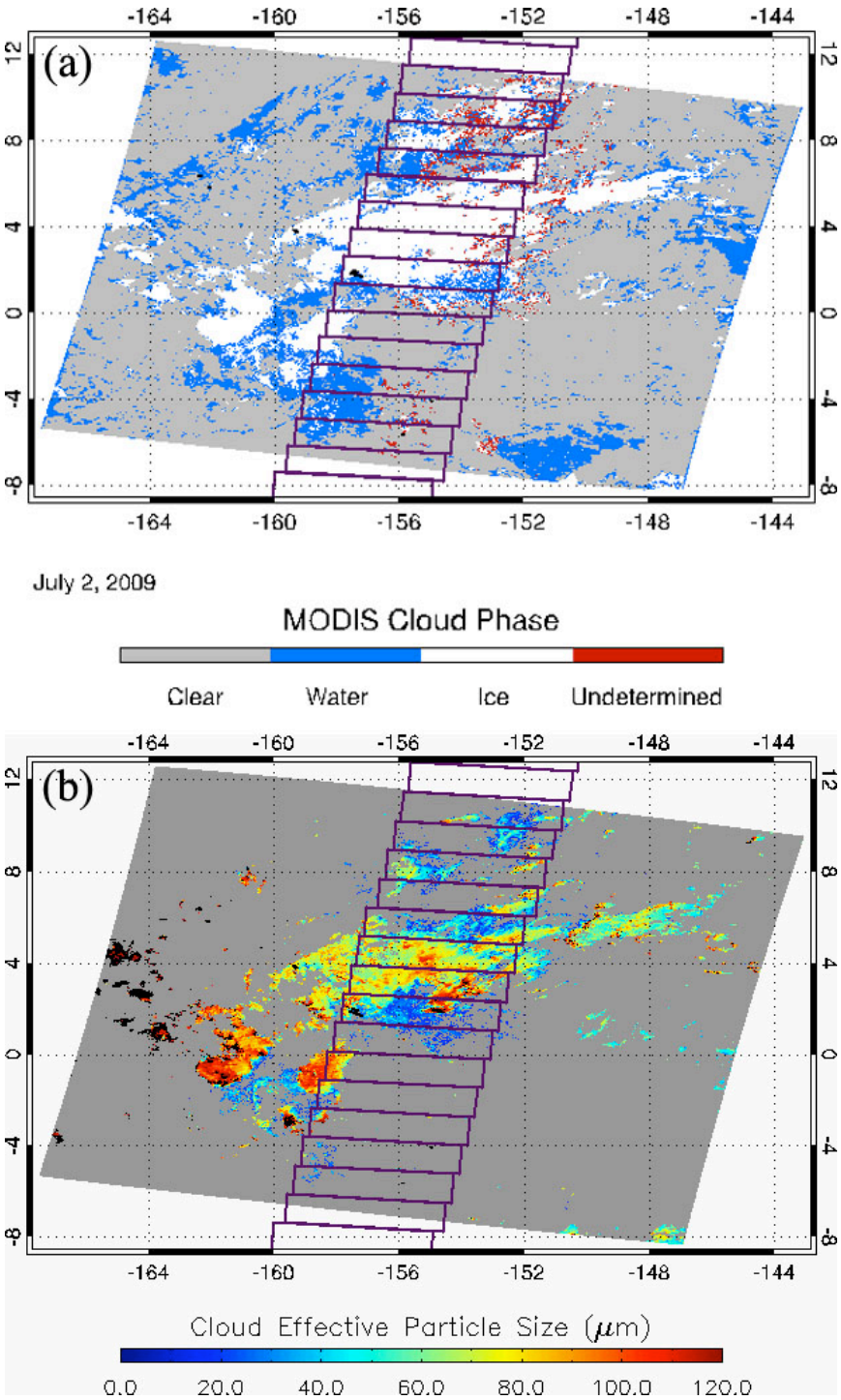

Fig. 4.9 Cloud properties determined from radiances corresponding to image in Fig. 4.6. (a) Thermodynamic phase, (b) Ice cloud effective particle sizes derived using HC ice cloud model.

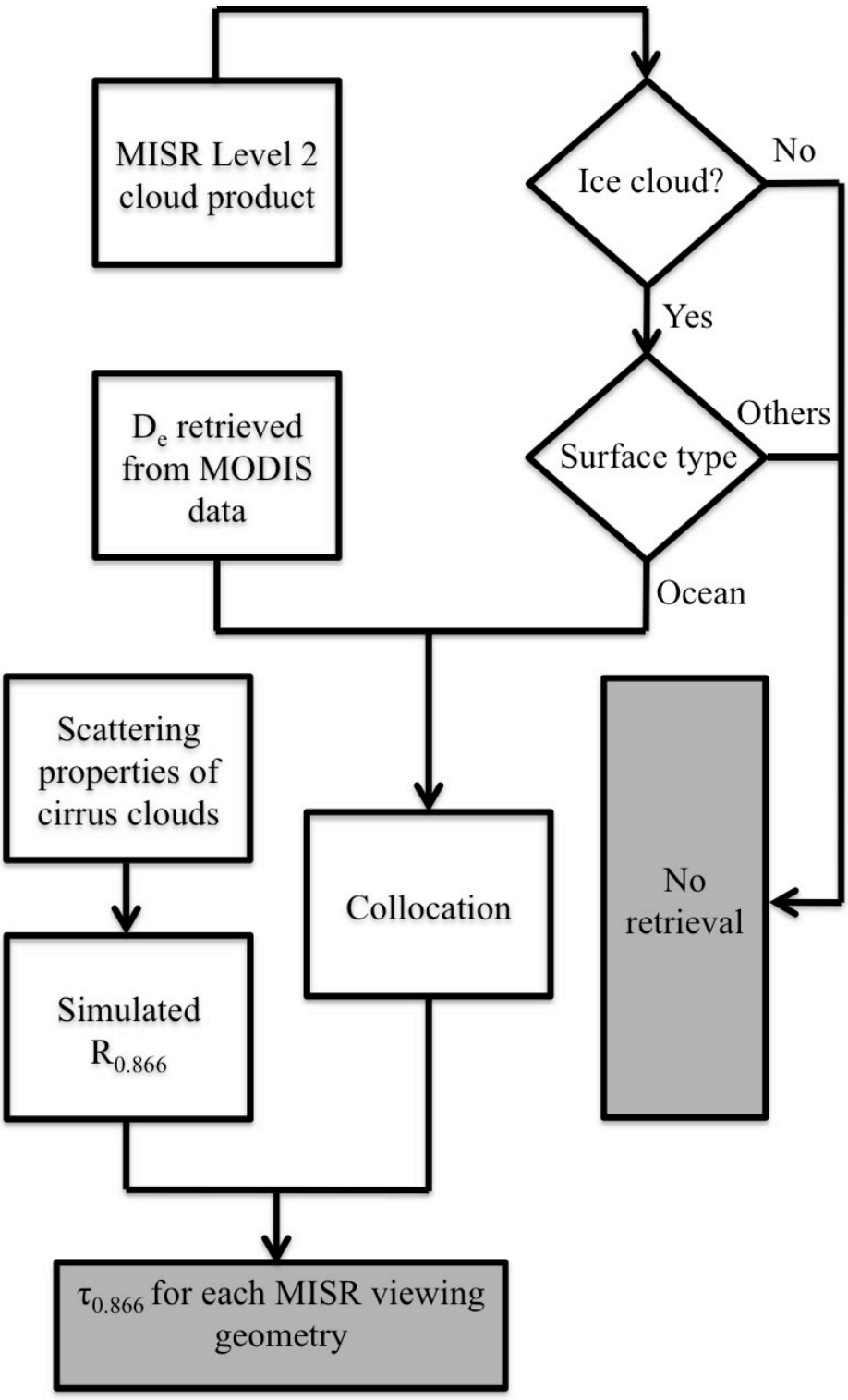

Fig. 4.10 Flow-chart of the algorithm for retrieving ice cloud optical thickness using matched MODIS and MISR data.

the ice cloud is then computed using the MOD02 band-7 reflectance and $\tau_{2.13}$ is determined with Eq (4.21) using the retrieved $\tau_{0.86}$. The final retrieval of the cloud particle size is equal to its initial guess (D_{e1}) when $|D_{e1}- D_{e2}|$ is negligible. Otherwise, the retrieval process is repeated, using an adjusted D_{e1}, until the cloud effective particle size is retrieved or a specific stopping criterion is met.

Figure 4.9 shows the cloud thermodynamic phases and D_e retrieved using the HC model reflectances for the image in Fig. 4.6. The MODIS-retrieved cloud particle sizes within the MISR blocks can be used to retrieve the ice cloud optical thicknesses from MISR data. Figure 4.10 outlines the process for retrieving $\tau_{0.866}$ at different satellite viewing geometries. The retrieval is limited to MISR pixels over ocean that are overcast by ice clouds. The MODIS retrieved cloud effective particle sizes, averaged over four contiguous MODIS pixels, are collocated with MISR pixels in 2.2 km × 2.2 km regions, when more than 70% of the MISR pixels are covered by the MODIS pixels. The 4-pixle D_e average is also compared with those for the surrounding 12 MODIS pixels to test the scene for uniformity. The cloud optical thickness retrieval is not performed when the D_e difference with the surrounding pixels exceeds 20 μm. The bias in cloud optical thickness caused by using an inappropriate D_e is discussed in section 4.4. The collected D_e is used in cooperation with the MISR NIR band reflectance of MIL2TCAL and the simulated $R_{0.866}$ to derive $\tau_{0.866}$ for each MISR viewing geometry.

4.4 MODIS retrieval dependence of cloud optical thicknesses retrieved by MISR

The MODIS-retrieved cloud optical thicknesses are subject to uncertainties independent of the MODIS retrieval. As discussed in Section 4.3, cloud optical

thicknesses and effective particle sizes are retrieved using cloud reflectances at visible and near-infrared wavelengths. In the retrieval of τ, the derived cloud particle sizes are employed to match the model and observed reflectances. On the other hand, the retrieved cloud optical thicknesses can be used to compute the MODIS 2.13-μm reflectance to enhance the retrieval of D_e. This process can be applied iteratively to improve both the τ and D_e retrievals until the simulated cloud reflectances match the satellite observations. Therefore, biases in τ may be present when only the MISR NIR band reflectances are used in the retrievals.

To illustrate such errors, Fig. 4.11a plots the lookup table reflectances for the MODIS band 7 (black lines) and the MISR NIR band (red lines) for the HC model for two relative azimuth angles, 85° (Fig. 4.11a) and 177.5° (Fig. 4.11b) where μ_0 and μ are both set to be 0.85. The red curves (MISR NIR reflectances) were computed using D_e=50 μm. In Fig. 4.11a, the retrieved cloud optical thicknesses are slightly overestimated when De < 50 μm. For clouds consisting of larger ice crystals, the retrieved cloud optical thicknesses with MISR NIR band reflectances are significantly underestimated. The bias caused by the absence of the MODIS band 7 reflectances varies with the ice cloud models and solar and satellite viewing geometries of the lookup tables. The lookup table reflectances plotted in Fig. 4.11b reveal that the errors in the cloud optical thicknesses using MISR data with D_e=50 μm are more extreme when retrieved near the backscattering direction.

Figure 4.12 shows the relative errors in retrieved cloud optical thickness (RE_τ), using the six ice cloud models with D_e=50 μm. These errors are defined as

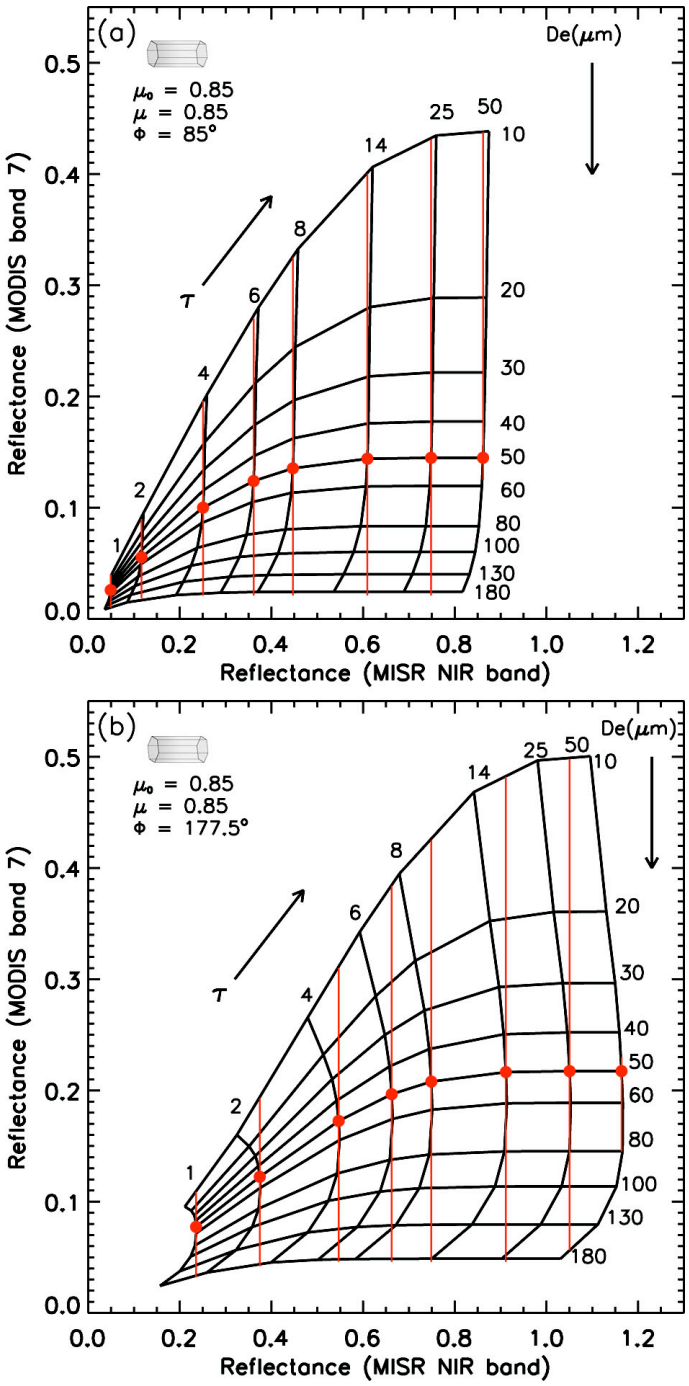

Fig. 4.11 MODIS band 7 and MISR NIR band reflectances (black) for variable particle size and optical thickness and MISR NIR band reflectances (red) for D_e = 50 μm. All calculations performed for the HC model at $\mu_o = \mu = 0.85$, and ϕ = (a) 85°, (b) 177.5°.

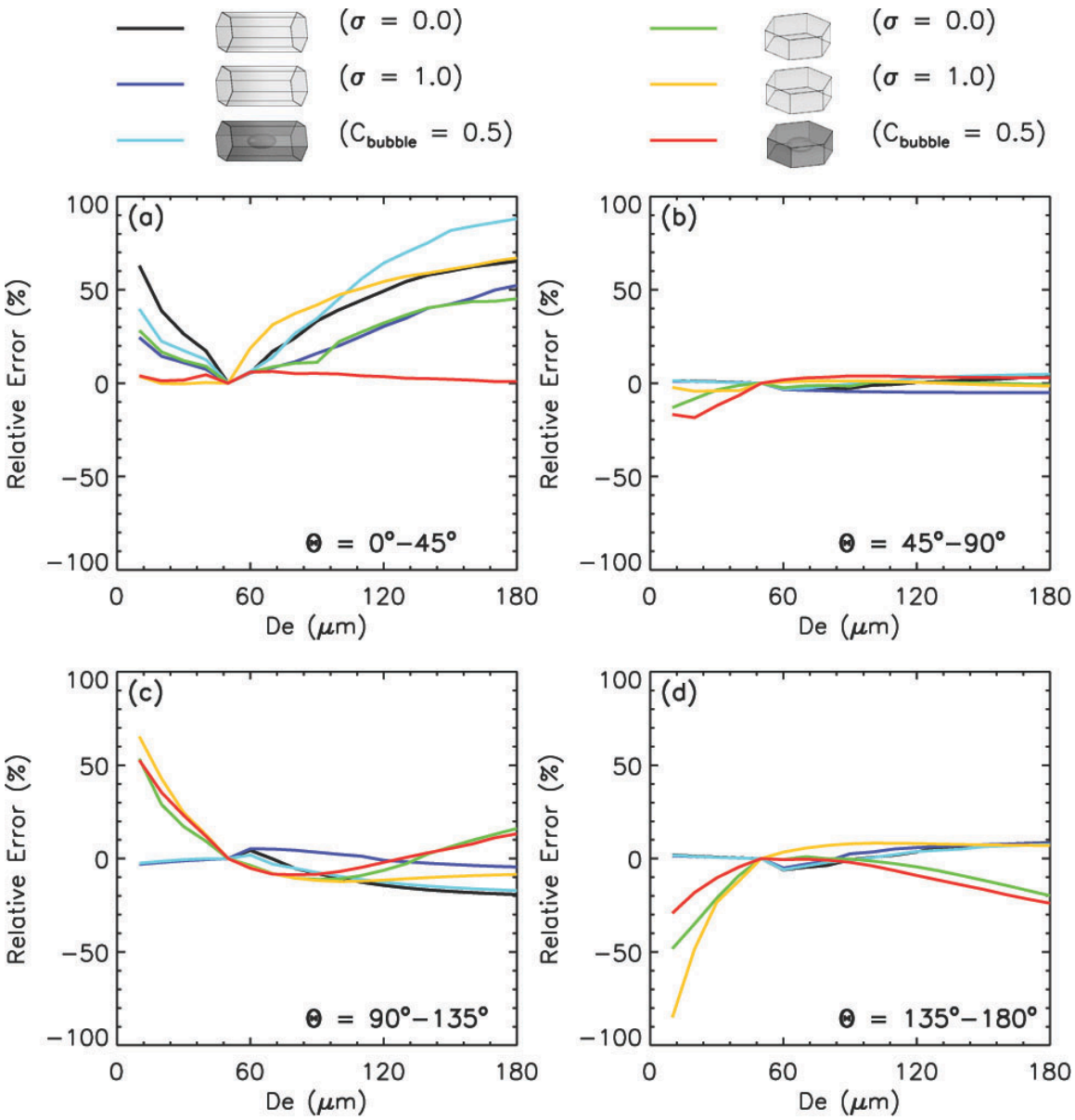

Fig. 4.12 Relative errors in τ using HC, RC, IC, HP, RP, and IP models with D_e = 50 μm and Θ = (a) 0°-45°, (b) 45°-90°, (c) 90°-135°, and (d) 135°-180°.

$$RE_{\tau} = \frac{1}{N_{\tau}} \sum_{i=1}^{N_{\tau}} \frac{\tau_{MISR,i} - \tau_i}{\tau_i} \times 100\%, \tag{4.22}$$

where τ_i is the cloud optical thickness used to simulate the MODIS band 7 and MISR NIR band reflectances, $\tau_{MISR,i}$ is the optical thickness retrieved using the lookup table of MISR NIR band reflectances, and N_τ is the total number of τ_i for each D_e. Figure 4.12a-4.12d show RE_τ averaged over the scattering angles Θ ranges, 0°-45°, 45°-90°, 90°-135°, and 135°-180°, respectively. In the region of forward scattering (see Fig. 4.12a), RE_τ is most sensitive to ice crystal habit and size. Fortunately, reflectances at Θ=0°-45° are infrequently used in satellite-based remote sensing. The RE_τ at Θ=45°-90° is within ±10% for most of the models and particle sizes. For Θ=90°-135°, the RE_τ values for the column models are nearly 0% for $D_e < 60$ μm and reach -20% for the largest crystals. The RE_τ values for the plate models in Fig. 4.12c are positive for D_e=0-50 and 120-180 μm, indicating an overestimate of τ for such clouds. For D_e=50-120 μm, RE_τ is slightly smaller than 0. In the region of back scattering (Fig. 4.12d), RE_τ for the column models is negligible. However, the optical thicknesses of plates are significantly underestimated when D_e=50 μm is used in the retrieval.

From the results shown in Figs. 4.11 and 4.12, the average RE_τ for the column models are within ±10% for the scattering angles related to satellite-base remote sensing. For plates, using an estimated cloud particle size may lead to substantial errors, especially for ice clouds with extremely small or large sizes. Thus, employing the MODIS retrieval of ice cloud effective particle sizes can efficiently remove the MISR retrieval biases that would otherwise result from the assumption of a constant particle size in the retrievals.

4.5 Results

Based on the algorithm described in section 4.3, τ is retrieved for the 9 MISR viewing geometries for the matched MODIS and MISR pixels. The difference between the cloud optical thicknesses from the 9 viewing angles and its average can be used to evaluate the accuracy of the retrieval. With the presence of other uncertainties in the retrieval of ice cloud optical properties, the most appropriate ice cloud model will give the smallest optical thickness differences (OTDs) values and RMS ε of optical thickness and is formulated as,

$$OTD_{i,j} = \frac{\tau_{i,j} - < \tau_i >_j}{< \tau_i >_j} \tag{4.23}$$

$$\varepsilon = \sqrt{\frac{1}{9N_P} \sum_{j=1}^{N_P} \sum_{i=1}^{9} OTD_{i,j}^2}\,, \tag{4.24}$$

where $\tau_{i,j}$ is the retrieved ice cloud optical thickness for each available MISR pixel, $<\tau_i>_j$ is the averaged value of $\tau_{i,j}$ over the 9 MISR viewing geometries, and N_P is the number of available MISR pixels.

4.5.1 Errors in retrieved optical thickness for matched MODIS and MISR granules pixels

Table 4.1 lists the values ε for the matched MODIS and MISR data from the granules shown in Fig. 4.6 and those over central Pacific Ocean on 19 February 2010 at 21:40 UTC (the MODIS RGB image of radiances is shown in Fig. 4.13; and the thermodynamic phases of the clouds and the retrieved ice cloud effective particle sizes are displayed in Fig. 4.14.). For the retrievals using data from the granule in Fig. 4.6, the smallest error is clearly that for the RC model. The IP model yields the best performance

Table 4.1. RMS, ε, of ice cloud optical thickness retrieved from matched MODIS and MISR data for one 5-miute MODIS granule using 6 different models.

Ice cloud model	2050 UTC, 2 July 2009	2140 UTC, 2 July 2009
HC	0.245	0.198
RC	0.176	0.168
IC	0.256	0.195
HP	0.2576	0.163
RP	0.2376	0.166
IP	0.2446	0.155

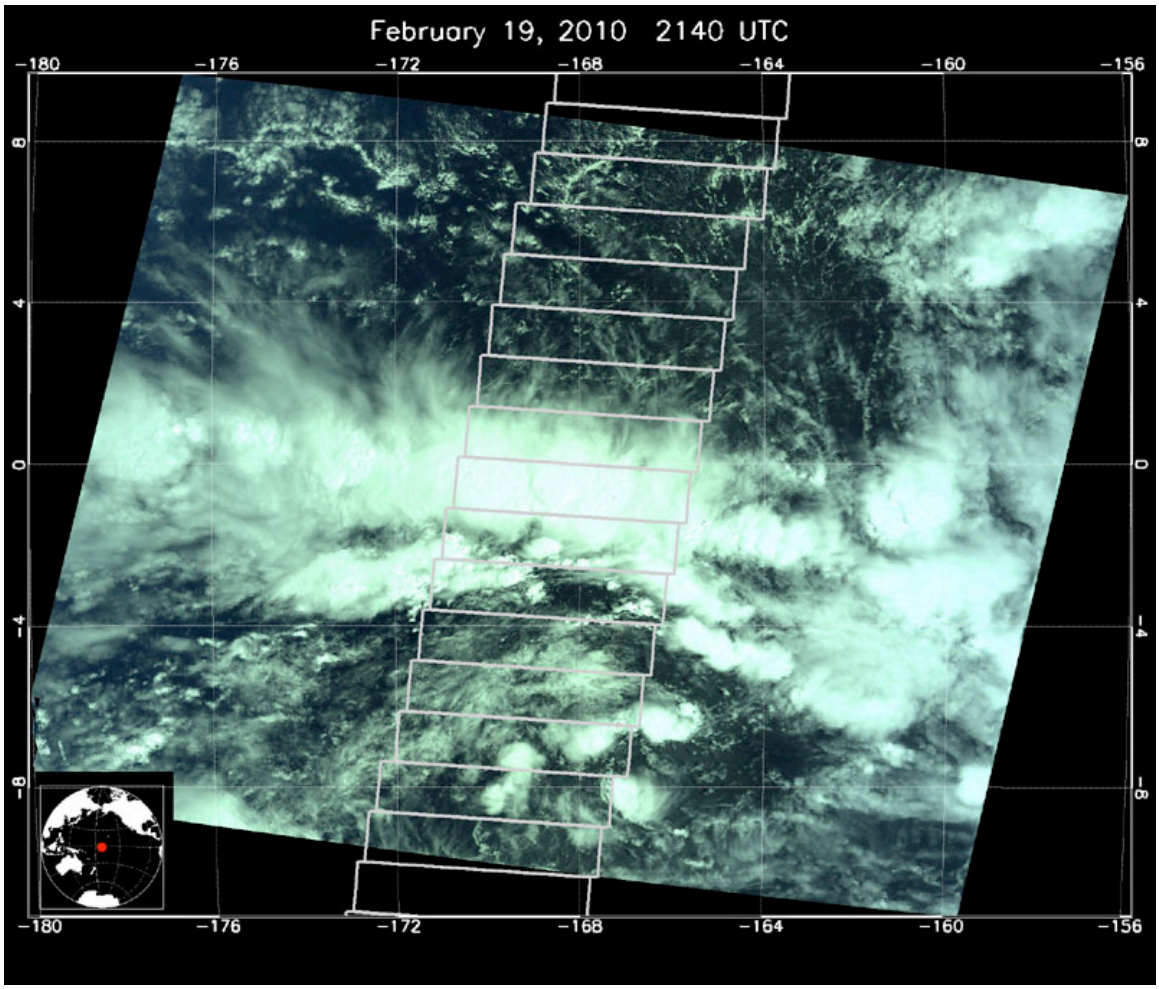

Fig. 4.13 Same as Fig. 4.6, except for 2140 UTC, 19 February 2010. The white boxes indicate blocks 83 through 100 of MISR Path 68.

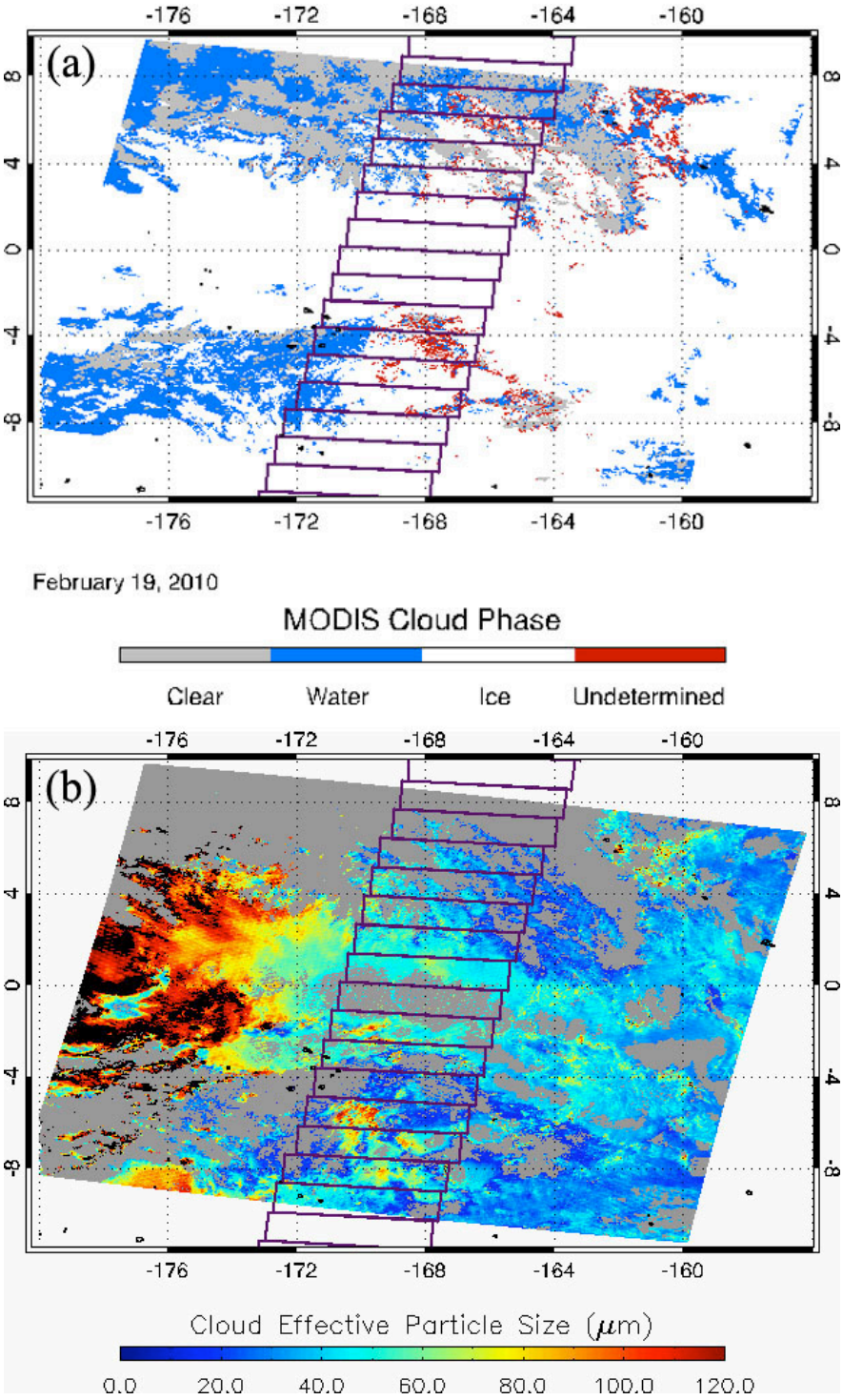

Fig. 4.14 Cloud properties determined from radiances corresponding to image in Fig. 4.13. (a) Thermodynamic phase, (b) Ice cloud effective particle sizes derived using HC ice cloud model.

in retrieving τ for the 19 February case. However, the retrieval errors for the HP, RP, and RC models are not much greater than the IP minimum. Because of the natural variability of the cloud particle habits, the differences between the 2 July and 19 February results is not surprising.

Figure 4.15 shows the histograms of D_e and τ retrieved using the HC model for the matched MODIS and MISR data for the granules taken 2 July 2009 and 19 February 2010 as shown in Figs. 4.6 and 4.13, respectively. The distributions of D_e and τ for the data in Fig. 4.6 are centered at around 70 μm and 15, respectively. For the retrievals using data from 19 February 2010, the particle sizes of the clouds are slightly smaller than 70 μm and the maximum optical depth occurs around τ=3.

Because the RC model error is small for both days and has the least error for both days combined, it would be the most appropriate model overall for these two cases. Although the IP model has lowest error for the 19 February case, its overall error is ~19% larger than that for the RC model. Since the IP model is the most appropriate one for the 19 February case and the retrieved optical depths are, on average, considerably less than those retrieved for the 2 July case, it would appear that the IP or any of the plate models would be best for optically thin clouds. However, the RC model error is only 8% greater than ε(IP) for that case. Thus, the use of plates to optimally retrieve τ for optically thin clouds is somewhat ambiguous. Further classification of the errors according to optical depth range would be required to determine if the model errors vary with τ.

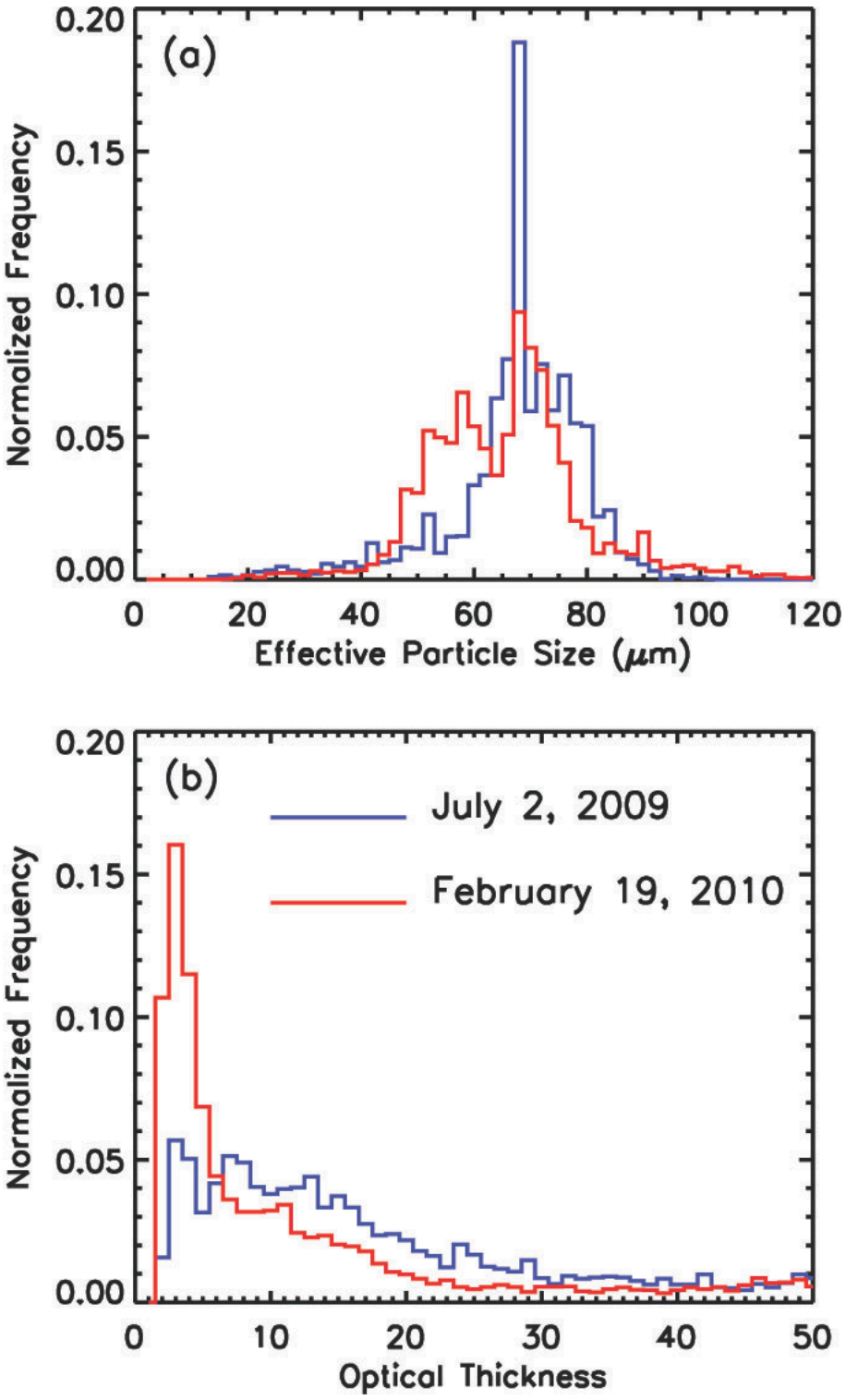

Fig. 4.15 Histograms of the ice cloud (a) effective particle size and (b) optical thickness retrieved using the HC model for the matched MODIS and MISR data shown in Figs. 4.6 and 4.13.

4.5.2 Examination of ice cloud models using 1-day of matched MODIS and MISR data

To further examine the potential of finding an ice cloud model that produces the least biased retrievals of ice cloud properties, models containing various mixtures of the six hexagonal and plate models are tested using MODIS and MISR data on a global scale. Following the results above using the two granules of matched MODIS and MISR data, RC data are assumed to be the major component for the habit mixtures. The habit fractions of the ice crystals in the ice cloud models are specified as follows:

$$C_{RC} = 0.4 + 0.6\xi_1 \,, \tag{4.25}$$

$$C_{HC} = \frac{(1 - C_{RC})\xi_2}{\xi_2 + \xi_3 + \xi_4 + \xi_5 + \xi_6} \,, \tag{4.26}$$

$$C_{IC} = \frac{(1 - C_{RC})\xi_3}{\xi_2 + \xi_3 + \xi_4 + \xi_5 + \xi_6} \,, \tag{4.27}$$

$$C_{HP} = \frac{(1 - C_{RC})\xi_4}{\xi_2 + \xi_3 + \xi_4 + \xi_5 + \xi_6} \,, \tag{4.28}$$

$$C_{RP} = \frac{(1 - C_{RC})\xi_5}{\xi_2 + \xi_3 + \xi_4 + \xi_5 + \xi_6} \,, \tag{4.29}$$

$$C_{IP} = \frac{(1 - C_{RC})\xi_6}{\xi_2 + \xi_3 + \xi_4 + \xi_5 + \xi_6} \,, \tag{4.30}$$

where ξ_1, ξ_2, ξ_3, ξ_4, ξ_5, and ξ_6 are independent random numbers uniformly distributed in [0, 1].

Two hundred sets of habit fractions were initially examined using the two cases represented in Figs. 4.6 and 4.13. Table 4.2 lists the habit mixture models having the minimum τ RMS errors for C_{RC} varying within the fractional intervals, (0.4, 0.5), (0.5, 0.6), (0.6, 0.7), (0.7, 0.8), (0.8, 0.9), and (0.9, 1.0). The RMS errors of cloud optical thickness generally decrease with increasing C_{RC}, which is associated with the overall

Table 4.2. Ice cloud models and standard deviations of cloud optical thickness for the MODIS and MISR granules on 2 July 2009 and 19 February 2010.

			$0.9<C_{RC}<1.0$				
Ice cloud model	C_{HC}	C_{RC}	C_{IC}	C_{HP}	C_{RP}	C_{IP}	ε
M1	0.0001	0.9974	0.0014	0.0009	0.0002	0.000	0.171
M2	0.0023	0.9828	0.0034	0.0067	0.0003	0.0045	0.171
			$0.8<C_{RC}<0.9$				
M3	0.0423	0.8913	0.0004	0.0115	0.0063	0.0482	0.171
M4	0.0004	0.8848	0.0115	0.0063	0.0485	0.0485	0.172
			$0.7<C_{RC}<0.8$				
M5	0.0353	0.7963	0.0390	0.0598	0.0158	0.0538	0.172
M6	0.0270	0.7875	0.0584	0.0723	0.0045	0.0503	0.172
			$0.6<C_{RC}<0.7$				
M7	0.0589	0.6987	0.0361	0.0710	0.0374	0.0979	0.173
M8	0.0068	0.6817	0.0759	0.0807	0.0228	0.1321	0.173
			$0.5<C_{RC}<0.6$				
M9	0.0701	0.5217	0.0191	0.0779	0.1609	0.1503	0.174
M10	0.0190	0.5389	0.0775	0.1602	0.1495	0.0549	0.174
			$0.4<C_{RC}<0.5$				
M11	0.0091	0.4818	0.0066	0.0254	0.2528	0.2243	0.174
M12	0.0057	0.4026	0.0221	0.2196	0.1948	0.1552	0.174

good error (~0.172) of the RC model for the two cases combined. Including some fraction of other habits in the mixture only reduces the minimum 2-case error by 0.6% (models M1 and M2) compared to the pure RC model.

Among the ice cloud models in this study, those consisting of a single ice crystal habit and M1, M3, M5, M7, M9, and M11 are further tested using all daytime matched MODIS and MISR data taken over ocean on 2 July 2009. A total of 129 MODIS granules and 15 MISR paths are involved. Figure 4.16 shows the histograms of D_e and τ retrieved using the HC model applied to the global 2 July dataset. Compared to Fig. 4.15a, the distribution of the cloud particle sizes in Fig. 4.16a is populated with ice particles covering a broad range with a peak at 60 μm. For the retrieved cloud optical thickness, the peak of the distribution occurs near 4, with ~50% of the population having $\tau<15$. The retrieved ice cloud properties in Fig. 4.16 are based on 244611 2.2 km MISR pixels, which indicates that more than 100 and 2000 retrievals contribute to any interval displayed in Figs. 4.16a and 4.16b, respectively. The large number of samples from all over the globe confirm that the results for this 1-day dataset are much more representative of ice clouds over the global than the two cases shown in Figs. 4.6 and 4.13.

Figure 4.17 compares the ice cloud optical thicknesses derived using MISR measurements at 9 different viewing angles. The retrievals of τ for Fig. 4.17 were obtained using the RC model. The optical thickness for each MISR viewing angle, $<\tau>_i$, is specified by

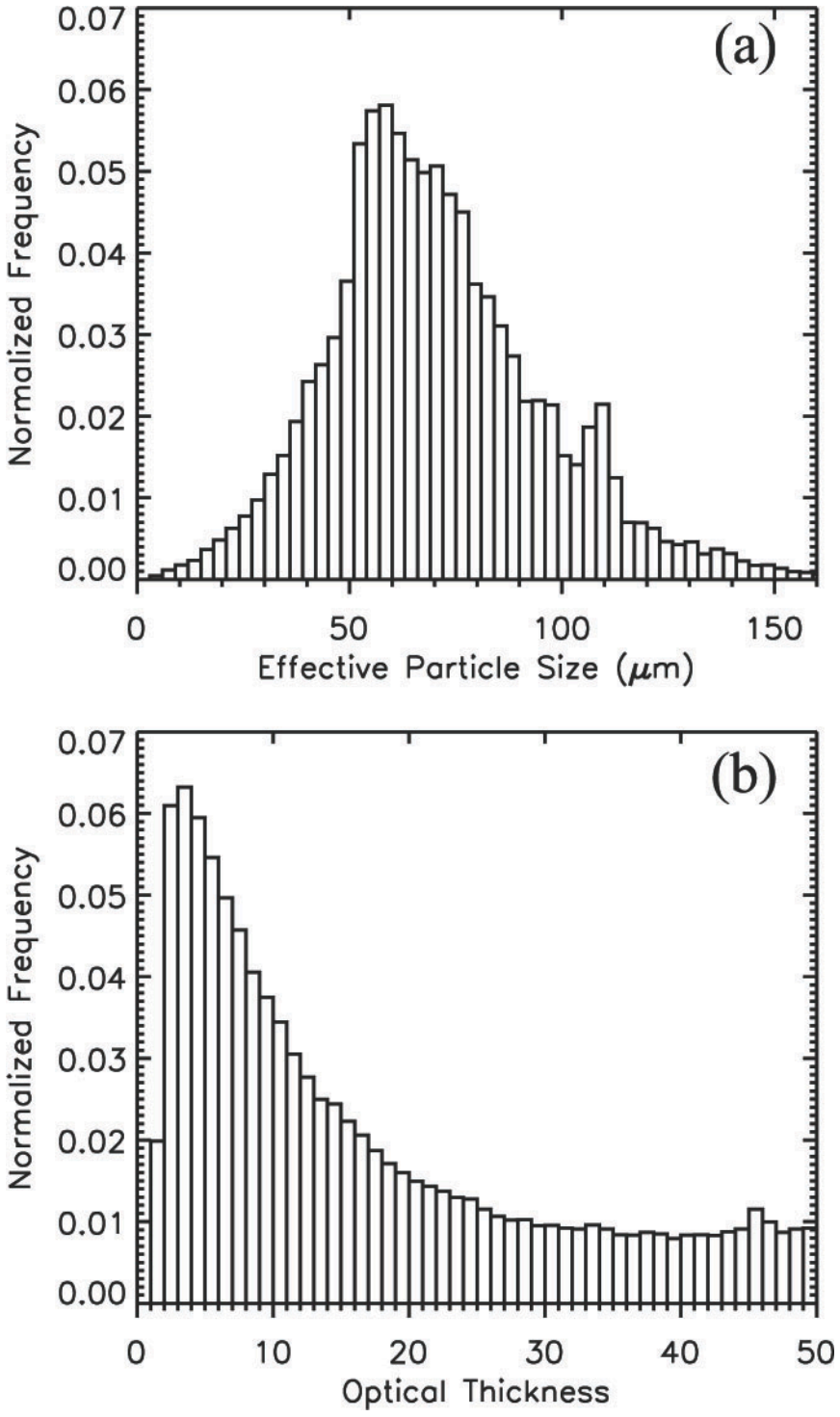

Fig. 4.16 Same as Fig. 4.15, except for 1 day of data taken over ocean, 2 July 2009.

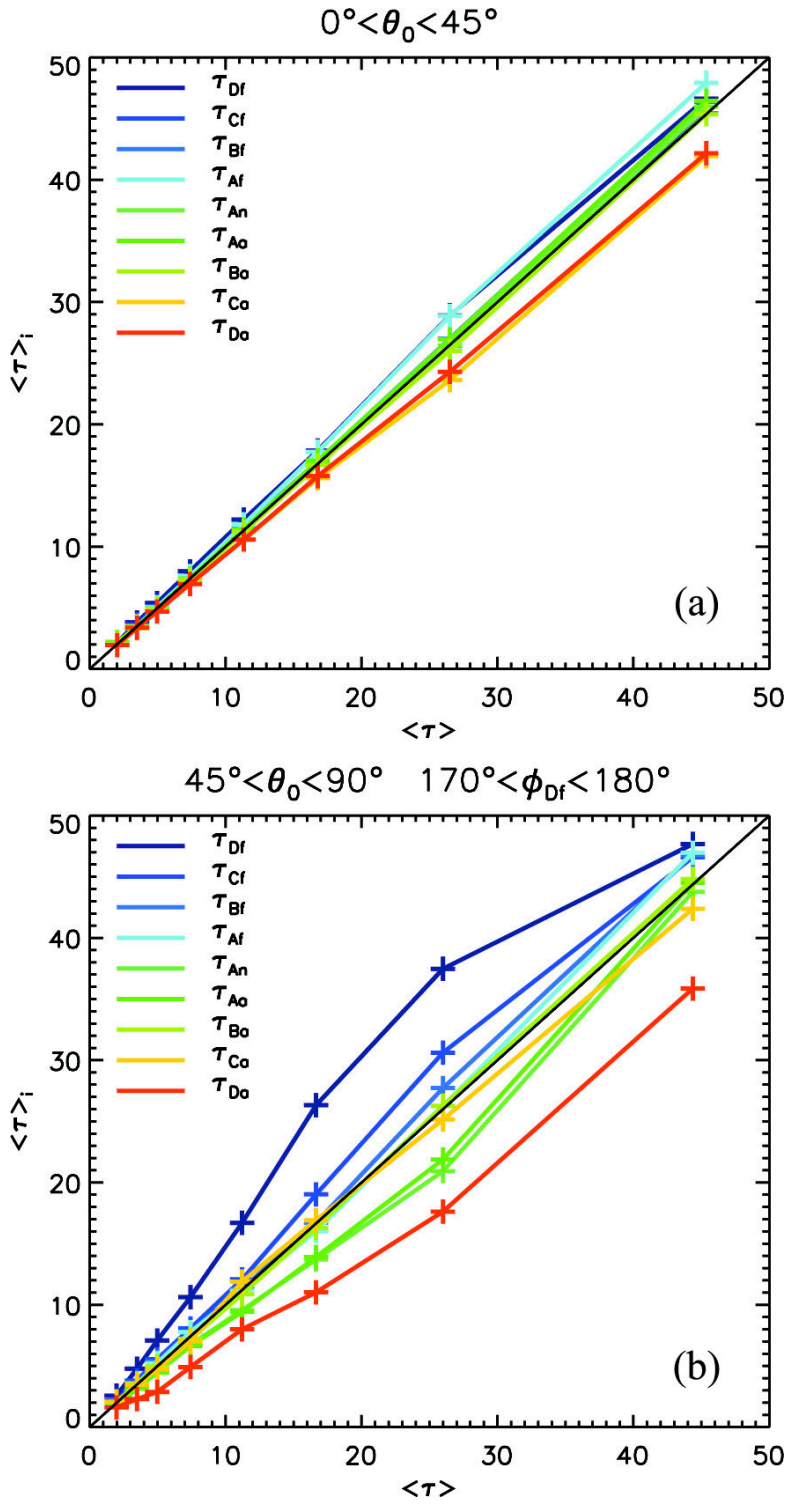

Fig. 4.17 (a) Average ice cloud optical thicknesses retrieved for each of the 9 MISR cameras using the RC model for 1 day of matched MODIS and MISR data taken over ocean, 2 July 2009. (a) $0° < \theta_0 < 45°$; (b) $45° < \theta_0 < 90°$ and $170° < \phi < 180°$.

$$\langle\tau\rangle_i = \begin{cases} \dfrac{1}{N_{P1}}\sum_{j=1}^{N_{P1}}\tau_{i,j} & for \quad \langle\tau\rangle \le 1 \\ \dfrac{1}{N_{P2}}\sum_{j=1}^{N_{P2}}\tau_{i,j} & for \quad 1 < \langle\tau\rangle \le 2 \\ \dfrac{1}{N_{P3}}\sum_{j=1}^{N_{P3}}\tau_{i,j} & for \quad 2 < \langle\tau\rangle \le 3 \\ \dfrac{1}{N_{P4}}\sum_{j=1}^{N_{P4}}\tau_{i,j} & for \quad 3 < \langle\tau\rangle \le 4 \\ \dfrac{1}{N_{P5}}\sum_{j=1}^{N_{P5}}\tau_{i,j} & for \quad 4 < \langle\tau\rangle \le 7 \\ \dfrac{1}{N_{P6}}\sum_{j=1}^{N_{P6}}\tau_{i,j} & for \quad 7 < \langle\tau\rangle \le 15 \\ \dfrac{1}{N_{P7}}\sum_{j=1}^{N_{P7}}\tau_{i,j} & for \quad 15 < \langle\tau\rangle \le 30 \\ \dfrac{1}{N_{P8}}\sum_{j=1}^{N_{P8}}\tau_{i,j} & for \quad 30 < \langle\tau\rangle \end{cases}, \tag{4.31}$$

where $<\tau>$ is the averaged value of $<\tau>_i$ over the 9 MISR viewing angles; and N_{P1}, N_{P2}, N_{P3}, N_{P4}, N_{P5}, N_{P6}, N_{P7}, and N_{P8} are the numbers of MISR pixels for each interval of $<\tau>$. At $0° < \theta_0 < 45°$, the retrieved τ is slightly dependent on satellite viewing geometries, particularly when $<\tau> < 10$ (see Fig. 4.17a). The agreement between the retrievals developed at small solar zenith angles is related to the phase function being less sensitive to ice cloud models in the backscattering directions. For $45° < \theta_0 < 90°$ and the relative azimuth angle ϕ_{Df} of the MISR Df camera between 170° and 180°, retrievals developed

over small viewing angles agree more with $<\tau>$, while the retrieved ice cloud optical thicknesses tend to be overestimated and underestimated fore and aft of the local vertical directions (see Fig. 4.17b). The effect can be explained by cloud side illumination and shadowing by 3D clouds [*Davies*, 1984; *Iwabuchi and Hayasaka*, 2002; *Loeb and Davies*, 1997; *Loeb and Coakley*, 1998].

Figure 4.18 shows the normalized densities of ice cloud OTDs as functions of Θ retrieved using a water cloud model (Fig. 18a) and the HC model (Fig. 4.18b) for 263657 and 244611 MISR pixels, respectively. Mie theory [*Wiscombe*, 1977] was employed to compute the scattering properties of water cloud particles whose refractive indices are $1.3244 + i3.58\times10^{-7}$ and $1.2901 + i3.94\times10^{-4}$ for λ=0.866 μm and λ=2.13 μm, respectively. Generally, the RMS values of the normalized OTDs in Fig. 4.18 are much larger than those derived for the two granules examined earlier (see Tables 4.1 and 4.2) because population of optically thick clouds is larger for the global dataset. The ε resulting from retrievals based on the water cloud model is significantly larger than that from using the ice cloud model. In addition, compared to Fig. 4.18a, the OTDs derived using the HC model are more symmetrical around a zero-bias line. These results confirm that the water cloud model is not appropriate for retrieving ice cloud optical properties, a conclusion reached from other types of analyses (e.g., *Minnis et al.*[1993]; *Doutriaux-Boucher et al.* [2000]).

Figures 4.19 and 4.20 show the normalized densities of ice cloud OTDs retrieved using the HC, RC, and IC models as functions of Θ. The OTDs for the RC model are smaller and more symmetrical around the zero-bias line than the other two models. It is

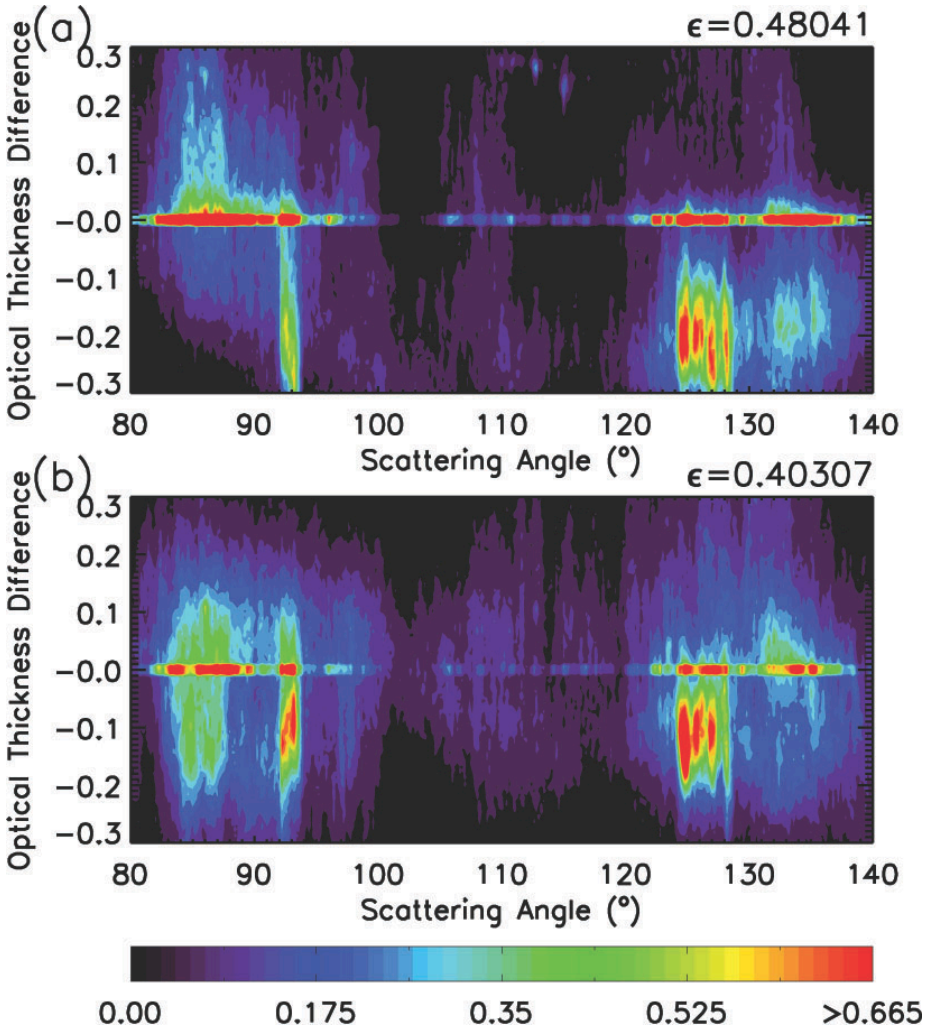

Fig. 4.18 Normalized densities of ice cloud optical thickness differences using (a) water cloud model and (b) HC model for 1 day of matched MODIS and MISR data taken over ocean, 2 July 2009.

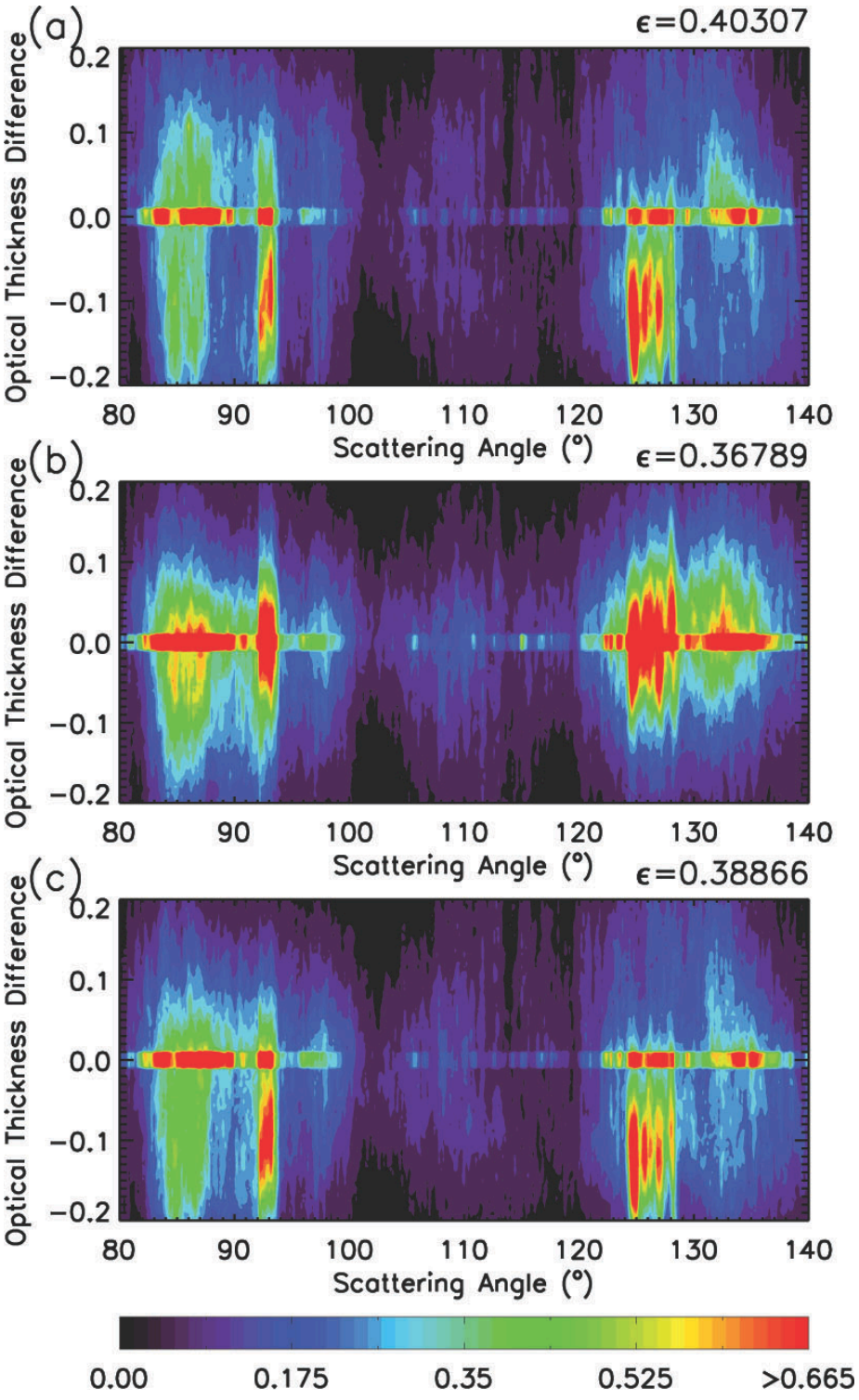

Fig. 4.19 Same as Fig. 4.18, except using (a) HC, (b) RC, and (c) IC models.

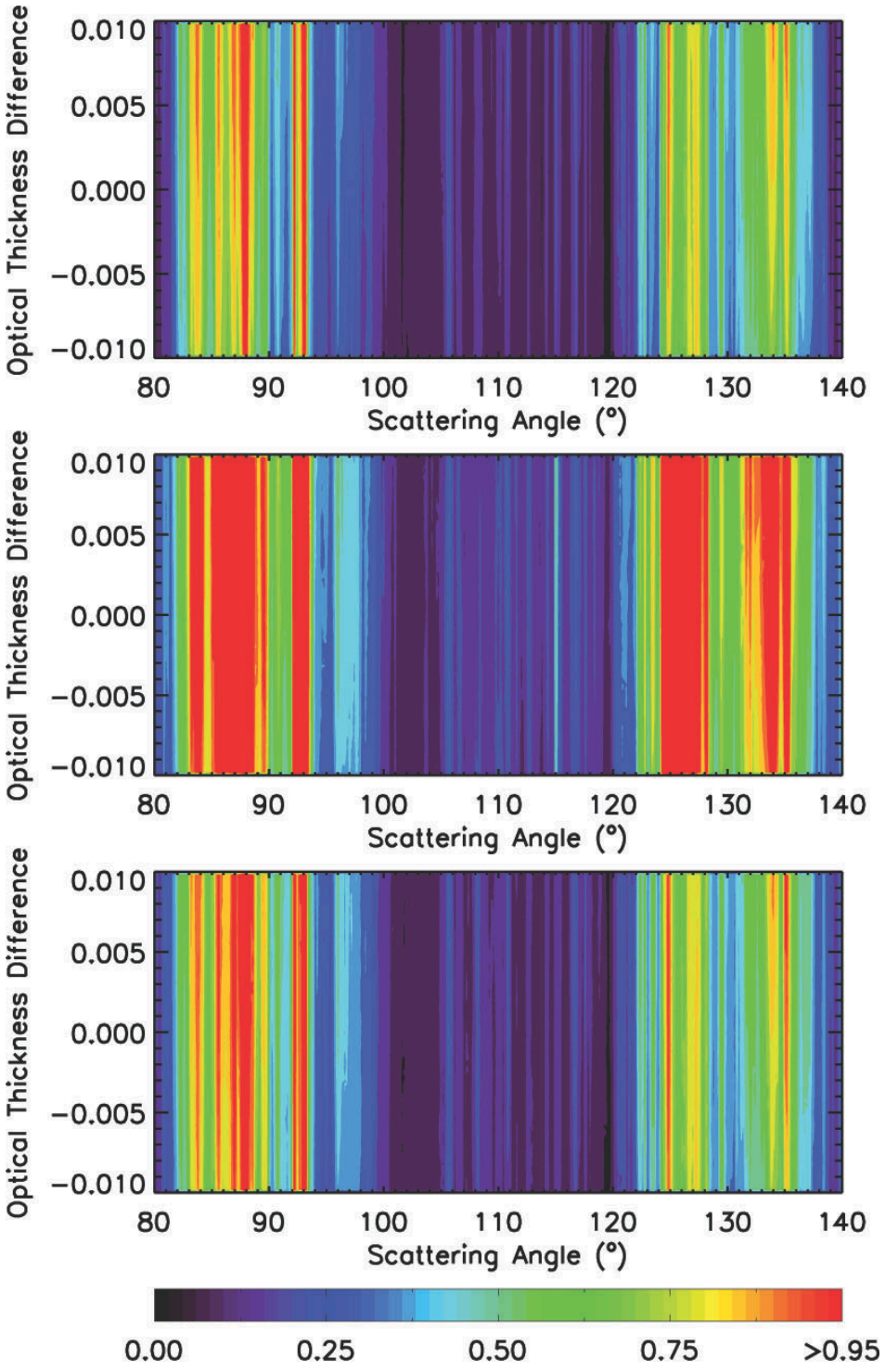

Fig. 4.20 Same as Fig. 4.19, except only for normalized OTDs between -0.01 and 0.01.

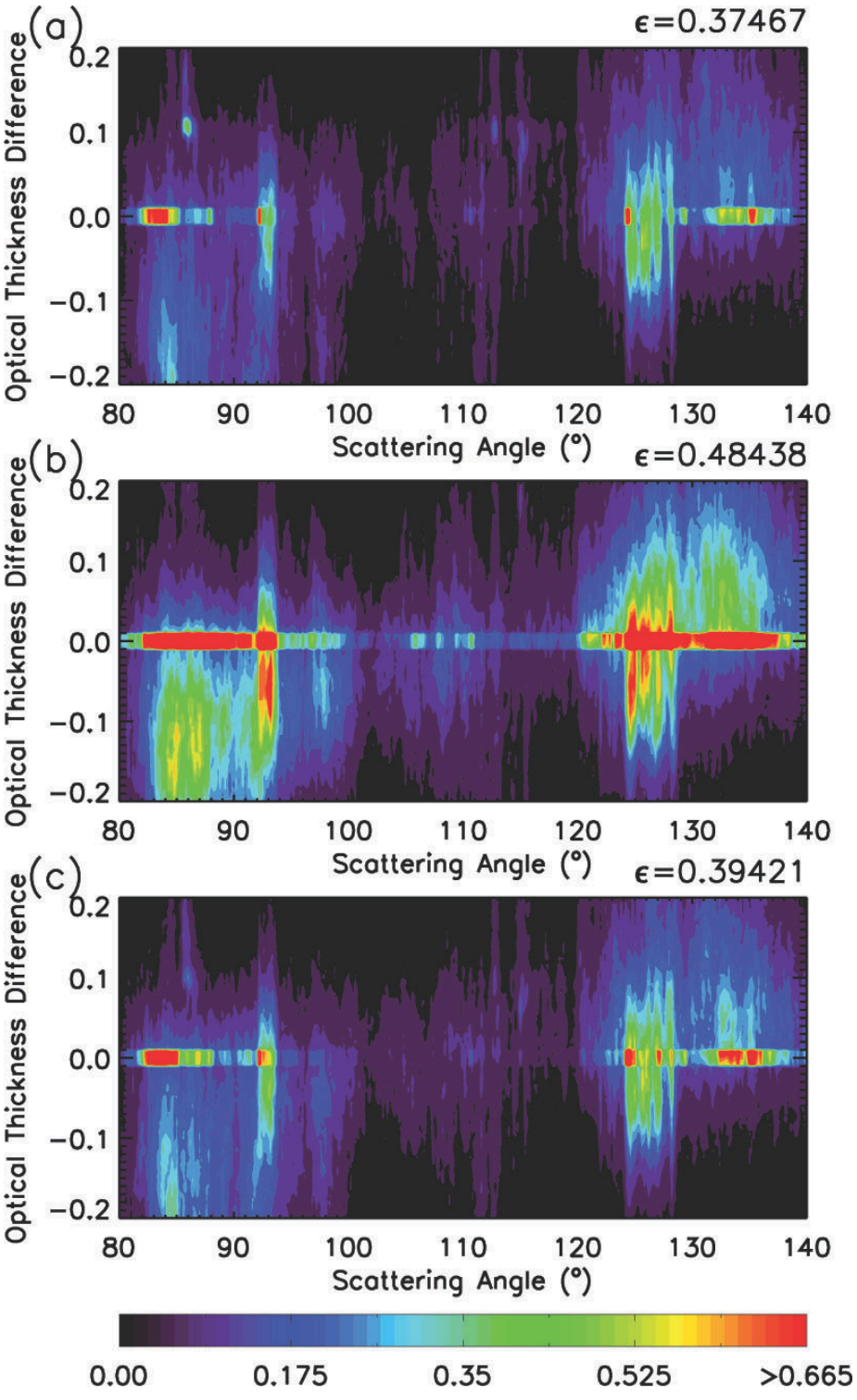

Fig. 4.21 Same as Fig. 4.19, except for using (a) HP, (b) RP, and (c) IP models.

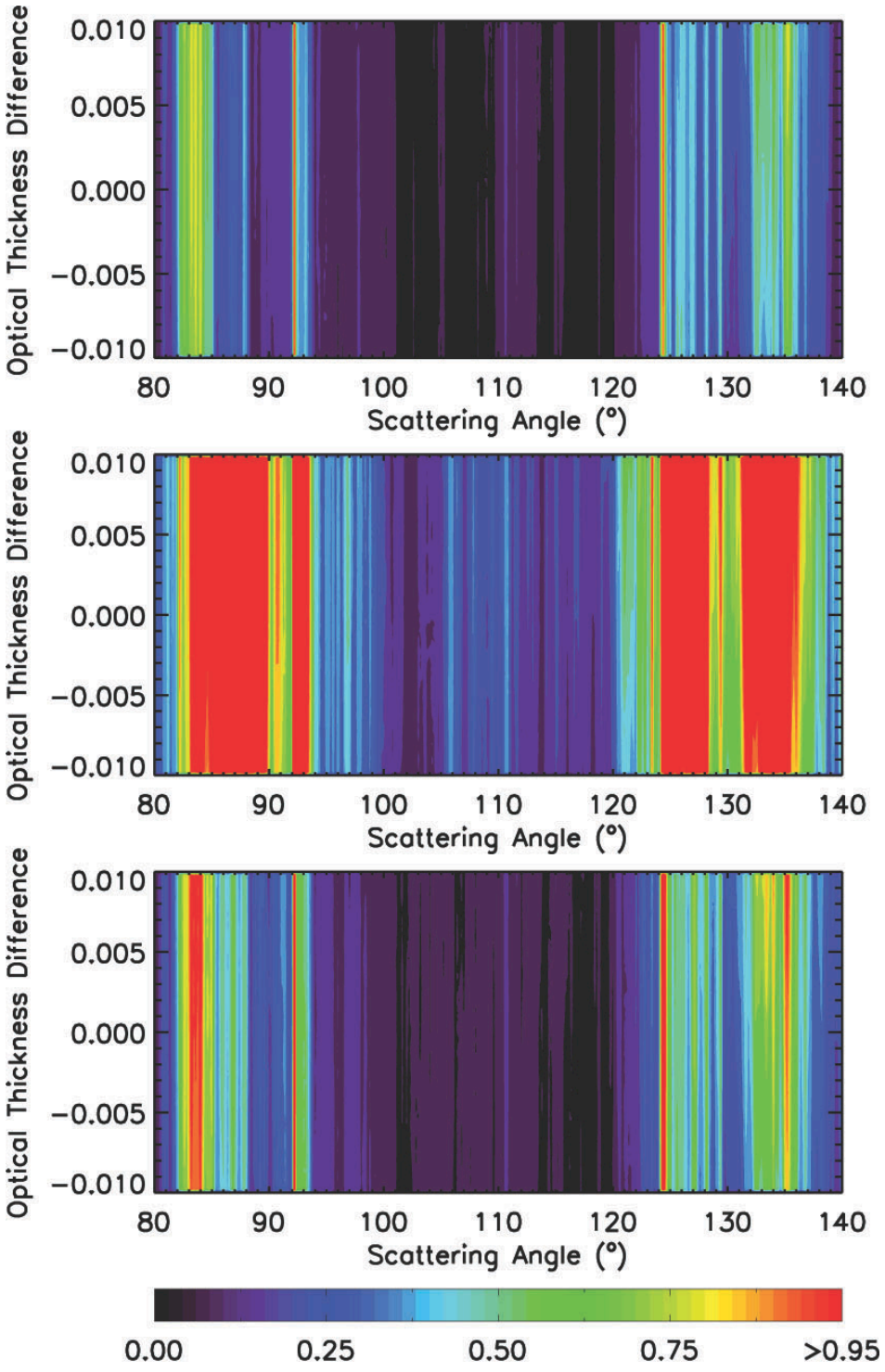

Fig. 4.22 Same as Fig. 4.21, except only for normalized OTDs between -0.01 and 0.01.

evident from the close up plot in Fig. 4.20 that more MISR retrievals using the RC scattering properties are associated with OTDs in the range of -0.01 to 0.01.

Figures 4.21 and 4.22 show the normalized densities of ice cloud OTDs using the HP, RP, and IP models as functions of Θ. Compared to the results in Fig. 4.19, fewer valid retrievals were obtained using the plate models. None of the plate models yield the degree of OTD symmetry about the zero bias that was found for the RC model retrievals. Overall, among the six ice crystal habits used for the results in Figs. 4.19-4.22, the RC model yields the least angular dependence of the τ retrieval on viewing angle. This is consistent with the initial test of ice cloud models using the two MODIS granules.

Table 4.3 lists the average standard deviation of retrieved τ for all of the ice cloud models tested using the 1-day MODIS-MISR dataset. The smallest value of ε, 0.365, is found for the M3 model. Figure 4.23a shows that the normalized densities of M3 OTD produce a pattern similar to that found using the RC model (Fig. 4.19b). Figures 4.23b and 4.23c display the OTD frequency differences between the M3 and HC results and the M3 and RC results as functions of Θ. The OTD distribution from M3 is quite different from that for the HC retrievals. Conversely, the M3 and RC distributions are very similar as indicated by the frequent occurrence of small differences in Fig. 4.23c. From the comparison of OTDs between the M3 and RC results and their small differences in ε from Table 4.3, it can be concluded that the M3 is minimally better at retrieving an angularly consistent τ. The asymmetry factors, g, of the ice cloud models are listed in Table 4.4. For D_e=50 μm, it can be found that g generally decreases when roughened surface and internal air bubbles are account for, which is consistent with the results reported by *Yang et al*. [2008b] and *Xie et al.* [2009]. At λ=0.866 and 2.13 μm, the ε does

Table 4.3. Ice cloud models and standard deviations of cloud optical thickness for the MODIS and MISR granules at a 1-day interval on 2 July 2009.

Ice cloud model	ε	Ice cloud model	ε
HC	0.403	M1	0.367
RC	0.368	M3	0.365
IC	0.389	M5	0.366
HP	0.375	M7	0.369
RP	0.484	M9	0.388
IP	0.394	M11	0.407

Table 4.4. Ice cloud models and their asymmetry factors for D_e=50 μm.

Ice cloud model	g (λ=0.866μm)	g (λ=2.13μm)
HC	0.7938	0.8452
RC	0.7820	0.8309
IC	0.7862	0.8389
HP	0.9172	0.9352
RP	0.8529	0.8906
IP	0.9104	0.9286
M1	0.7822	0.8310
M3	0.7868	0.8351
M5	0.7916	0.8392
M7	0.7971	0.8439
M9	0.8091	0.8537
M11	0.8159	0.8589

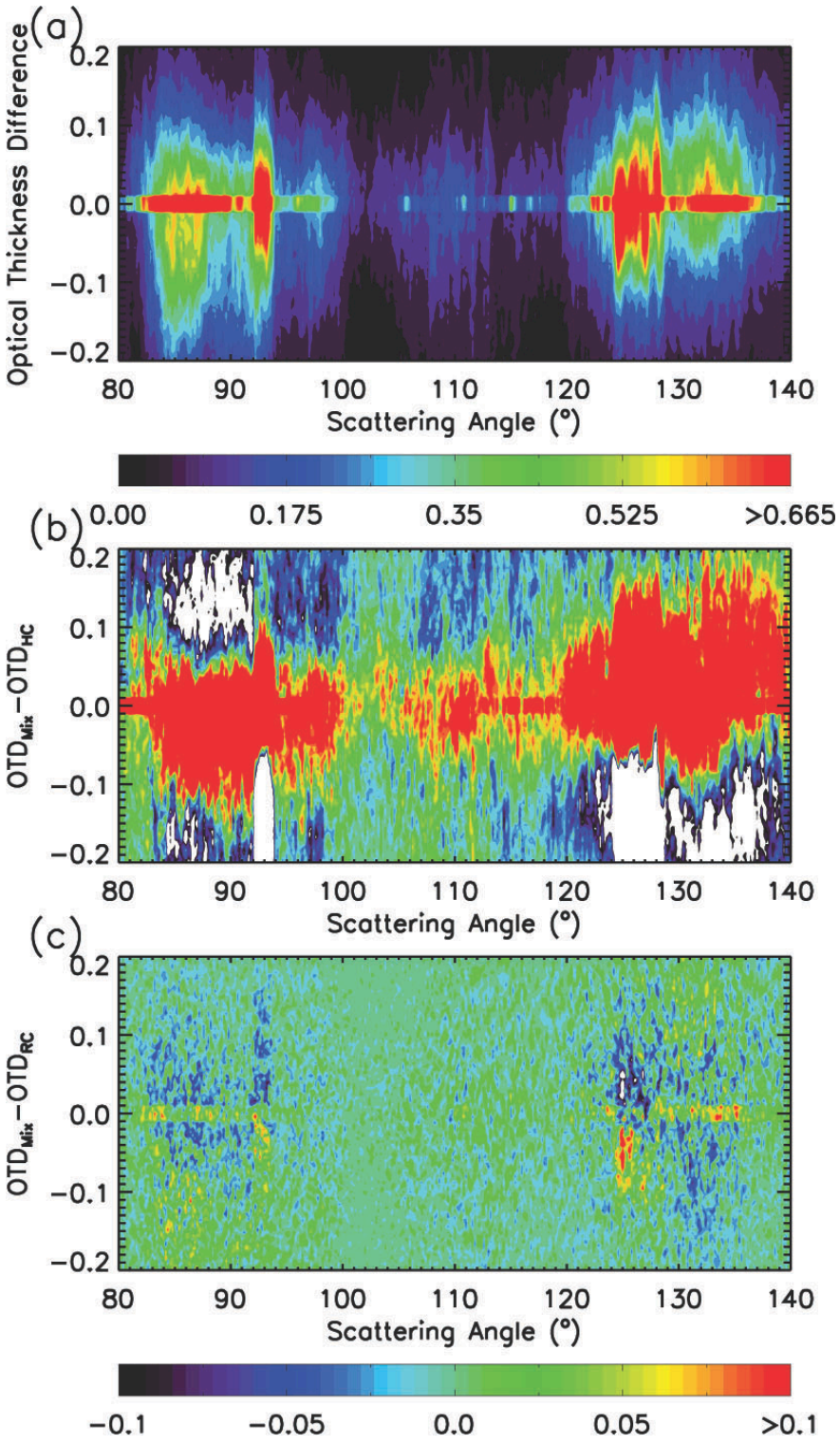

Fig. 4.23 (a) Normalized density of ice cloud optical thickness differences using the M3 model, (b) OTD_{Mix}-OTD_{HC} and (c) OTD_{Mix}-OTD_{RC} as functions of scattering angle for 1 day of matched MODIS and MISR data taken over ocean, 2 July 2009.

not have a linear relationship with g as evident by Tables 4.3 and 4.4. However, Ice cloud models with relatively small g normally have better performance in the retrieval of ice cloud properties.

Figure 4.24 replots the normalized densities of the M3 OTDs for two different ranges of $<\tau>$, 0-5 (Fig. 4.24a) and 5-20 (Fig. 4.24b). From Fig. 4.24, the M3 model performed well in retrieving ice cloud properties for both optically thin and thick clouds. Based on the comparison between the data in Fig. 4.24a and 4.24b, the OTDs of optically thin cirrus clouds are concentrated closer to 0. The greater errors for optically thick cirrus cloud retrievals may be, in part, due to a greater contribution of 3D effects [*Iwabuchi and Hayasaka*, 2002].

From these results, it can be concluded that among the tested ice crystal distributions, the M3 model is the best model for retrieving cloud optical thickness from solar reflectance measurements. However, its accuracy is only slightly better than that found for the simpler roughened hexagonal ice column model, RC, and three other habit-mixture models. All 5 represent significant improvements over the use of smooth hexagonal columns and plates, roughened plates, and inhomogeneous plates. The goal of this study was to determine the optimal model for simple shapes and combinations of those simple shapes. As noted earlier, many other habits and combinations of habits are possible and they may yield smaller dependencies of the retrieved τ on the viewing and illumination geometry. However, much additional study is required to examine the sensitivity of the retrieved optical thickness to more complex shapes and combinations.

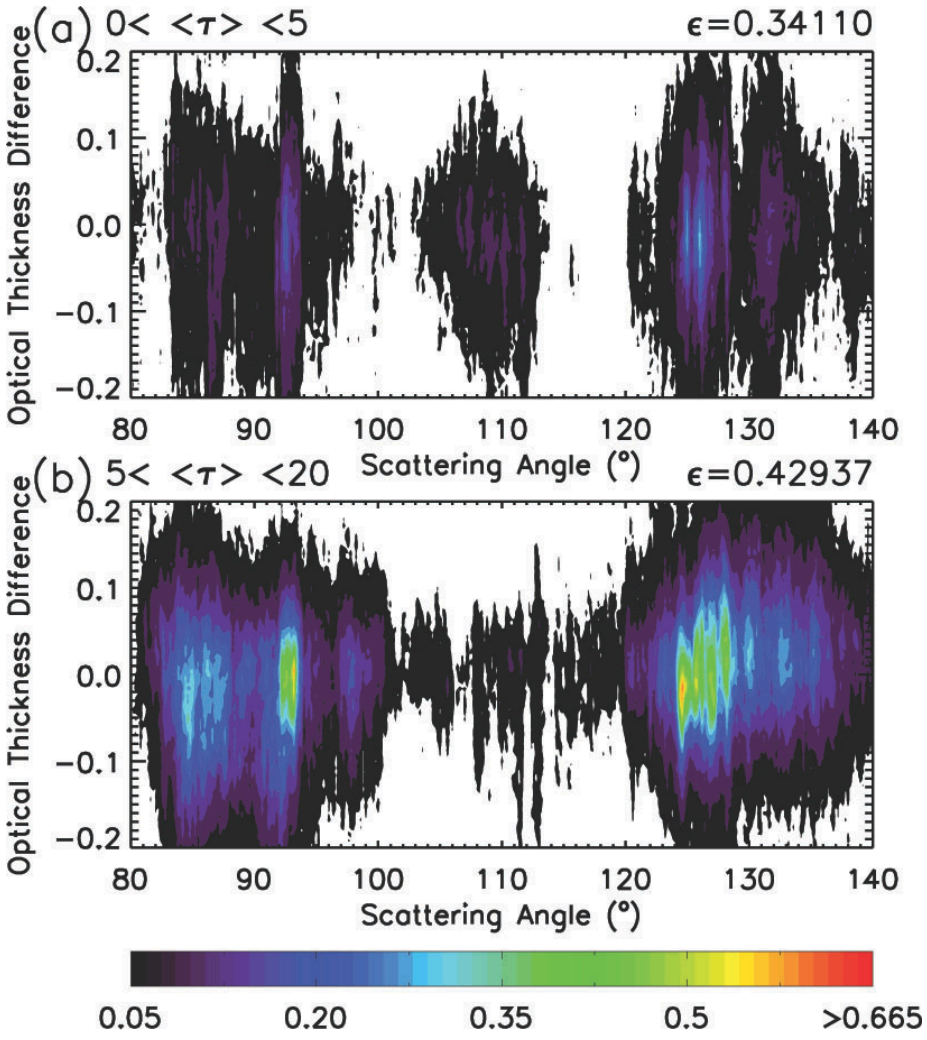

Fig. 4.24 Normalized density of ice cloud optical thickness differences using the M3 model (a) $0 < \langle\tau\rangle < 5$ and (b) $5 < \langle\tau\rangle < 20$.

4.6 Summary

In this study, we examined a broad range of ice cloud models that consist of smooth, roughened, homogeneous, and inhomogeneous hexagonal ice crystals with various aspect ratios. The sensitivity of cirrus bulk scattering properties and solar reflectances to these ice cloud models is investigated using the IGOM and DISORT models. At shortwave wavelengths, the smoothed scattering phase function is shown for ice cloud models with surface roughened or inhomogeneous ice crystals. It was also demonstrated that cloud bidirectional reflectance is sensitive to the particular ice cloud habit with the smoothest reflectance fields resulting from the use of severely roughened ice columns.

The MODIS cloud reflectances from bands 1 and 7, averaged over 1° × 1° latitude-longitude regions, are consistent with those in MISR red and NIR bands. An algorithm was developed to retrieve ice cloud optical thickness using matched MODIS and MISR data. The MODIS data are used to derive ice cloud particle size. The retrieved ice cloud particle sizes are then collocated to the MISR pixel for cloud optical thickness retrievals at the 9 MISR views. Errors in cloud property retrievals are examined when MODIS retrievals are not provided. For the solar and satellite viewing angles applied most closely to the operational conditions in cloud property retrievals, the relative errors in cloud optical thickness are within ±10% when the ice cloud model that consists of only columns. For the plate ice cloud model, substantial errors may arise from the absence of MODIS retrievals of cloud particle size. Therefore, particle-size dependent biases can be efficiently removed by using the MODIS-retrieved particle size in the MISR retrieval of ice cloud optical thickness.

The ice cloud optical thicknesses are retrieved for the 9 MISR viewing geometries in the overlap regions of MODIS and MISR granules. The differences between cloud optical thickness retrieved at the 9 views and their mean are used to characterize the retrieval accuracy. Ice cloud models containing single and mixed ice crystal habits are initially examined using MODIS and MISR data at two 5-minute intervals. The ice cloud model with surface roughened columns has the best overall performance in fitting the reflectances with the cloud property retrievals. The ice cloud models are further tested using the daytime MODIS and MISR data taken over ocean for the entire day of 2 July 2009. The retrieved ice cloud optical thicknesses tend to be overestimated and underestimated fore and aft of the local vertical directions. Employing mixtures of inhomogeneous and homogeneous ice crystals with surface roughness is found to further reduce the uncertainty in the ice cloud retrievals, but only by a small amount. A new ice cloud model containing a mixture of ice crystal habits or a distribution of severely roughened hexagonal ice columns is recommended for the future satellite-based retrievals of ice cloud properties for both optically thin and thick clouds.

CHAPTER V

SUMMARY AND CONCLUSIONS

Representation of ice clouds in radiative transfer simulations is subject to uncertainties associated with the shapes and sizes of ice crystals within cirrus clouds. This doctoral study represents an effort to improve the ice cloud models used in the operational retrieval of ice cloud properties. Realistic ice crystal geometries are defined on the basis of the observations of ice crystals and the ice crystal habits used in the current satellite-based remote sensing of cirrus clouds. An algorithm is then developed in order to employ the new ice crystals to the ice cloud models.

The single-scattering properties of inhomogeneous ice crystals containing air bubbles are first investigated. Unlike the IHM model developed by *Labonnote et al.* [2001], large air bubbles are included within hexagonal ice crystals on the basis of the observations made by *Tape* [1994]. The IGOM [*Yang and Liou*, 1996b] is used to simulate the scattering of light by the inhomogeneous ice crystals with random orientations. The effect of the inhomogeneous ice crystals is to smooth the phase functions, diminish the 22° and 46° halo peaks, and reduce the backscatter in comparison with the case of bubble-free ice crystals. This feature is consistent with those reported by *Labonnote et al.* [2001] and *Yang et al.* [2008b] because the air bubbles within the ice crystals may cause the spreading of the rays that associated with the minimum deviation of refraction. However, the air bubbles in the current ice crystal geometry reduced the overall ice water content compared to the IHM model. The asymmetry factors of inhomogeneous ice crystals decrease as the ratio of air-bubble volume to ice crystal

volume increases. The reflectances simulated for inhomogeneous ice crystals are larger than those computed for homogeneous ice crystals at a wavelength of 0.65 μm. Thus, the retrieved cloud optical thickness is reduced by employing inhomogeneous ice cloud models. At a wavelength of 2.13 μm, including air bubbles in ice crystal morphology may also increase the reflectance. This effect implies, particularly in the case of large air bubbles, that the retrieved effective particle size for inhomogeneous ice crystals is larger than that retrieved for homogeneous ice crystals.

Errors in the simulation of light scattering by aggregates may also have significant impacts on the retrieval of ice cloud properties. In regions of deep tropical convection, ice particles often undergo aggregation and form complex chains. The effect of the representation of aggregates on electromagnetic scattering calculations is investigated by developing an algorithm to efficiently specify the geometries of aggregates and to compute some of their geometric parameters such as the projected area. Compared to the previous studies on aggregates [*Evans et al.*, 2005; *Um and McFarquhar*, 2009; *Yang and Liou*, 1998], the current algorithm is able to represent the great natural variability of the actual aggregates. The ADDA [*Yurkin et al.*, 2007; *Yurkin and Hoekstra*, 2009] and IGOM [*Yang and Liou*, 1996b] are used to compute the scattering properties of individual aggregate ice particles whose size parameters are smaller and larger than 25, respectively. Aggregates are defined as hexagonal plates attached together in a chain-like manner. It has been found that an aggregate model containing 10 ensemble members provides an accurate and computationally efficient way to represent all aggregates occurring within ice clouds. Furthermore, the aggregate model can be used to study the influence of these complex ice particles on satellite-based remote sensing of ice clouds. The computed

cloud reflectances for aggregates are different from those associated with randomly oriented individual hexagonal plates. When aggregates are ignored, simulated cloud reflectances are generally lower at visible and near-infrared wavelengths resulting in larger effective particle sizes but smaller optical thicknesses. The present aggregate model may potentially be useful in remote sensing of ice cloud properties.

To improve the retrieval of ice cloud properties, we examined several ice cloud models consisting of smooth, roughened, homogeneous, and inhomogeneous hexagonal ice crystals with various aspect ratios. The sensitivity of the bulk scattering properties and solar reflectances of cirrus clouds to specific ice cloud models is investigated using the IGOM [*Yang and Liou*, 1996b] and the DISORT [*Stamnes et al.*, 1988] model. The ice crystal habits may significantly affect the simulations of cloud reflectances at visible through near-infrared wavelengths. The relative maxima of the reflectances associated with forward and backward scattering are reduced from the use of roughened ice crystals. A new algorithm is developed to help determine an appropriate ice cloud model for application to the satellite-based retrieval of ice cloud properties. The ice cloud particle size retrieved from MODIS data, collocated with MISR observations, is used to infer the optical thicknesses of ice clouds for 9 MISR scattering angles. It was demonstrated that substantial errors of cloud optical thicknesses may arise when MODIS retrievals are not provided and hexagonal plates are assumed in the ice cloud model. The differences between view-dependent cloud optical thickness and the averaged value over the 9 MISR viewing angles are used to evaluate the ice cloud models. In the case for 2 July 2009, the ice cloud model with mixed ice crystal habits is the best fit to the observations. The ice cloud model also produces consistent cloud property retrievals for the 9 MISR viewing

configurations within the measurement uncertainties. Compared to the studies reported by *Doutriaux-Boucher et al.* [2000] and *McFarlane et al.* [2005], this current work is an initial effort on improving the ice cloud models by using pixel-by-pixel retrievals of ice cloud properties from satellite viewing angles. Employing other ice crystal habits, i.e., bullet rosettes, droxtals, hollow columns, and aggregates deserves further study and may further improve the performance of the ice cloud models in the retrieval of ice cloud properties.

REFERENCES

Ardanuy, P. E., D. Han, and V. V. Salomonson (1991), The Moderate Resolution Imaging Spectrometer (Modis) science and data system requirements, *IEEE Transactions on Geoscience and Remote Sensing*, *29*(1), 75-88.

Arnott, W. P., Y. Y. Dong, J. Hallett, and M. R. Poellot (1994), Role of small ice crystals in radiative properties of cirrus: A case study, FIRE II, November 22, 1991, *J. Geophys. Res.*, *99*(D1), 1371-1381.

Auer, A. H., and D. L. Veal (1970), Dimension of ice crystals in natural clouds, *J. Atmos. Sci.*, *27*(6), 919-926.

Bailey, M., and J. Hallett (2004), Growth rates and habits of ice crystals between -20° and -70°C, *J. Atmos. Sci.*, *61*(5), 514-544.

Baker, B. A., and R. P. Lawson (2006), In situ observations of the microphysical properties of wave, cirrus, and anvil clouds. Part I: Wave clouds, *J. Atmos. Sci.*, *63*(12), 3160-3185.

Baran, A. J., P. N. Francis, L. C. Labonnote, and M. Doutriaux-Boucher (2001a), A scattering phase function for ice cloud: Tests of applicability using aircraft and satellite multi-angle multi-wavelength radiance measurements of cirrus, *Q. J. R. Meteorol. Soc.*, *127*(577), 2395-2416.

Baran, A. J., P. Yang, and S. Havemann (2001b), Calculation of the single-scattering properties of randomly oriented hexagonal ice columns: A comparison of the T-matrix and the finite-difference time-domain methods, *Appl. Opt.*, *40*(24), 4376-4386.

Baran, A. J. (2004), On the scattering and absorption properties of cirrus cloud, *J. Quant. Spectrosc. Radiat. Transfer*, *89*(1-4), 17-36.

Baran, A. J., V. N. Shcherbakov, B. A. Baker, J. F. Gayet, and R. P. Lawson (2005), On the scattering phase-function of non-symmetric ice-crystals, *Q. J. R. Meteorol. Soc.*, *131*(611), 2609-2616.

Baran, A. J., and L. C. Labonnote (2006), On the reflection and polarisation properties of ice cloud, *J. Quant. Spectrosc. Radiat. Transfer*, *100*(1-3), 41-54.

Baran, A. J., and L. C. Labonnote (2007), A self-consistent scattering model for cirrus. I: The solar region, *Q. J. R. Meteorol. Soc.*, *133*(629), 1899-1912.

Baum, B. A., D. P. Kratz, P. Yang, S. C. Ou, Y. X. Hu, P. F. Soulen, and S. C. Tsay (2000), Remote sensing of cloud properties using MODIS airborne simulator imagery during SUCCESS. Part I: Data and models, *J. Geophys. Res.*, *105*(D9), 11767-11780.

Baum, B. A., R. A. Frey, G. G. Mace, M. K. Harkey, and P. Yang (2003), Nighttime multilayered cloud detection using MODIS and ARM data, *J. Appl. Meteor.*, *42*(7), 905-919.

Baum, B. A., A. J. Heymsfield, P. Yang, and S. T. Bedka (2005a), Bulk scattering properties for the remote sensing of ice clouds. Part I: Microphysical data and models, *J. Appl. Meteor.*, *44*(12), 1885-1895.

Baum, B. A., P. Yang, A. J. Heymsfield, S. Platnick, M. D. King, Y. X. Hu, and S. T. Bedka (2005b), Bulk scattering properties for the remote sensing of ice clouds. Part II: Narrowband models, *J. Appl. Meteor.*, *44*(12), 1896-1911.

Baum, B. A., P. Yang, S. Nasiri, A. K. Heidinger, A. Heymsfield, and J. Li (2007), Bulk scattering properties for the remote sensing of ice clouds. Part III: High-resolution spectral models from 100 to 3250 cm-1, *J. Appl. Meteor.*, *46*(4), 423-434.

Baumgardner, D., H. Chepfer, G. B. Raga, and G. L. Kok (2005), The shapes of very small cirrus particles derived from in situ measurements, *Geophys. Res. Lett.*, *32*(1), L01806, doi:01810.01029/02004GL021300.

Bi, L., P. Yang, G. W. Kattawar, B. A. Baum, Y. X. Hu, D. M. Winker, R. S. Brock, and J. Q. Lu (2009a), Simulation of the color ratio associated with the backscattering of radiation by ice crystals at 0.532 and 1.064 μm wavelengths, *J. Geophys. Res.*, *114*, D00H08, doi: 10.1029/2009JD011759.

Bi, L., P. Yang, G. W. Kattawar, and R. Kahn (2009b), Single-scattering properties of triaxial ellipsoidal particles for a size parameter range from the Rayleigh to geometric-optics regimes, *Appl. Opt.*, *48*(1), 114-126.

Borovoi, A. G., and I. A. Grishin (2003), Scattering matrices for large ice crystal particles, *J. Opt. Soc. Am. A*, *20*(11), 2071-2080.

Cai, Q., and K. N. Liou (1982), Polarized-light scattering by hexagonal ice crystals: Theory, *Appl. Opt.*, *21*(19), 3569-3580.

Carte, A. E. (1961), Air bubbles in ice, *Proc. Phys. Soc.*, *77*(495), 757-768.

Chepfer, H., P. Goloub, J. Riedi, J. F. De Haan, J. W. Hovenier, and P. H. Flamant (2001), Ice crystal shapes in cirrus clouds derived from POLDER/ADEOS-1, *J. Geophys. Res.*, *106*(D8), 7955-7966.

Chepfer, H., P. Minnis, D. Young, L. Nguyen, and R. F. Arduini (2002), Estimation of cirrus cloud effective ice crystal shapes using visible reflectances from dual-satellite measurements, *J. Geophys. Res.*, *107*(D23), 4730, doi: 4710.1029/2000JD000240.

Chepfer, H., V. Noel, P. Minnis, D. Baumgardner, L. Nguyen, G. Raga, M. J. McGill, and P. Yang (2005), Particle habit in tropical ice clouds during CRYSTAL-FACE: Comparison of two remote sensing techniques with in situ observations, *J. Geophys. Res.*, *110*(D16), D16204, doi:16210.11029/12004JD005455.

Coleman, R. F., and K. N. Liou (1981), Light scattering by hexagonal ice crystals, *J. Atmos. Sci.*, *38*(6), 1260-1271.

Connolly, P. J., C. P. R. Saunders, M. W. Gallagher, K. N. Bower, M. J. Flynn, T. W. Choularton, J. Whiteway, and R. P. Lawson (2005), Aircraft observations of the influence of electric fields on the aggregation of ice crystals, *Q. J. R. Meteorol. Soc.*, *131*(608), 1695-1712.

Cox, C., and W. Munk (1954), Measurement of the roughness of the sea surface from photographs of the sun's glitter, *J. Opt. Soc. Am.*, *44*, 838-850

Davies, R. (1984), Reflected solar radiances from broken cloud scenes and the interpretation of scanner measurements, *J. Geophys. Res.*, *89*(D1), 1259-1266.

Diner, D. J., C. J. Bruegge, J. V. Martonchik, T. P. Ackerman, R. Davies, S. A. W. Gerstl, H. R. Gordon, P. J. Sellers, J. Clark, J. A. Daniels, E. D. Danielson, V. G. Duval, K. P. Klaasen, G. W. Lilienthal, D. I. Nakamoto, R. J. Pagano, and T. H. Reilly (1989), MISR: A multiangle imaging spectroradiometer for geophysical and climatological research from Eos, *IEEE Transactions on Geoscience and Remote Sensing*, *27*(2), 200-214.

Diner, D. J., R. Davies, L. D. Girolamo, A. Horvath, C. Moroney, J. P. Muller, S. R. Paradise, D. Wenkert, and J. Zong (1997), MISR Level 2 aerosol retrieval algorithm theoretical basis, *JPL document D-11400, Rev. C*, Jet Propulsion Laboratory, Pasadena, CA.

Diner, D. J., J. C. Beckert, T. H. Reilly, C. J. Bruegge, J. E. Conel, R. A. Kahn, J. V. Martonchik, T. P. Ackerman, R. Davies, S. A. W. Gerstl, H. R. Gordon, J. P. Muller, R. B. Myneni, P. J. Sellers, B. Pinty, and M. M. Verstraete (1998), Multi-angle Imaging SpectroRadiometer (MISR) instrument description and experiment overview, *IEEE Transactions on Geoscience and Remote Sensing*, *36*(4), 1072-1087.

Diner, D. J., J. C. Beckert, G. W. Bothwell, and J. I. Rodriguez (2002), Performance of the MISR instrument during its first 20 months in Earth orbit, *IEEE Transactions on Geoscience and Remote Sensing*, *40*(7), 1449-1466.

Dinh-Van, P., and L. Phan-Cong (1978), Aggregation of small ice crystals in an electric field, *Atmosphere-Ocean*, *16*, 248-259.

Doutriaux-Boucher, M., J. C. Buriez, G. Brogniez, L. C. Labonnote, and A. J. Baran (2000), Sensitivity of retrieved POLDER directional cloud optical thickness to various ice particle models, *Geophys. Res. Lett.*, *27*(1), 109-112.

Draine, B. T. (1988), The discrete dipole approximation and its application to interstellar graphite grains, *Astrophys. J.*, *333*(2), 848-872.

Draine, B. T., and J. Goodman (1993), Beyond Clausius-Mossotti-wave-propagation on a polarizable point lattice and the discrete dipole approximation, *Astrophys. J.*, *405*(2), 685-697.

Draine, B. T., and P. J. Flatau (1994), Discrete-dipole approximation for scattering calculations, *J. Opt. Soc. Am. A*, *11*(4), 1491-1499.

Evans, K. F., and G. L. Stephens (1995), Microwave radiative transfer through clouds composed of realistically shaped ice crystals. Part I: Single scattering properties, *J. Atmos. Sci.*, *52*(11), 2041-2057.

Evans, K. F., J. R. Wang, P. E. Racette, G. Heymsfield, and L. H. Li (2005), Ice cloud retrievals and analysis with the compact scanning submillimeter imaging radiometer and the cloud radar system during CRYSTAL FACE, *J. Appl. Meteorol.*, *44*(6), 839-859.

Foot, J. S. (1988), Some observations of the optical properties of clouds. II: Cirrus, *Q. J. R. Meteorol. Soc.*, *114*(479), 145-164.

Freedman, D., R. Pisani, and R. Purves (2007), *Statistics*, 4th ed., W. W. North & Company, New York.

Fu, Q., W. B. Sun, and P. Yang (1999), Modeling of scattering and absorption by nonspherical cirrus ice particles at thermal infrared wavelengths, *J. Atmos. Sci.*, *56*(16), 2937-2947.

Gallagher, M. W., P. J. Connolly, J. Whiteway, D. Figueras-Nieto, M. Flynn, T. W. Choularton, K. N. Bower, C. Cook, R. Busen, and J. Hacker (2005), An overview of the microphysical structure of cirrus clouds observed during EMERALD-1, *Q. J. R. Meteorol. Soc.*, *131*(607), 1143-1169.

Gatebe, C. K., M. D. King, A. I. Lyapustin, G. T. Arnold, and J. Redemann (2005), Airborne spectral measurements of ocean directional reflectance, *J. Atmos. Sci.*, *62*(4), 1072-1092.

Hallett, J. (1964), Experimental studies of the crystallization of supercooled water, *J. Atmos. Sci.*, *21*(6), 671-682.

Hess, M., and M. Wiegner (1994), COP: A data library of optical-properties of hexagonal ice crystals, *Appl. Opt.*, *33*(33), 7740-7746.

Hess, M., R. B. A. Koelemeijer, and P. Stammes (1998), Scattering matrices of imperfect hexagonal ice crystals, *J. Quant. Spectrosc. Radiat. Transfer*, *60*(3), 301-308.

Heymsfield, A. J., and C. M. R. Platt (1984), A parameterization of the particle size spectrum of ice clouds in terms of the ambient temperature and the ice water content, *J. Atmos. Sci.*, *41*(5), 846-855.

Heymsfield, A. J. (1986), Ice particle evolution in the anvil of a severe thunderstorm during CCOPE, *J. Atmos. Sci.*, *43*(21), 2463-2478.

Heymsfield, A. J., K. M. Miller, and J. D. Spinhirne (1990), The 27-28 October 1986 FIRE IFO cirrus case study: Cloud microstructure, *Mon. Wea. Rev.*, *118*(11), 2313-2328.

Heymsfield, A. J., A. Bansemer, P. R. Field, S. L. Durden, J. L. Stith, J. E. Dye, W. Hall, and C. A. Grainger (2002), Observations and parameterizations of particle size distributions in deep tropical cirrus and stratiform precipitating clouds: Results from in situ observations in TRMM field campaigns, *J. Atmos. Sci.*, *59*(24), 3457-3491.

Heymsfield, A. J. (2003), Properties of tropical and midlatitude ice cloud particle ensembles. Part I: Median mass diameters and terminal velocities, *J. Atmos. Sci.*, *60*(21), 2573-2591.

Heymsfield, A. J., and L. M. Miloshevich (2003), Parameterizations for the cross-sectional area and extinction of cirrus and stratiform ice cloud particles, *J. Atmos. Sci.*, *60*(7), 936-956.

Hobbs, P., S. Chang, and J. Locatelli (1974), The dimension and aggregation of ice crystals in natural clouds, *J. Geophys. Res.*, *79*, 2199-2206

Hong, G., P. Yang, B. A. Baum, A. J. Heymsfield, F. Z. Weng, Q. H. Liu, G. Heygster, and S. A. Buehler (2009), Scattering database in the millimeter and submillimeter wave range of 100-1000 GHz for nonspherical ice particles, *J. Geophys. Res.*, *114*, D06201, doi: 06210.01029/02008JD010451.

Houze, R. A., and D. D. Churchill (1987), Mesoscale organization and cloud microphysics in a Bay of Bengal depression, *J. Atmos. Sci.*, *44*(14), 1845-1867.

Iaquinta, J., H. Isaka, and P. Personne (1995), Scattering phase function of bullet rosette ice crystals, *J. Atmos. Sci.*, *52*(9), 1401-1413.

Iwabuchi, H., and T. Hayasaka (2002), Effects of cloud horizontal inhomogeneity on the optical thickness retrieved from moderate-resolution satellite data, *J. Atmos. Sci.*, *59*(14), 2227-2242.

Jensen, E., D. O. Starr, and O. B. Toon (2004), Mission investigates tropical cirrus clouds, *Eos, Trans. Amer. Geophys. Union*, *85*, 45-50.

Kahnert, F. M. (2003), Numerical methods in electromagnetic scattering theory, *J. Quant. Spectrosc. Radiat. Transfer*, *79*, 775-824.

Kajikawa, M., and A. J. Heymsfield (1989), Aggregation of ice crystals in cirrus, *J. Atmos. Sci.*, *46*(20), 3108-3121.

Kalashnikova, O. V., and I. N. Sokolik (2004), Modeling the radiative properties of nonspherical soli-derived mineral aerosols, *J. Quant. Specrtrosc. Radiat. Transfer 87*(2), 137-166.

Kato, S., and A. Marshak (2009), Solar zenith and viewing geometry-dependent errors in satellite retrieved cloud optical thickness: Marine stratocumulus case, *J. Geophys. Res.*, *114*, D01202, doi 01210.01029/02008JD010579.

King, M. D., S. Platnick, P. Yang, G. T. Arnold, M. A. Gray, J. C. Riedi, S. A. Ackerman, and K. N. Liou (2004), Remote sensing of liquid water and ice cloud optical thickness and effective radius in the Arctic: Application of airborne multispectral MAS data, *J Atmos Ocean Tech*, *21*(6), 857-875.

Knap, W. H., L. C. Labonnote, G. Brogniez, and P. Stammes (2005), Modeling total and polarized reflectances of ice clouds: Evaluation by means of POLDER and ATSR-2 measurements, *Appl. Opt.*, *44*(19), 4060-4073.

Kobayashi, T. (1961), The growth of snow crystals at low supersaturation, *Philadelphia Magazine*, *6*, 1363-1370.

Korolev, A. V., G. A. Isaac, and J. Hallett (1999), Ice particle habits in Arctic clouds, *Geophys. Res. Lett.*, *26*(9), 1299-1302.

Kosarev, A. L., and I. P. Mazin (1991), An empirical model of the physical structure of upper-layer clouds, *Atmos. Res.*, *26*, 213-228.

Labonnote, L. C., G. Brogniez, J. C. Buriez, M. Doutriaux-Boucher, J. F. Gayet, and A. Macke (2001), Polarized light scattering by inhomogeneous hexagonal monocrystals: Validation with ADEOS-POLDER measurements, *J. Geophys. Res.*, *106*(D11), 12139-12153.

Lawless, R., Y. Xie, and P. Yang (2006), Polarization and effective Mueller matrix for multiple scattering of light by nonspherical ice crystals, *Opt Express*, *14*(14), 6381-6393.

Lawson, R. P., A. J. Heymsfield, S. M. Aulenbach, and T. L. Jensen (1998), Shapes, sizes and light scattering properties of ice crystals in cirrus and a persistent contrail during SUCCESS, *Geophys. Res. Lett.*, *25*(9), 1331-1334.

Lawson, R. P., B. A. Baker, C. G. Schmitt, and T. L. Jensen (2001), An overview of microphysical properties of Arctic clouds observed in May and July 1998 during FIRE ACE, *J. Geophys. Res.*, *106*(D14), 14989-15014.

Lawson, R. P., B. Baker, B. Pilson, and Q. X. Mo (2006), In situ observations of the microphysical properties of wave, cirrus, and anvil clouds. Part II: Cirrus clouds, *J. Atmos. Sci.*, *63*(12), 3186-3203.

Li, J., H. L. Huang, C. Y. Liu, P. Yang, T. J. Schmit, H. L. Wei, E. Weisz, L. Guan, and W. P. Menzel (2005), Retrieval of cloud microphysical properties from MODIS and AIRS, *J. Appl. Meteorol. Clim.*, *44*(10), 1526-1543.

Liou, K. N. (1972), Light scattering by ice clouds in the visible and infrared: A theoretical study, *J. Atmos. Sci.*, *29*(3), 524-536.

Liou, K. N. (1986), Influence of cirrus clouds on weather and climate processes: A global perspective, *Mon. Wea. Rev.*, *114*(6), 1167-1199.

Loeb, N. G., and R. Davies (1997), Angular dependence of observed reflectances: A comparison with plane parallel theory, *J. Geophys. Res.*, *102*(D6), 6865-6881.

Loeb, N. G., and J. A. Coakley (1998), Inference of marine stratus cloud optical depths from satellite measurements: Does 1D theory apply? *J. Clim.*, *11*(2), 215-233.

Mace, G. G., Y. Y. Zhang, S. Platnick, M. D. King, P. Minnis, and P. Yang (2005), Evaluation of cirrus cloud properties from MODIS radiances using cloud properties derived from ground-based data collected at the ARM SGP site, *J. Appl. Meteorol.*, *44*(2), 221-240.

Macke, A. (1993), Scattering of light by polyhedral ice crystals, *Appl. Opt.*, *32*(15), 2780-2788.

Macke, A., and M. I. Mishchenko (1996), Applicability of regular particle shapes in light scattering calculations for atmospheric ice particles, *Appl. Opt.*, *35*(21), 4291-4296.

Macke, A., M. I. Mishchenko, and B. Cairns (1996a), The influence of inclusions on light scattering by large ice particles, *J. Geophys. Res.*, *101*(D18), 23311-23316.

Macke, A., J. Mueller, and E. Raschke (1996b), Single scattering properties of atmospheric ice crystals, *J. Atmos. Sci.*, *53*(19), 2813-2825.

Masuda, K., H. Ishimoto, and T. Takashima (2002), Retrieval of cirrus optical thickness and ice-shape information using total and polarized reflectance from satellite measurements, *J. Quant. Spectrosc. Radiat. Transfer*, *75*(1), 39-51.

McFarlane, S. A., R. T. Marchand, and T. P. Ackerman (2005), Retrieval of cloud phase and crystal habit from Multiangle Imaging Spectroradiometer (MISR) and Moderate Resolution Imaging Spectroradiometer (MODIS) data, *J. Geophys. Res.*, *110*(D14), D14201, doi 14210.11029/12004JD004831.

McFarquhar, G. M., and A. J. Heymsfield (1996), Microphysical characteristics of three anvils sampled during the Central Equatorial Experiment, *J. Atmos. Sci.*, *53*(17), 2401-2423.

McFarquhar, G. M., P. Yang, A. Macke, and A. J. Baran (2002), A new parameterization of single scattering solar radiative properties for tropical anvils using observed ice crystal size and shape distributions, *J. Atmos. Sci.*, *59*(16), 2458-2478.

Min, Q. L., P. Minnis, and M. M. Khaiyer (2004), Comparison of cirrus optical depths from GOES-8 and surface measurements, *J. Geophys. Res.*, *109*, D20119, 20110.21029/22003JD004390.

Minnis, P., P. W. Heck, and D. F. Young (1993), Inference of cirrus cloud properties using satellite-observed visible and infrared radiances. Part II: Verification of theoretical cirrus radiative properties, *J. Atmos. Sci.*, *50*(9), 1305-1322.

Minnis, P., D. P. Garber, D. F. Young, and R. F. Arduini (1998a), Parameterization of reflectance and effective emittance for satellite remote sensing of cloud properties, *J. Atmos. Sci.*, *55*(22), 3313-3339.

Minnis, P., D. P. Garber, D. F. Young, and R. F. Arduini (1998b), Parameterizations of reflectance and effective emittance for satellite remote sensing of cloud properties, *J. Atmos. Sci.*, *55*(22), 3313-3339.

Minnis, P., D. Young, S. Sun-Mack, P. W. Heck, D. R. Doelling, and Q. Z. Trepte (2004), CERES cloud property retrievals from imagers on TRMM, Terra, and Aqua, paper presented at Proc. SPIE 10th Int. Symp. on Remote Sensing: Conf. on Remote Sensing of Clouds and the Atmosphere VII, Barcelona, Spain.

Minnis, P., S. Sun-Mack, D. F. Young, P. W. Heck, D. P. Garber, Y. Chen, D. A. Spangenberg, R. F. Arduini, Q. Z. Trepte, W. L. Smith, J. K. Ayers, S. C. Gibson, W. F. Miller, V. Chakrapani, Y. Takano, K. N. Liou, and Y. Xie (submitted), CERES Edition-2 cloud property retrievals using TRMM VIRS and Terra and Aqua MODIS data, Part I: Algorithms, *Geosci. Remote Ses*.

Mishchenko, M. I., W. B. Rossow, A. Macke, and A. A. Lacis (1996), Sensitivity of cirrus cloud albedo, bidirectional reflectance and optical thickness retrieval accuracy to ice particle shape, *J. Geophys. Res.*, *101*(D12), 16973-16985.

Mitchell, D. L. (1991), Evolution of snow-size spectra in cyclonic storms. Part II: Deviations from the exponential form, *J. Atmos. Sci.*, *48*(16), 1885-1899.

Mitchell, D. L., and W. P. Arnott (1994), A model predicting the evolution of ice particle-size spectra and radiative properties of cirrus clouds .Part II: Dependence of absorption and extinction on ice crystal morphology, *J. Atmos. Sci.*, *51*(6), 817-832.

Mitchell, D. L., W. P. Arnott, C. Schmitt, A. J. Baran, S. Havemann, and Q. Fu (2001), Photon tunneling contributions to extinction for laboratory grown hexagonal columns, *J. Quant. Spectrosc. Radiat. Transfer*, *70*(4-6), 761-776.

Muinonen, K. (1989), Scattering of light by crystals: A modified Kirchhoff approximation, *Appl. Opt.*, *28*(15), 3044-3050.

Nakajima, T., and M. D. King (1990), Determination of the optical thickness and effective particle radius of clouds from reflected solar radiation measurements. Part I: Theory, *J. Atmos. Sci.*, *47*(15), 1878-1893.

Nasiri, S. L., B. A. Baum, A. J. Heymsfield, P. Yang, M. R. Poellot, D. P. Kratz, and Y. X. Hu (2002), The development of midlatitude cirrus models for MODIS using FIRE-I, FIRE-II, and ARM in situ data, *J. Appl. Meteor.*, *41*(3), 197-217.

Noel, V., D. M. Winker, M. McGill, and P. Lawson (2004), Classification of particle shapes from lidar depolarization ratio in convective ice clouds compared to in situ observations during CRYSTAL-FACE, *J. Geophys. Res.*, *109*(D24), D24213, doi:24210.21029/22004JD004883.

Nousiainen, T., and K. Muinonen (2007), Surface-roughness effect on single-scattering properties of wavelength-scale particles, *J. Quant. Specrtrosc. Radiat. Transfer 106*, 389-397

Nousiainen, T., E. Zubko, J. V. Niemi, K. Kupiainen, M. Lehtinen, K. Muinonen, and G. Videen (2009), Single-scattering modeling of thin, birefringent mineral-dust flakes using the discrete-dipole approximation, *J. Geophys. Res.*, *114*, D07207, doi:07210.01029/02008JD011564.

Nussenzveig, H. M., and W. J. Wiscombe (1980), Efficiency factors in Mie scattering, *Phys. Rev. Lett.*, *45*(18), 1490-1494.

Nussenzveig, H. M., and W. J. Wiscombe (1991), Complex angular momentum approximation to hard-core scattering, *Phys. Rev. A.*, *43*(5), 2093-2112.

Ono, A. (1969), The shape and riming properties of ice crystals in natural clouds, *J. Atmos. Sci.*, *26*(1), 138-147.

Oreopoulos, L., and R. Davies (1998), Plane parallel albedo biases from satellite observations. Part I: Dependence on resolution and other factors, *J. Clim.*, *11*(5), 919-932.

Pinker, R. T., and I. Laszlo (1992), Modeling surface solar irradiance for satellite applications on a global scale, *J. Appl. Meteorol.*, *31*(2), 194-211.

Pruppacher, H. R. (1963), The effects of electric fields on cloud physical processes, *J. Appl. Math. and Phys.*, *14*(5), 590-599.

Pruppacher, H. R., and J. D. Klett (1980), *Microphysics of clouds and precipitation*, Reidel, Boston, MA.

Purcell, E. M., and C. R. Pennypacker (1973), Scattering and absorption of light by nonspherical dielectric grains, *Astrophys. J.*, *186*(2), 705-714.

Ramanathan, V., E. J. Pitcher, R. C. Malone, and M. L. Blackmon (1983), The response of a general circulation model to refinements in radiative processes, *J. Atmos. Sci.*, *40*(3), 605-630.

Sassen, K., N. C. Knight, Y. Takano, and A. J. Heymsfield (1994), Effects of ice-crystal structure on halo formation: Cirrus cloud experimental and ray-tracing modeling studies, *Appl. Opt.*, *33*(21), 4590-4601.

Schmitt, C. G., J. Iaquinta, and A. J. Heymsfield (2006), The asymmetry parameter of cirrus clouds composed of hollow bullet rosette–shaped ice crystals from ray-tracing calculations, *J. Appl. Meteorol. Clim.*, *45*(7), 973-981.

Shcherbakov, V., J. F. Gayet, B. Baker, and P. Lawson (2006), Light scattering by single natural ice crystals, *J. Atmos. Sci.*, *63*(5), 1513-1525.

Silva Dias, M. A. F., S. Rutledge, P. Kabat, P. L. S. Dias, C. Nobre, G. Fisch, A. J. Dolman, E. Zipser, M. Garstang, A. O. Manzi, J. D. Fuentes, H. R. Rocha, J. Marengo, A. Plana-Fattori, L. D. A. Sa, R. C. S. Alvala, M. O. Andreae, P. Artaxo, R. Gielow, and L. Gatti (2002), Cloud and rain processes in a biosphere-atmosphere interaction context in the Amazon Region, *J. Geophys. Res.*, *107*(D20), 8072, doi:8010.1029/2001JD000335.

Stamnes, K., S. C. Tsay, W. Wiscombe, and K. Jayaweera (1988), Numerically stable algorithm for discrete-ordinate-method radiative transfer in multiple scattering and emitting layered media, *Appl. Opt.*, *27*(12), 2502-2509.

Starr, D. O. (1987), A cirrus-cloud experiment: Intensive field observations planned for FIRE, *Bull. Amer. Meteor. Soc.*, *68*(2), 119-124.

Stith, J. L., J. E. Dye, A. Bansemer, A. J. Heymsfield, C. A. Grainger, W. A. Petersen, and R. Cifelli (2002), Microphysical observations of tropical clouds, *J. Appl. Meteorol.*, *41*(2), 97-117.

Stith, J. L., J. A. Haggerty, A. Heymsfield, and C. A. Grainger (2004), Microphysical characteristics of tropical updrafts in clean conditions, *J. Appl. Meteorol.*, *43*(5), 779-794.

Sun, W. B., N. G. Loeb, and P. Yang (2006), On the retrieval of ice cloud particle shapes from POLDER measurements, *J. Quant. Spectrosc. Radiat. Transfer*, *101*(3), 435-447.

Takano, Y., and K. N. Liou (1989), Solar radiative transfer in cirrus clouds. Part I: Single-scattering and optical properties of hexagonal ice crystals, *J. Atmos. Sci.*, *46*(1), 3-19.

Takano, Y., and K. N. Liou (1995), Radiative transfer in cirrus clouds .Part III: Light-scattering by irregular ice crystals, *J. Atmos. Sci.*, *52*(7), 818-837.

Tape, W. (1983), Some ice crystals that made halos, *J. Opt. Soc. Am.*, *73*(12), 1641-1645.

Tape, W. (1994), *Atmospheric halos*, 143 pp., American Geophysical Union, Washington, D.C.

Um, J., and G. M. McFarquhar (2007), Single-scattering properties of aggregates of bullet rosettes in cirrus, *J. Appl. Meteorol. Clim.*, *46*(6), 757-775.

Um, J., and G. M. McFarquhar (2009), Single-scattering properties of aggregates of plates, *Q. J. R. Meteorol. Soc.*, *135*(639), 291-304.

Wendisch, M., P. Pilewskie, J. Pommier, S. Howard, P. Yang, A. J. Heymsfield, C. G. Schmitt, D. Baumgardner, and B. Mayer (2005), Impact of cirrus crystal shape on solar spectral irradiance: A case study for subtropical cirrus, *J. Geophys. Res.*, *110*(D3), D03202, doi: 03210.01029/02004JD005294.

Wendisch, M., P. Yang, and P. Pilewskie (2007), Effects of ice crystal habit on thermal infrared radiative properties and forcing of cirrus, *J. Geophys. Res.*, *112*(D8), D08201, doi:08210.01029/02006JD007899.

Wiscombe, W. J. (1977), The delta-M method: Rapid yet accurate radiative flux calculations for strongly asymmetric phase functions, *J. Atmos. Sci.*, *34*(9), 1408-1422.

Xie, Y., P. Yang, G. W. Kattawar, P. Minnis, and Y. X. Hu (2009), Effect of the inhomogeneity of ice crystals on retrieving ice cloud optical thickness and effective particle size, *J. Geophys. Res.*, *114*, D11203, doi:11210.11029/12008JD011216.

Yang, P., and K. N. Liou (1995), Light scattering by hexagonal ice crystals: Comparison of finite-difference time domain and geometric optics models, *J. Opt. Soc. Am. A*, *A12*(1), 162-176.

Yang, P., and K. N. Liou (1996a), Finite-difference time domain method for light scattering by small ice crystals in three-dimensional space, *J. Opt. Soc. Am. A*, *13*(10), 2072-2085.

Yang, P., and K. N. Liou (1996b), Geometric-optics-integral-equation method for light scattering by nonspherical ice crystals, *Appl. Opt.*, *35*(33), 6568-6584.

Yang, P., and K. N. Liou (1997), Light scattering by hexagonal ice crystals: Solutions by a ray-by-ray integration algorithm, *J. Opt. Soc. Am. A*, *14*(9), 2278-2289.

Yang, P., and K. N. Liou (1998), Single scattering properties of complex ice crystals in terrestrial atmosphere, *Contrib. Atmos. Phys.*, *71*, 223-248.

Yang, P., K. N. Liou, M. I. Mishchenko, and B. C. Gao (2000), An efficient finite-difference time domain scheme for light scattering by dielectric particles: Application to aerosols, *Appl. Opt.*, *39*(21), 3727-3737.

Yang, P., H. L. Wei, H. L. Huang, B. A. Baum, Y. X. Hu, G. W. Kattawar, M. I. Mishchenko, and Q. Fu (2005), Scattering and absorption property database for nonspherical ice particles in the near- through far-infrared spectral region, *Appl. Opt.*, *44*(26), 5512-5523.

Yang, P., G. Hong, G. W. Kattawar, P. Minnis, and Y. X. Hu (2008a), Uncertainties associated with the surface texture of ice particles in satellite-based retrieval of cirrus clouds. Part II: Effect of particle surface roughness on retrieved cloud optical thickness and effective particle size, *IEEE Transactions on Geoscience and Remote Sensing 46*(7), 1948-1957.

Yang, P., G. W. Kattawar, G. Hong, P. Minnis, and Y. X. Hu (2008b), Uncertainties associated with the surface texture of ice particles in satellite-based retrieval of cirrus clouds. Part I: Single-scattering properties of ice crystals with surface roughness, *IEEE Transactions on Geoscience and Remote Sensing 46*(7), 1940-1947.

Yang, P., Z. B. Zhang, G. W. Kattawar, S. G. Warren, B. A. Baum, H. L. Huang, Y. X. Hu, D. Winker, and J. Iaquinta (2008c), Effect of cavities on the optical properties of bullet rosettes: Implications for active and passive remote sensing of ice cloud properties, *J. Appl. Meteorol. Clim.*, *47*(9), 2311-2330.

Yang, P., and Q. Fu (2009), Dependence of ice crystal optical properties on particle aspect ratio, *J. Quant. Spectrosc. Radiat. Transfer*, *110*(14-16), 1604-1614.

Yurkin, M. A., V. P. Maltsev, and A. G. Hoekstra (2007), The discrete dipole approximation for simulation of light scattering by particles much larger than the wavelength, *J. Quant. Spectrosc. Radiat. Transfer*, *106*(1-3), 546-557.

Yurkin, M. A., and A. G. Hoekstra (2009), *User manual for the discrete dipole approximation code ADDA v.0.79*, *http://adda.googlecode.com/svn/tags/rel_0_79/doc/manual.pdf*

Yuter, S. E., R. A. Houze, E. A. Smith, T. T. Wilheit, and E. Zipser (2005), Physical characterization of tropical oceanic convection observed in KWAJEX, *J. Appl. Meteorol. Clim.*, *44*(4), 385-415.

APPENDIX A

ESTIMATING THE RELATIVE POSITION OF HEXAGONAL PARTICLES

Figure A1 shows the geometries of hexagonal particles used in our study. In particle A, the faces, edges, and vertices of the particle are indicated by $F_{iA}(iA=1,2,...,8)$, $L_{jA}(jA=1,2,...,18)$, and $P_{kA}(kA=1,2,...,12)$, respectively. $\overrightarrow{c_{iA}}(iA=1,2,...,8)$ are the position vectors of the centers of the particle faces, $\overrightarrow{f_{iA}}(iA=1,2,...,8)$ indicate the normal directions of the particle faces, and $\overrightarrow{p_{kA}}(kA=1,2,...,12)$ and $\overrightarrow{l_{jA}}(jA=1,2,...,18)$ are the vectors of the vertices and edges, respectively.

The distance between two hexagonal particles that are not overlapped in the oxyz coordinate can be written by

$$D=\left\langle \begin{matrix} D(P_{kA},F_{iB},kA=1,2,...,12,iB=1,2,...,8) \\ D(P_{kB},F_{iA},kB=1,2,...,12,iA=1,2,...,8) \\ D(L_{jA},L_{jB},iA=1,2,...,18,jB=1,2,...,18) \end{matrix} \right\rangle, \tag{A1}$$

where $\langle\ \rangle$ indicates the minimum value of the variables.

$D(P_{kA},F_{iB},kA=1,2,...,12,iB=1,2,...,8)$ are the distances between a vertex $(P_{kA},kA=1,2,...,12)$ of particle A and a face $(F_{iB},iB=1,2,...,8)$ of particle B, and can be determined by

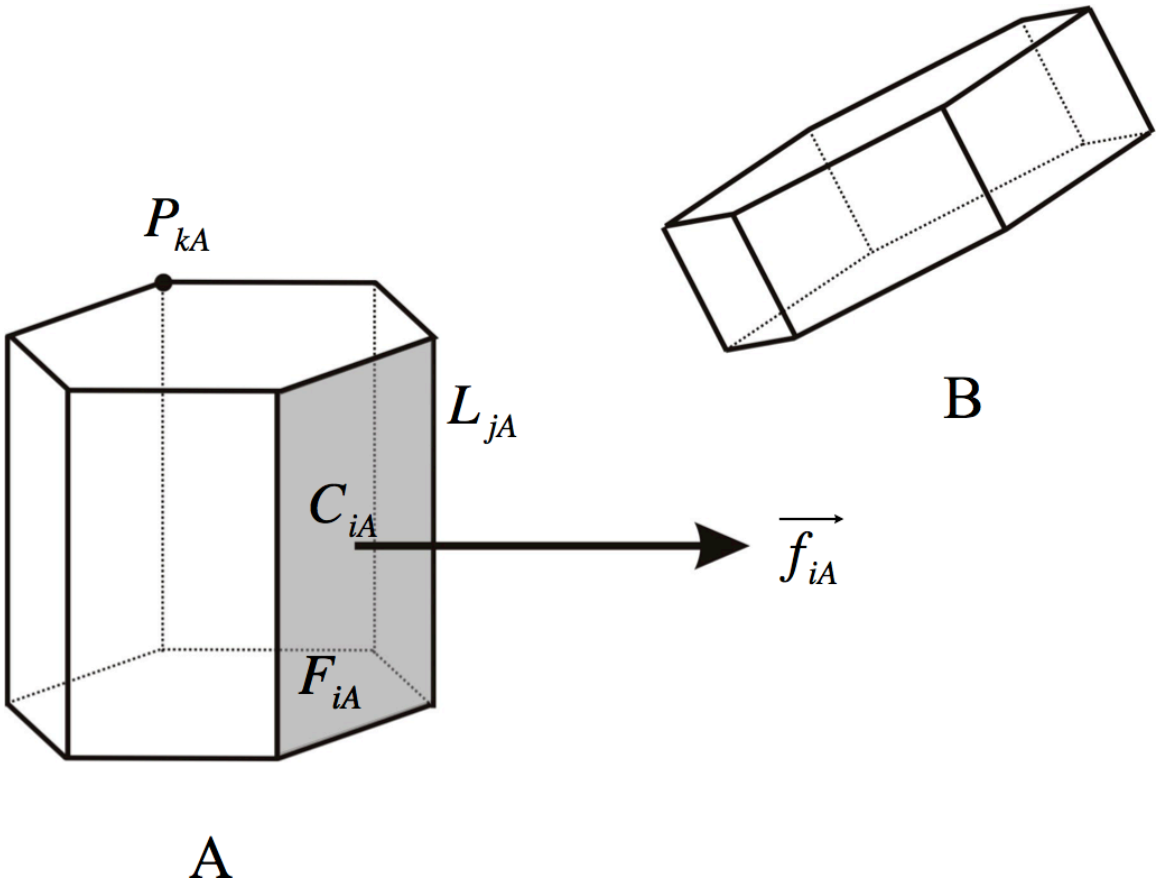

Fig. A1 Geometries of hexagonal particles.

$$D(P_{kA},F_{iB},kA=1,2,...,12,iB=1,2,...,8)=\begin{cases}\left|\overrightarrow{p_{kA}}-\overrightarrow{p_u}\right| \ (kA=1,2,...,12,iB=1,2,...,8) \\ for \quad P_u\in F_{iB} \\ \left\langle D(P_{kA},L_{iB\_m1},m1=1,2,...4(or\ \ 6))\right\rangle \\ (kA=1,2,...,12,iB=1,2,...,8) \\ for \quad P_u\notin F_{iB}\end{cases}, \tag{A2}$$

where L_{iB_m1} represents the edges on the face F_{iB}, and $\overrightarrow{p_u}$ is the position vector of P_u and can be given by

$$\overrightarrow{p_u}=\overrightarrow{p_{kA}}+\overrightarrow{f_{iB}}\frac{\overrightarrow{f_{iB}}\cdot(\overrightarrow{c_{iB}}-\overrightarrow{p_{kA}})}{\left|\overrightarrow{f_{iB}}\right|^2}. \tag{A3}$$

The distance between P_{kA} and L_{iB_m1} can be derived as follows:

$$D(P_{kA},L_{iB\_m1},m1=1,2,...4(or\ \ 6))=\begin{cases}\left|\overrightarrow{p_{kA}}-\overrightarrow{p_v}\right| \quad for \quad P_v\in L_{iB\_m1} \\ \left\langle\left|\overrightarrow{p_{kA}}-\overrightarrow{p_{iB\_m1\_m2}}\right| \ (m2=1 \ \ and \ \ 2)\right\rangle \ (m1=1,2,...4(or\ \ 6)) \\ for \quad P_v\notin L_{iB\_m1}\end{cases}, \tag{A4}$$

where $P_{iB\_m1\_m2}$ represents the vertices on L_{iB_m1}, and $\overrightarrow{p_v}$ is the position vector of P_v and can be given by

$$\begin{aligned}\overrightarrow{p_v}=&\frac{(\overrightarrow{p_{kA}}-\overrightarrow{p_{iB\_m1\_m2}})\cdot(\overrightarrow{p_{iB\_m1\_1}}-\overrightarrow{p_{iB\_m1\_2}})}{\left|\overrightarrow{p_{iB\_m1\_1}}-\overrightarrow{p_{iB\_m1\_2}}\right|^2}(\overrightarrow{p_{iB\_m1\_1}}-\overrightarrow{p_{iB\_m1\_2}}) \\ &+\overrightarrow{p_{iB\_m1\_1}} \ (m1=1,2,...4(or\ \ 6))\end{aligned}. \tag{A5}$$

$D(L_{jA},L_{jB},jA=1,2,...,18,jB=1,2,...,18)$ in Eq. (A1) is the distance between $L_{jA}(jA=1,2,...,18)$ and $L_{jB}(jB=1,2,...,18)$ from particle A and B, respectively, and can be given as follows:

$$D(L_{jA},L_{jB},jA=1,2,...,18,jB=1,2,...,18)=\left\langle\begin{array}{l}\left|\overrightarrow{p_{jA\_m3}}-\overrightarrow{p_{jB\_m4}}\right| \ (m3,m4=1 \ \ and \ \ 2)\\ D(P_{jA\_m3},L_{jB},m3=1 \ \ and \ \ 2)\\ D(P_{jB\_m4},L_{jA},m4=1 \ \ and \ \ 2)\\ D(P_w,L_{jA}) \ \ for \ \ P_w\in L_{jB}\end{array}\right\rangle, \quad (A6)$$

where $D(P_{jA\_m3},L_{jB},m3=1 \ \ and \ \ 2)$ and $D(P_{jB\_m4},L_{jA},m4=1 \ \ and \ \ 2)$ can be derived from Eq. (A4). The position vector of the P_w in Eq. (A6) is given by

$$\overrightarrow{P_w}=\overrightarrow{p'_{jA\_1}}+(\overrightarrow{p'_{jA\_1}}-\overrightarrow{p'_{jA\_2}})\left[\frac{(\overrightarrow{p'_{jA\_1}}-\overrightarrow{p_{jB\_1}})\times(\overrightarrow{p_{jB\_2}}-\overrightarrow{p_{jB\_1}})}{(\overrightarrow{p'_{jA\_2}}-\overrightarrow{p'_{jA\_1}})\times(\overrightarrow{p_{jB\_2}}-\overrightarrow{p_{jB\_1}})}\right]_z, \quad (A7)$$

where

$$\overrightarrow{p'_{jA\_1}}=\overrightarrow{p_{jA\_1}}+(\overrightarrow{l_{jA}}\times\overrightarrow{l_{jB}})\frac{(\overrightarrow{l_{jA}}\times\overrightarrow{l_{jB}})\cdot(\overrightarrow{p_{jB\_1}}-\overrightarrow{p_{jA\_1}})}{\left|\overrightarrow{l_{jA}}\times\overrightarrow{l_{jB}}\right|^2}, \quad (A8)$$

$$\overrightarrow{p'_{jA\_2}}=\overrightarrow{p_{jA\_2}}+(\overrightarrow{l_{jA}}\times\overrightarrow{l_{jB}})\frac{(\overrightarrow{l_{jA}}\times\overrightarrow{l_{jB}})\cdot(\overrightarrow{p_{jB\_1}}-\overrightarrow{p_{jA\_2}})}{\left|\overrightarrow{l_{jA}}\times\overrightarrow{l_{jB}}\right|^2}. \quad (A9)$$

The particles A and B are not overlapped in space if they satisfy,

$$\begin{cases}\sum_{iB=1}^{8}D(P_{kA},F_{iB},kA=1,2,...,12)\neq 3\sqrt{3}a_B+L_B\\ \sum_{iA=1}^{8}D(P_{kB},F_{iA},kB=1,2,...,12)\neq 3\sqrt{3}a_A+L_A \ ,\\ \sum_{jA=1}^{18}L_{jA}\bigcap\sum_{iB=1}^{8}F_{iB}=\varnothing\end{cases} \quad (A10)$$

where a_A and a_B and L_A and L_B are the semi-widths and lengths of the hexagonal particles, respectively. The derivation of $D(P_{kA},F_{iB},kA=1,2,...,12,iB=1,2,...,8)$ and $D(P_{kB},F_{iA},kB=1,2,...,12,iA=1,2,...,8)$ can be found in Eqs. (A1) and (A2). Figure A2 shows two types F_{iB}. If F_{iB} has a rectangular shape, the relationship between L_{jA} and F_{iB} in Eq (A10) can be derived as follows:

$$\begin{cases} L_{jA}\bigcap F_{iB}\neq\varnothing \quad for \quad \sum_{m5=1}^{4} D(L_{jA},L_{iB\_m5}) \neq a_B + L_B \\ L_{jA}\bigcap F_{iB}=\varnothing \quad for \quad \sum_{m5=1}^{4} D(L_{jA},L_{iB\_m5}) = a_B + L_B \end{cases}, \tag{A11}$$

where $D(L_{jA},L_{iB\_m5},m5=1,2,..,4)$ is the distance between L_{jA} and the boundaries of F_{iB}. The derivation of $D(L_{jA},L_{iB\_m5},m5=1,2,...4)$ can be found in Eq (A6). If F_{iB} has a hexagonal structure as shown in Fig. A2, $L_{jA}\bigcap F_{iB}$ can be given by

$$\begin{cases} L_{jA}\bigcap F_{iB}\neq\varnothing \quad for \quad \sum_{m6=1}^{6} D(L_{jA},L_{iB\_m6}) \neq 3\sqrt{3}a_B \\ L_{jA}\bigcap F_{iB}=\varnothing \quad for \quad \sum_{m6=1}^{6} D(L_{jA},L_{iB\_m5}) = 3\sqrt{3}a_B \end{cases}. \tag{A12}$$

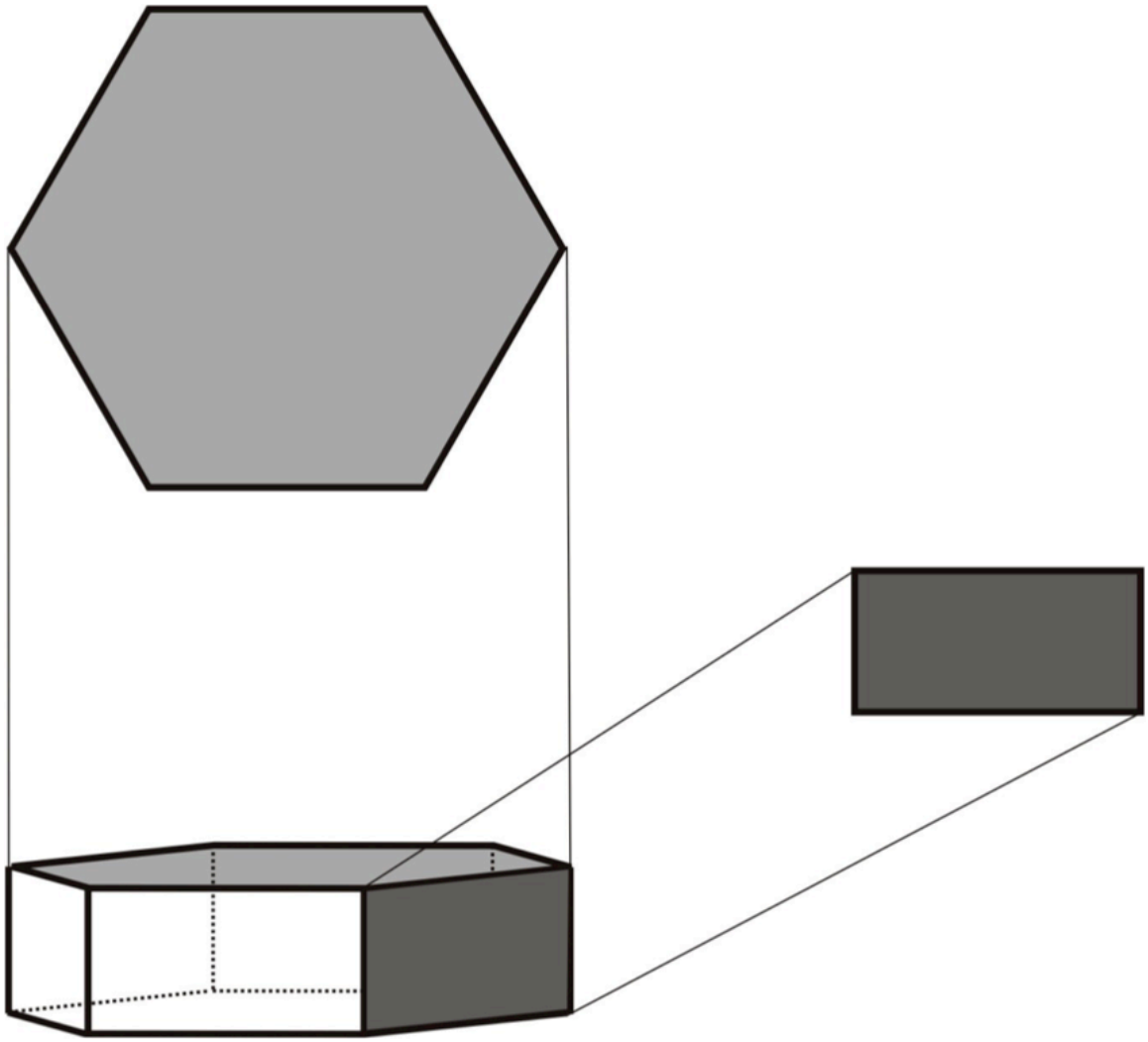

Fig. A2 Two types of faces for a hexagonal ice crystal.

APPENDIX B

COMPUTE PROJECTED AREA OF AN AGGREGATE

Figure B1 shows an aggregate A in the oxyz coordinate system. The projected area of an aggregate can be computed by an algorithm based on the Monte Carlo method. Consider a random disk D_i that is perpendicular to its center position vector $\overrightarrow{p_{i0}}$. The radius of D_i is equal to the maximum dimension of the aggregate D_m and a random point P_i on the disk can be derived from

$$\left|\overrightarrow{p_i} - \overrightarrow{p_{i0}}\right| = D_m\sqrt{\xi_A}\,, \tag{B1}$$

$$\overrightarrow{p_i}\cdot\overrightarrow{p_{i0}} = \left|\overrightarrow{p_{i0}}\right|^2, \tag{B2}$$

$$(\overrightarrow{p_i} - \overrightarrow{p_{i0}})\cdot(\overrightarrow{p_B} - \overrightarrow{p_{i0}}) = D_m\sqrt{\xi_A}\left|\overrightarrow{p_B} - \overrightarrow{p_{i0}}\right|\cos(2\pi\xi_B) \tag{B3}$$

where ξ_A and ξ_B are independent random numbers that are uniformly distributed on [0, 1], and $\overrightarrow{p_B}$ is the position vector of a fixed point on the face containing D_i, which can be given by

$$\overrightarrow{p_B} = (0,0,\frac{\left|\overrightarrow{p_{i0}}\right|^2}{(\overrightarrow{p_{i0}})_z})\quad . \tag{B4}$$

For a line L_i that satisfies

$$\begin{cases} P_i \in L_i \\ \vec{l}_i = \overrightarrow{p_{i0}} \end{cases}, \tag{B5}$$

we consider a M_i given by

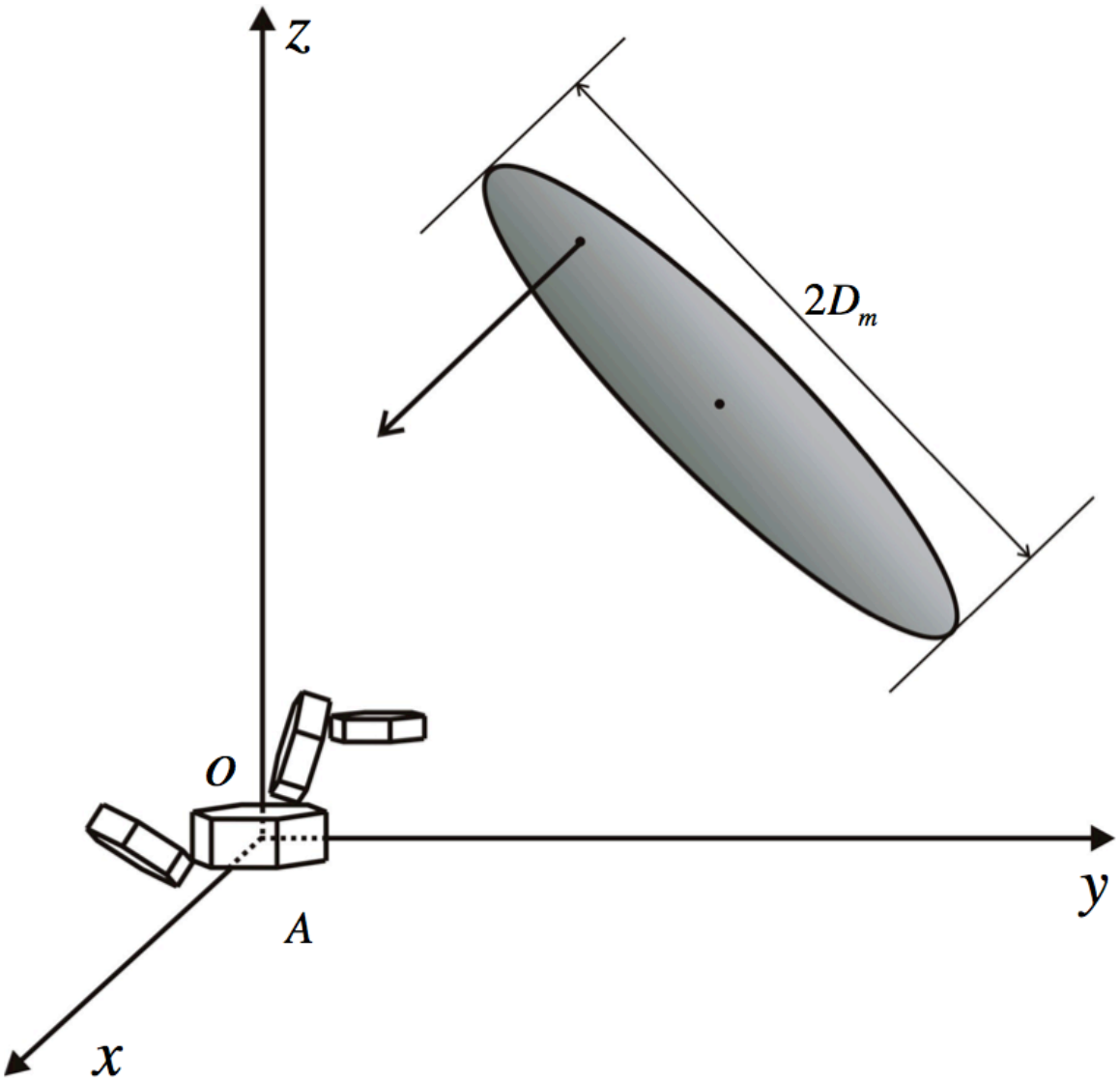

Fig. B1 A schematic illustrating the computation of the projected area of an aggregate ice crystal.

$$M_i = \begin{cases} 1 & for \quad L_i \bigcap \sum_{j=1}^{8N} F_j \neq \varnothing \\ 0 & for \quad L_i \bigcap \sum_{j=1}^{8N} F_j = \varnothing \end{cases}, \tag{B6}$$

where F_j indicates a face of aggregate A in Fig. B1, and N is the number of the hexagonal particles in A. The relationship between L_i and F_j can be derived using Eqs (A11) and (A12).

The projected area of aggregate A can be derived by

$$S = \pi D_m^2 \frac{\sum_{i=1}^{N} M_i}{N_L}, \tag{B7}$$

where N_L is the number of D_i in the computation. The algorithm to compute the projected area can be verified by replacing aggregate A with a hexagonal column whose projected area can be simply determined by

$$S = \frac{3}{4} a(\sqrt{3}a + 2L), \tag{B8}$$

where a and L represent the semi-width and length of the hexagonal column, respectively. This result is obtained by using the fact that the projected area of a convex body at random orientation is simply one-fourth of its surface area. Our results indicate that the projected area of an aggregate can be accurately computed for the case N_L>100,000.

VITA

Yu Xie received his Bachelor of Science degree in physics from Peking University, Beijing, China in July 2003. He received his Master of Science degree in atmospheric sciences from Texas A&M University in May 2007. He continued his study in Department of Atmospheric Sciences at Texas A&M University beginning in May 2007, and received a Ph.D. degree in December 2010.

Mr. Xie may be reached at the Department of Atmospheric Sciences, Texas A&M University, 3150 TAMU, College Station, TX 77843-3150. His email address is xieyupku@tamu.edu.

Peer-Reviewed Publications

Ding, S., **Y. Xie**, P. Yang, F. Weng, Q. Liu, B. Baum, and Y. X. Hu, 2009: Estimates of radiation over clouds and dust aerosols: optimized number of terms in phase function expansion, *J. Quant. Spectro. Rad. Transfer*, 110, 1190-1198.

Xie, Y., P. Yang, G. W. Kattawar, P. Minnis, and Y. X. Hu, Effect of the inhomogeneity of ice crystals on retrieving ice cloud optical thickness and effective particle size, *J. Geophys. Res*. 114, doi: 10.1029/2008JD011216.

Jin, Z., T. P. Charlock, P. Yang, **Y. Xie**, and W. Miller, 2008: Snow Optical Properties for Different Particle Shapes With Application to Snow Grain Size Retrieval and MODIS/CERES Radiance Comparison Over Antarctic, *Remote Sensing of Environment*, 112, 3563-3581.

Lawless, R., **Y. Xie**, P. Yang, G. W. Kattawar, and I. Laszlo, 2006: Polarization and effective Mueller matrix for multiple scattering of light by nonspherical ice crystals, *Optical Express*, Vol. 14, 6381-6393.

Xie, Y., P. Yang, B.-C. Gao, G. W. Kattawar, and M. I. Mishchenko, 2006: Effect of ice crystal shape and effective size on snow bidirectional reflectance, *J. Quant. Spectro. Rad. Transfer*, 100, 457-469.